COMPUTATIONAL STUDIES ON THE MECHANICAL INHOMOGENEITY OF TROPOMYOSIN, AND THE DIRECTED AND COOPERATIVE MOTILITY OF THE NCD MOTOR

A Dissertation

by

SIRISH KAUSHIK LAKKARAJU

Submitted to the Office of Graduate Studies of
Texas A&M University
in partial fulfillment of the requirements for the degree of

DOCTOR OF PHILOSOPHY

December 2011

Major Subject: Biomedical Engineering

COMPUTATIONAL STUDIES ON THE MECHANICAL INHOMOGENEITY OF TROPOMYOSIN, AND THE DIRECTED AND COOPERATIVE MOTILITY OF THE NCD MOTOR

A Dissertation

by

SIRISH KAUSHIK LAKKARAJU

Submitted to the Office of Graduate Studies of
Texas A&M University
in partial fulfillment of the requirements for the degree of

DOCTOR OF PHILOSOPHY

Approved by:

Chair of Committee,	Wonmuk Hwang
Committee Members,	Mariappan Muthuchamy
	Roland R. Kaunas
	Brian E. Applegate
Head of Department,	Gerard L. Cote

December 2011

Major Subject: Biomedical Engineering

ABSTRACT

Computational Studies on the Mechanical Inhomogeneity of Tropomyosin, and the Directed and Cooperative Motility of the Ncd Motor. (December 2011)

Sirish Kaushik Lakkaraju, B.En., University of Madras, India;

M.S., Texas A&M University

Chair of Advisory Committee: Dr.Wonmuk Hwang

Alpha-helical coiled-coils are common protein structural motifs with varied mechanical roles, such as, tropomyosin in muscle contraction or neck-stalks of kinesins and myosins, in motor proteins. Using computer simulations, we characterized elastic properties of coiled-coils both, globally and locally. Normal mode analysis for global elastic properties revealed a buckling instability due to inherently present weak non-bonded forces. We characterized this using a critical buckling length (l_c). For coiled-coils, l_c was significantly less than their persistence length thereby governing the filament conformation. We also found that mutations to the hydrophobic residues at the knob-into-hole interface affect elasticity of coiled-coils significantly. We built a flexibility map of tropomyosin using a local fluctuation analysis and found regional variations in flexibilities due to such breaks in the knob-into-hole packing. Overall, flexibility varies by more than twofold and increases towards the C-terminal region of the molecule. Actin binding sites in α zones and broken core regions due to acidic residues at the hydrophobic face such as, the Asp137 and the Glu218, are found to be the most labile with moduli for splay and broad face bending as 70 nm and 116 nm, respectively. Such variations in flexibility could be relevant to the tropomyosin function, especially for moving across the non-uniform surface of F-actin to regulate myosin binding.

Non-claret disjunction (Ncd), is a Kinesin-14 family protein that walks to the

microtubule's minus end. Although available structures show its α-helical coiled-coil neck in either pre- or post-stroke orientations, little is known about the transition between these two states. Using a combination of molecular dynamics simulations and structural analyses, we find that the neck travel is a guided diffusion involving sequential intermediate contacts with the motor head. The post-stroke is at a higher free-energy minimum than the pre-stroke. The importance of intermediate contacts correlates with the existing motility data including those of mutant Ncds and other members of the kinesin-14 family. While the forward motion has a $\sim$4.5 k_BT (k_B: Boltzmann constant, T = 300 K) free energy barrier, recovery stroke goes nearly downhill in free energy. The hysteresis in forward and reverse neck motion energetics arises from the mechanical compliance of the protein, and together with guided diffusion, it may be key for the directed motility of Ncd.

Although it is known that neighboring Ncds on a microtubule (MT) have an attractive interaction and a group of Ncds act cooperatively, the physical basis of neither this attraction nor the cooperativity is known. From structural analysis of Ncd neighbors on an MT lattice we find that steric hindrances between the coiled-coil neck-stalks of longitudinal neighbors drive synchrony among a group of Ncds on a single protofilament. Across lateral dimers, surface loop L2 of the motor-head (MH) that is not bound to the MT (unbound-MH) in a pre-stroke dimer, is seen to have strong attraction to the nucleotide pocket in the MH that is bound to MT (bound-MH) of its off-axis neighbor. Such an attraction will however impede the motility in both the dimers. We hence propose rules that drive motor binding to an MT site in the presence of immediate neighbors such that motility of the group is not compromised. The unbound-MH, whose role in the walking step of an Ncd was unclear, is thus seen to regulate MT decoration.

To Bhagwan Sri Sathya Saibaba

ACKNOWLEDGMENTS

Its a pleasure to thank many people who made this dissertation possible. Anything I say about how much they mean to me and my work will, however, be an understatement.

I have utmost gratitude for Dr.Wonmuk Hwang for his continuous guidance, patience, and support throughout the course of this research. Throughout the last six years in his lab, I have learned and appreciated a great many things about him both as a professor and a person. His hard-work and patience are some virtues I will always look up to. I also particularly enjoyed the freedom of going to him at any time with any questions, results or discussions. I have also enjoyed his classes and apart from developing an interest in statistical mechanics and microscale biology, I have also learned some great teaching techniques from him. I am also thankful for the numerous opportunities he gave me for presenting my results across different conferences. I believe all my training under him has shaped me into being a better researcher and a person.

I thank Dr.Mariappan Muthuchamy for introducing me to tropomyosin and directing me to literature in the area. I also thank Dr.Roland Kaunas and Dr.Brian Applegate for serving on my committee and providing valuable suggestions. I thank Dr.Humphrey for his extremely enjoyable classes. His clarity of thought and elucidation of a concept or an idea always amazed me.

I thank my lab members from various times: Krishna, Jiyong, John, Francesca, Jinseon, Weewen, Xiaojing, Andrew, Esma, Amol and Tyler. Krishna has been a constant companion throughout my time here, and I thank him for the many stimulating discussions in both research and non-academic topics. It was always a new dimension of thought with him. I thank Jiyong for his expertise and constant guidance during

many critical times. I thank John and Weewen for teaching me motility experiments.

Life at Texas A&M University was particularly enjoyable, thanks to the company of many friends. I thank Soma for all the lively discussions on myriad topics. I will always cherish the short-film making experience with him and other friends through the Spring 07. These times and experiences have been so enriching and I believe they have molded my thinking through the years.

I cannot thank my family enough for everything they have done. My wife Vichika was a tremendous support system throughout grad school. Both through good and frustrating times, she has always been around with a comforting smile. Also, my parents for instilling the right values and the importance of education early on. My father's strict adherence to his set of principles and my mother's resilience through all times will always be something I look up to. I thank my parents-in-law: my father-in-law for his advice on how to navigate through the academic world and my mother-in-law for her passion for teaching. Thank you, Sarath and Deepthi for the nice pen. Finally, I thank my aunts and uncles for driving me back to grad school.

TABLE OF CONTENTS

CHAPTER Page

CHAPTER Page

LIST OF TABLES

TABLE Page

LIST OF FIGURES

FIGURE Page

FIGURE Page

FIGURE Page

FIGURE Page

FIGURE Page

FIGURE Page

FIGURE Page

CHAPTER I

INTRODUCTION:PREVIOUS STUDIES ON TROPOMYOSIN AND KINESIN-14 NCD AND MOTIVATION

A. Tropomyosin

Tropomyosin makes up a large complex family of α-helical coiled coils found in eukaryotes, and is usually seen bound to F-actin [1]. In thin filaments of muscle, it regulates actin-myosin interactions by winding around actin in a right handed fashion and blocking the actin-binding sites of myosin. While precise roles of non-muscle tropomyosin isoforms such as those found in stress fiber assemblies is poorly understood [2], tropomyosin has been observed to increase actin's persistence length by about 1.5 times [3]. It could thus significantly affect mechanical properties of the cytoskeleton.

Since its 284 pairs of residues ($\sim$40 nm) follow mostly an unbroken heptad (seven-residue) periodicity, tropomyosin has been considered as a paradigm of an α-helical coiled-coil [4]. In addition, in muscle isoforms, there is a $\sim$40-residue periodicity where each period is divided into two alternative actin binding α and β zones. A single tropomyosin molecule can attach to 7 consecutive actin monomers through a strip of negatively charged side chains in either α or β zones. While α zones are more regularly negatively charged [5], the actual actin binding residues on the surface of tropomyosin are still not clearly known. Currently accepted "consensus" residues [6] are those initially identified by Phillips [5, 7]. Point mutations along the charged surface residues of tropomyosin have been associated with changes in cardiac muscle contractility [8] and dilated cardiomyopathy [9]. Regulation of myosin binding

---

´The journal model is *IEEE Transactions on Automatic Control.*

is achieved by the Ca^{2+} dependent action of tropomyosin and troponin [4]. In the 'off' state, tropomyosin is bound along the outer edge of the F-actin, blocking the myosin binding site. When Ca^{2+} binds to troponin (bound to both tropomyosin and F-actin), it undergoes conformational changes, allowing tropomyosin to move into the groove of F-actin, exposing myosin binding site. Earlier this process was described by a two-state model [5]. More recent observations led to a three-state steric blocking model that consists of the off, blocked, and potentiated states depending on whether tropomyosin covers F-actin's myosin binding site fully, partially, or exposes it [7]. Although details of this process are still unknown, it is likely that tropomyosin undergoes deformation along the non-uniform helical surface of F-actin. Along the molecule there are clusters of alanines which are thought to induce a bend, thereby assisting the coiled-coil to wind around F-actin [10]. However, the energetics of deformation as the molecule binds and moves on F-actin has not been characterized in detail. The mechanical properties of tropomyosin should hence be an important factor for its function.

Previous mechanical characterization of tropomyosin treated it as a homogeneous filament and estimated its global persistence length (l_p) to be about 150 nm [11]. However, our previous estimate of bending stiffness of α-helical coiled-coils using normal mode analysis was about 500 nm [12]. Hence it is important to determine the factors that modulate stiffness of coiled-coils. Functionally distinct domains for actin-binding or for inducing bend in tropomyosin are likely to have varied mechanical properties. Thus a local flexibility map will be relevant in understanding how these functionally distinct domains modulate elasticity of tropomyosin.

B. Kinesin-14 Ncd

Ncd (Non-claret disjunction) is a homodimer that belongs to the kinesin-14 family of motor proteins and is involved in spindle assembly and stabilization during meiotic chromosome distribution in the Drosophila embryo [13]. Cytological analysis reveals diffusive, multipolar or abnormally wide spindles in the meiosis I oocytes of the ncd mutants that cause chromosomes to become widely scattered during the two meiotic divisions and result in the formation of multiple telophase II nuclei of varying numbers and sizes [14].

1. Motility mechanism

With a 40% sequence similarity and less than 2 Å root mean square deviation (RMSD) in the backbone atoms of the central β sandwich (eight β-sheets flanked by 3 α helices on either side, Fig. 1), the motor-heads (MH) of Ncd and conventional kinesins (Kinesin-1 (Kin1)) are structurally very similar. Despite the high structural similarity in the motor heads with which these dimers bind to and walk on microtubule (MT), the motility properties of Ncds and Kin1 are largely different. While Kin1 travel to the plus end of the MT and walk processively, the kinesin-14 family (Ncd, Kar3, etc) motors walk to the minus ends of the MT non-processively [15].

It is believed that different motility behaviors across motors are achieved by modifying subdomains such as those mediating track binding, force generation, and allosteric transduction of ATPase or mechanical events to other parts of the motor [16]. Between Kin1 and Ncd, a key structural difference is the neck-linker that connects the MH to the coiled-coil stalk [17]. Instead of a flexible *neck linker* as in Kinesin-1, Ncd has an α-helical *neck* that continues from the stalk and connects directly to the MH (Fig. 1). Mutational studies showed that directionality is partly determined

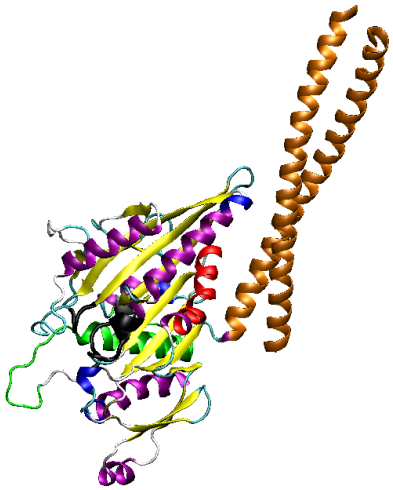

Fig. 1. With 8 β-sheets (yellow) surrounded by 3 α-helices (purple) on either side, motor head of Ncd is similar to kinesin. Black: Nucleotide binding pocket, green: MT binding regions, red: α-1 subdomain that interacts with the coiled-coil stalk (orange).

by the neck domains: A chimeric Kinesin-1 with Ncd's neck showed MT minus-end directed motility whereas an Ncd with Kinesin-1's neck linker was plus-end directed, although motility in both cases was impaired [17, 18, 19, 20]. However, the underlying structural mechanism is still not well-understood, in particular for Ncd.

In the case of Kinesin-1, the neck linker is disordered when unbound, and it docks to the MH upon ATP binding [21]. Recent computational [22] and experimental [23] studies showed that the N-terminal *cover strand* protruding from the MH is also crucial for force generation, where the folding of the cover strand and the neck linker into a β-sheet named the cover-neck bundle provides the necessary forward bias. In contrast to such an order-disorder transition, cryo-electron microscopy (cryo-EM) and x-ray studies indicate that the α-helical neck of Ncd rotates by about 70°, more like a lever-arm [24, 25]. In x-ray structures of Ncd in the pre- and post-stroke states, the neck orients and makes contacts with the MH respectively in the the plus- and

minus-end directions. However, the atomistic details of the transition between the two states are unknown. The MH-neck contacts have different roles in Ncd motility, as can be seen by the MT gliding velocities of the corresponding point mutations: Some maintain a near wild-type (WT) activity [26] while others even switch direction [27]. The issue of the nucleotide state in which the motion of the neck occurs is also not clear [25, 28, 29]. Single-molecule studies even suggest occasional plus-end directed stepping events [15, 30].

Atomistic simulations of the Ncd between these two known two end states will hence not only explain the physical basis of the neck rotation, but also the roles of different MH-neck contacts on the Ncd motility. Ncd and other members of the kinesin-14 family have a large sequence and structure similarity with critical differences only in the MH-neck contact sites. Hence, determining the role of the MH-neck contacts in the motility cycle of Ncd will also explain motility of these others motors from the kinesin-14 family. Further, atomistic trajectories of the neck transition maybe used for calculating the energetics and features of the minimum free energy path involved in the walking step of Ncd.

2. Cooperativity

Ncds are known to act cooperatively, as the forces measured on an MT acted upon by a group of Ncds were much greater than that generated by a single Ncd [31]. When a group of Ncds are sandwiched between two MTs, depending on whether the MTs have a parallel or anti-parallel orientation, the Ncds act either as cross-linkers or trigger sliding between the two filaments respectively [31]. With the Ncds attaching to the two filaments through both their MT binding domains, the neck-stalk rotation to the minus-end during the walking step of individual Ncds, leads to these two different phenomena that is modulated by the orientation of the two filaments. This difference

in behavior is crucial for proper mitosis activity as Ncds are found localized at two different sites: those at the poles (where the MTs are oriented parallely) act as cross-linkers, while those between the centrosome and kinetochore MTs (opposing polarity) are involved in sliding [32].

Theoretical models predicted the force generated by a group of Ncds and the effect of this cumulative force on the filament [33, 34]. These models however, failed to incorporate the effect of interactions between immediate neighbors on the group dynamics. Recent studies show an attractive interaction of about 1.5-1.7 k_BT between immediate neighbors among kinesin-1 and Ncd populations [35, 36]. This attractive interaction seemed to aid the complete decoration of the MT, which is important for EM reconstruction studies [35, 37] of these motors. The physical origin of this attraction, on the other hand remained unknown. Also unknown is the effect of this attraction on the walking step energetics and the motility cycle of the motors.

Since the end-states of the Ncd are known, structural analysis and molecular dynamics simulations with various combinations of pre-& post-stroke Ncd dimers occupying two neighboring sites on an MT lattice can reveal the physical basis of attraction between two motors. Also, this atomistic analysis could reveal the possible role of various structural elements such as the coiled-coil neck-stalks and the unbound-MH in controlling interactions between neighbors and thereby regulating synchrony between a group of motors.

CHAPTER II

MODULATION OF ELASTICITY IN FUNCTIONALLY DISTINCT DOMAINS OF TROPOMYOSIN COILED-COIL*

A. Introduction

Tropomyosin is a 284 pair residue α-helical coiled-coil that winds around F-actin and regulates actin-myosin interactions in muscle. It is also known to increase the stiffness of actin-filaments by nearly 1.5 times. Previous mechanical characterization of tropomyosin treated it as a homogeneous filament and estimated its global persistence length (l_p) to be about 150 nm [11]. Yet, due to the presence of functionally distinct regions such as for actin binding or for inducing a bend, it is likely that mechanical properties of tropomyosin is non-uniform along the molecule. Here we construct a flexibility map of a cardiac muscle tropomyosin (Protein Data Bank (PDB) ID: 1C1G) [38] using molecular dynamics (MD) simulations. Local coordinate basis named triads were assigned along the length of the molecule and changes in their relative orientation during MD was monitored, from which we calculated local bending and torsional stiffness. For comparison, we also use the standard leucine zipper coiled-coil and study the effect of side chain mutations on its bending stiffness.

While bending stiffness of a single α-helix is not very sensitive to its amino acid sequence [12, 39], we find that coiled-coil has a stronger sequence dependence, contrary to a previous continuum-based theoretical estimate [40] which did not consider

*Portions of this chapter are reprinted with permission from Sirish Kaushik Lakkaraju and Wonmuk Hwang, "Modulation of elasticity in functionally distinct domains of tropomyosin coiled-coil", Cell.Mol.Bioeng.,Vol. 2, No.1 ,pp 57–65,2009,Copyright 2009 by Springer Science and from Sirish Kaushik Lakkaraju and Wonmuk Hwang, "Critical buckling length vs. persistence length: what governs a biofilament conformation?", Phys. Rev. Lett., Vol 102, pp 118102,2009, Copyright 2009 by APS.

energetic contribution by the steric knob-into-hole packing of hydrophobic side chains between two α-helices [41] . Thus coiled-coils with variations in amino acid sequence may not be treated as uniform elastic rods. For tropomyosin, we find that its bending moduli vary by more than twofold, between 220 and 470 nm. Around the broken core region Asn137 [42], it further drops to 116 nm. Hence, analogous to the strength of a chain determined by its weakest link, the 'global' persistence length obtained by considering the entire tropomyosin molecule would be smaller.

The local flexibility map also elucidates how variation in flexibility is tailored for the function of tropomyosin. In particular, α zones are more flexible than β zones, which would be advantageous since tropomyosin binds to the deeper actin groove in the blocked and more in the potentiated states through α zones. Being more flexible, α zones may easily reach their binding site in the actin groove without requiring a rigid-body motion of the entire molecule along F-actin. More generally, local flexibility map of fibrous proteins will provide useful insights into their mechanical function.

B. Theory

1. Local fluctuation analysis

We first derive the expression for the elastic energy of a continuum rod [43, 44] and explain how it is applied to the coiled-coil geometry. Our method is basically the same as the one used by Choe and Sun for analyzing α-helix elasticity, except that they averaged fluctuation over the length of the molecule [39].

Let $\mathbf{r}(s)$ be the position vector of the contour of a rod of length L parametrized by the contour length s, such that $\mathbf{r}(0)$ and $\mathbf{r}(L)$ represent two ends of the rod. The

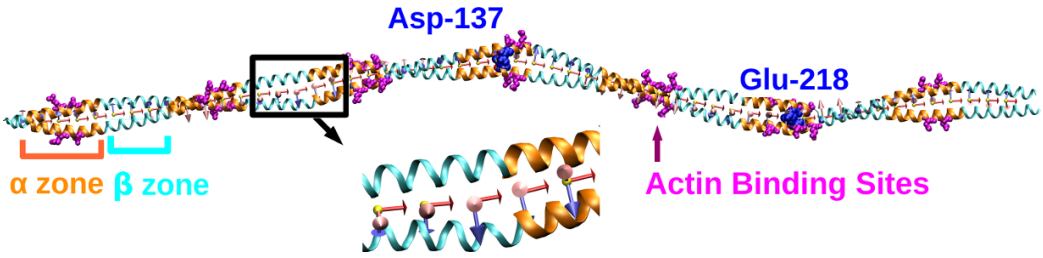

Fig. 2. Crystal structure of a cardiac muscle tropomyosin (PDB ID: 1C1G). The α and β zones are shown in orange and cyan, respectively. Successive α or β zones rotate by about 90° axially. Side chains of the putative actin binding residues in α zones are shown in magenta. Asp137 and Glu218 are shown in blue van der Waals representation. Starting with triad 1 on the left (N-terminus), we assigned 56 triads along the length of the molecule in intervals of 5 residues. Triads 1 and 56 were not considered for the flexibility map to eliminate edge effects. The magnified image shows triads 14-18. $\vec{e}_3$ (red) points to the right, $\vec{e}_2$ (blue) points downward, and $\vec{e}_1$ (pink) points out of the page.

unit tangent vector $\mathbf{e}_3(s)$ at a point s is then

$$\mathbf{e}_3 = \frac{d\mathbf{r}}{ds}. \tag{2.1}$$

We introduce two additional unit vectors $\mathbf{e}_1(s)$ and $\mathbf{e}_2(s)$ that are binormal to $\mathbf{e}_3$, so that $\{\mathbf{e}_1, \mathbf{e}_2, \mathbf{e}_3\}$ forms a right-handed *triad*. Choices for $\mathbf{e}_1$ and $\mathbf{e}_2$ are not unique and they only need to be continuously differentiable with respect to s. Typically $\mathbf{e}_1$ and $\mathbf{e}_2$ are chosen based on the cross-sectional geometry of the rod, to better represent the physics.

Now we consider a rod whose equilibrium shape is straight. When it deforms, the curvature vector $\vec{\omega}$ is related to $\mathbf{e}_3$ by [43]

$$\frac{d\mathbf{e}_3}{ds} = \vec{\omega} \times \mathbf{e}_3, \tag{2.2}$$

i.e., $\vec{\omega}$ is the rate of rotation of the triad along s. When decomposed using triads, ω_1

and ω_2 represent bending of the rod in two directions normal to the contour and ω_3 represents torsion (we ignore stretch in the axial direction, which is usually a good approximation for α-helices and β-sheet filaments since their backbone hydrogen bond network is stiff due to the narrowly distributed hydrogen bond distances [12, 45]). If $\vec{e}_1$ and $\vec{e}_2$ are chosen as principal axes of the cross section of the rod, for a linear elastic material (but not necessarily homogeneous along the length), the elastic energy per unit length at s is given by

$$E(s) = \frac{1}{2}\sum_{i=1}^{3} \kappa_i \omega_i^2. \tag{2.3}$$

Here, $\kappa_i(s)$ is the stiffness of the rod with respect to the rotation along $\mathbf{e}_i$. The total elastic energy of the rod is then $E_{tot} = \int_0^L dsE(s)$. For a rod whose equilibrium shape is not straight, Eq. 2.3 can be generalized to

$$E(s) = \frac{1}{2}\sum_{i=1}^{3} \kappa_i (\omega_i - \omega_{0i})^2, \tag{2.4}$$

where $\omega_{0i}(s)$ is the equilibrium curvature of the rod.

If the rod is in thermal equilibrium at temperature T, the average elastic energy stored in the i-th direction for the segment $(s, s + \Delta s)$ satisfies the equipartition theorem [46]

$$\langle E_i(s)\rangle \Delta s = \frac{k_B T}{2} = \frac{1}{2}\kappa_i \langle(\omega_i - \omega_{0i})^2\rangle \Delta s. \tag{2.5}$$

Here $\langle\cdot\rangle$ denotes ensemble or time average and Δs is chosen small enough so that κ_i, ω_i, and ω_{0i} can be considered invariant over this interval. k_B is Boltzmann constant.

For tropomyosin, we assigned triads as follows. First, centroids for each α-helix were assigned with an interval of 5 residues. These were chosen using the position of ten C_α atoms in an overlapping manner, so that the first centroid is based on residues 1–10, the second on 6–15, *etc.* In total there are 56 centroids on each α-helix. The midpoint between n-th centroids of the two helices then defines the contour vector

$\mathbf{r}_n$ ($n = 1 \cdots 56$). We assigned $\mathbf{e}_3 = (\mathbf{r}_{n+1} - \mathbf{r}_n)/|\mathbf{r}_{n+1} - \mathbf{r}_n|$ and $\mathbf{e}_1$ was obtained as a unit vector normal to both $\mathbf{e}_3$ and the vector pointing from centroid n of helix A to that of helix B (choice of helix A and B is arbitrary). This fixes $\mathbf{e}_2 = \mathbf{e}_3 \times \mathbf{e}_1$ (Fig. 2). To construct triad 56 (the last one), a new centroid, 57 was calculated using residues 281–284. But triads 1 and 56 were not used for the actual calculation to eliminate possible end effects. The distance Δs between triads is not uniform across the molecule (*cf.*, part (a) of the figure shown on page 21). We used the value of Δs for each successive triad pair averaged over the simulation time.

The curvature vector $\vec{\omega}_n$ was calculated as follows. Two neighboring triads $\{\mathbf{e}_{ni}\}$ and $\{\mathbf{e}_{(n+1)i}\}$ ($i = 1, 2, 3$) can be related by a transformation matrix $\mathbf{U}$ employing Euler angles

$$\vec{e}_{(n+1)i} = \sum_j U_{ij} \vec{e}_{nj}. \tag{2.6}$$

Expressing each unit vector of a triad in terms of three Cartesian components, Eq. 2.6 can be cast in a matrix form, $\mathbf{E}_{(n+1)} = \mathbf{U}\mathbf{E}_n$. The i-th row of the 3×3 matrix $\mathbf{E}_n$ represents the three cartesian components of $\vec{e}_{ni}$. Multiplying $\mathbf{E}^{-1}$ on both sides yields $\mathbf{U}$ and hence the three Euler angles θ_i (the standard notation for Euler angles are α, β, and γ, but we use θ_i for notational simplicity).[47] Components of the curvature vector are then $\omega_{ni} = \theta_i/\Delta s$. In equilibrium, its distribution is Gaussian. By measuring average and variance, Eq. 2.5 can be used to get κ_i for each triad. Below we present data using the persistence length $l_{pi} = \kappa_i/k_B T$ ($T = 300K$) instead of κ_i. As Fig. 2 shows, l_{p1} is the persistence length with respect to the splay deformation of the molecule as a twisted tape whereas l_{p2} is for bending of the broad face. Torsional rigidity is represented by l_{p3}.

Note that we implicitly assumed that $\mathbf{e}_1$ and $\mathbf{e}_2$ as assigned above are local principal axes. If they are not, there is a term proportional to the product $\omega_1\omega_2$

in Eq. 2.3. Although it is possible to find principal axes based on the distribution of ω_1 and ω_2, we did not do that since our analysis based on $\mathbf{e}_1$ and $\mathbf{e}_2$ provides an intuitively clear picture of tropomyosin as a twisted tape, while a more accurate set of principal axes may depend on local amino acid sequence, resulting in a less intuitive geometry. Furthermore, as explained below, our simple approach still provides many useful information about the elasticity of tropomyosin.

2. Normal mode analysis

Determining flexural rigidity $\kappa_b = \min(\kappa_1, \kappa_2)$ and $l_p = \kappa_b / k_B T$ using normal mode analysis (NMA) is well documented in earlier works. [12, 45, 48] Here we just present the equations used.

For a freely vibrating rod in a linear elastic regime, flexural rigidity can be retrieved from the following relation

$$\kappa_b = \frac{\rho_l (\omega^{(m)})^2}{(k^{(m)})^4}. \tag{2.7}$$

Here, ρ_l is the mass per unit length, $\omega^{(m)}$ is the angular frequency of the m-th bending mode (note that this is different from the component of the curvature vector of the n-th triad ω_{ni} introduced above). $k^{(m)}$ is the wave number given by $\frac{c^{(m)}}{L}$, with $c^{(1)} = 4.7300$, $c^{(2)} = 7.8532$, $c^{(3)} = 10.9956$, *etc.* L is the length of the rod. [45] In principle, κ_b does not depend on the mode number m. [12] In calculations below, we use the first bending mode ($m = 1$).

C. Simulation details

We used CHARMM [49] version c34b1 for simulations and Visual Molecular Dynamics (VMD) [50] for visualizations. The param19 force field in CHARMM was used. [51]

For NMA of leucine zipper structures, straight coiled-coils were constructed using a C-code provided by Offer. [52] They were energy minimized in a two-step process. First, backbone atoms were constrained harmonically with a spring constant of 5 kcal/(mol·Å^2) and side-chains were energy minimized using the adopted basis Newton-Raphson (ABNR) method until the energy change between successive minimization steps reached less than the default tolerance of CHARMM. Next, constraints were removed and the entire molecule was again fully energy minimized. The VIBRA facility of CHARMM was used to calculate normal modes and their frequencies. Stiffness was calculated using Eq. 2.7.

For the flexibility map, simulations were carried out on the 1C1G structure. Since a coiled-coil has a well-defined packing geometry by the knob-into-hole interhelical packing and the backbone hydrogen bonds in the α-helices, conformational fluctuations are likely to exist in the solvent exposed side-chains. In MD simulations, these are likely to fluctuate. Hence, although the resolution of 7-Å for a crystal structure is low, it is still likely to yield global conformational changes that are relevant for our study.

To incorporate the effect of solvation effects, we used the ACE2 continuum solvent model in CHARMM.[53, 54] It has been previously shown that water molecules do not affect the elasticity of α-helices much, although stability may be affected more.[12, 39] This is because the elasticity is determined mainly by the network of backbone hydrogen bonds rather than by interaction among side chains and water molecules. It is expected that the same is true for coiled-coils, which, in addition to backbone hydrogen bonds, have the knob-into-hole packing of hydrophobic residues as a major determinant of elasticity.

After energy minimization as described above, MD simulation was performed with a step size of 1 fs. The system was heated for 650 ps from 0 K to 300 K, in 5

K increment every 10 ps. After heating, equilibration run followed for 200 ps, during which velocities were rescaled if the temperature deviated from 300 K by more than 5 K. The final production run lasted 10 ns. Coordinates were recorded every 10 ps, totaling 1000 coordinate frames, with 56 triads per frame. To calculate stiffness, we made histograms of ω_{ni} ($n = 1 \cdots 56$, $i = 1, 2, 3$), with a bin size of 0.002 rad/Å (parts (a,b) of the figure in page 19). Fitting logarithm of this histogram with a quadratic curve (parts (c,d) of the figure in page 19) yields average and variance of ω_{ni}. We calculated stiffness by using Eq. 2.5.

D. Results

1. Critical buckling length governs coiled-coil filament conformation

When we calculated flexural rigidity for coiled-coils with leucine-zipper sequence of varying lengths using Eqn. 2.7, we noted that the bending stiffness dropped for longer coiled-coils. The drop of κ_b for longer coiled-coils is due to weak non-bonded attractions among atoms that increase as the chain bends and eventually lead to buckling instability.

To check, we constructed a bead on a chain model (*1D chain*) where beads have the mass of a carbon atom, and are connected by harmonic springs of rest length $b = 1$ Å and spring constant $K_b = 8000$ kcal/mol·Å^2. Bending stiffness is prescribed by a harmonic potential for the bond angle θ, $U(\theta) = K_\theta(\theta - \pi)^2$, with $K_\theta = 800$ kcal/mol·rad^2. Non-bonded attraction is incorporated via the Lennard-Jones potential for the distance r between any two non-neighbor beads.

$$V_{LJ}(r) = \epsilon \left[(2b/r)^{12} - 2\,(2b/r)^{6} \right]. \tag{2.8}$$

NMA shows that when $\epsilon = 0$, κ_b does not drop for any length of the chain. κ

however dropped for $\epsilon = 0.3$ kcal/mol and further for $\epsilon = 0.7$ kcal/mol, confirming that the drop is indeed due to the attractive force.

These results suggest that non-bonded attraction cannot be ignored for sufficiently long filaments. Even when forces balance in a straight configuration, attraction between two points on the chain increases as it bends. As non-bonded attraction is usually weak, restoring force prevails for short chains. However, beyond a certain length, the filament develops buckling instability, which can be described as [43]

$$\rho_l \omega_n^2 = k_n^2(\kappa_0 k_n^2 - f_c), \tag{2.9}$$

where κ_0 is the length-independent, local bending stiffness. The critical buckling force f_c represents non-bonded attraction. Setting $f_c = 0$ in Eq. (2.9) restores Eq. (2.7). Since $k_n = c_n/L$, for a given f_c,

$$l_c = c_n\sqrt{\kappa_0/f_c}, \tag{2.10}$$

such that for $L > l_c$, $\omega_n^2 < 0$, *i.e.*, there is no stable wave solution. Since c_n grows with n, higher modes have larger l_c. From a linear fit to a plot of $X \equiv L^{-2}$ *vs.* $Y \equiv \omega_n^2 L^2$ we then retrieved l_c for the coiled-coils which was about 70 nm.

Since $l_c < l_p$ for coiled-coils, l_c rather than l_p is the length scale governing the chain conformation. A single tropomyosin molecule is about 42 nm, thereby limiting itself within the critical buckling limit. Even the 50-nm long coiled-coil stalk of kinesin has a hinge in the middle [55], so that the respective CC segments are well shorter than l_c.

2. Persistence length of a coiled-coil depends on the amino acid sequence

Earlier estimates of the l_p of coiled-coils in experiments were ∼150 nm, for the myosin S2 subdomain [56] and tropomyosin [11]. As mentioned above, l_p measured from

global conformation of the molecule may be affected by flexible points and we expect that a coiled-coil with an ideal heptad periodicity would have a longer l_p [12]. To further study the effect of amino acid composition on stiffness of a coiled-coil, we constructed 112-residue long straight coiled-coils whose heptad sequence was taken from the GCN4 leucine zipper. We introduced point mutations and calculated l_p for each mutant using NMA. Some of these mutants were unstable in MD at 300 K, so local fluctuation analysis could not be applied. As mentioned previously [12], stiffness and stability represent different parts of the energy landscape: While stiffness relates to the curvature of the conformational energy minimum, stability is a measure of the height of the energy barrier between the conformational minimum and other states. Thus, stiffness can be measured even for weakly stable mutants using NMA.

Table I shows that replacing hydrophobic residues with charged ones in d positions leads to a progressive decrease in stiffness with an increasing number of mutations. However, point mutations in the hydrophilic outer edge does not affect the stiffness significantly (bottom row in Table I). Thus while the knob-into-hole packing between hydrophobic faces of α-helices contributes to the stiffness of the coiled-coil, there is no significant contribution by residues on the outer side, including the inter-helical salt bridges formed between charged residues in e and g positions of the heptad. Instead, these salt bridges are important for maintaining stability of the coiled-coil by protecting the hydrophobic contacts among a and d residues from water [57].

In an earlier theoretical study by Wolgemuth and Sun [40], the adhesion energy between two α-helices was treated as constant under deformation of the coiled-coil. However, our calculation suggests that the steric knob-into-hole packing between hydrophobic side chains in a and d positions would provide a significant barrier to deformation, rendering l_p of a leucine zipper longer than experimental estimates of coiled-coils that contain regions of varied flexibility or broken heptads.

Table I. Persistence length l_p of leucine zipper coiled-coil and mutants. Mutated residues are marked in bold. l_p drops with an increase in the number of point mutations along the hydrophobic core (a and d positions), while there is no significant effect by mutations in exposed residues. As reported previously, in this range of coiled-coil sizes, there is a dependence of l_p on the length of the molecule, as can be seen by comparing wild-type (WT) values of 112- and 84-residue coiled-coils.

Size (no. of res)	No. of mutations	Residue No.	Sequence *a b c d e f g a b c d e f g a b c d e f g a b c d e f g*	K_b ($\times 10^{-27}$ Nm^2)	l_p (nm)
112	WT	1	MKQLEDKVEELLSKNYHLENEVARLKKL	2.04	493.43
		29	MKQLEDKVEELLSKNYHLENEVARLKKL		
		57	MKQLEDKVEELLSKNYHLENEVARLKKL		
		85	MKQLEDKVEELLSKNYHLENEVARLKKL		
	10	1	MKQLEDKVEE**K**LSKNYH**E**ENEVARLKKL	1.52	362.30
		29	MKQ**K**EDKVEE**K**LSKNYHLENEVAR**E**KKL		
		57	MKQ**K**EDKVEELLSKNYH**E**ENEVAR**K**KKL		
		85	MKQLEDKVEE**K**LSKNYH**E**ENEVARLKKL		
	14	1	MKQLEDKVEE**K**LSKNYH**E**ENEVAR**E**KKL	1.21	287.41
		29	MKQ**K**EDKVEE**K**LSKNYH**E**ENEVAR**E**KKL		
		57	MKQ**K**EDKVEE**K**LSKNYH**E**ENEVAR**K**KKL		
		85	MKQ**K**EDKVEE**K**LSKNYH**E**ENEVARLKKL		
	16	1	MKQ**K**EDKVEE**K**LSKNYH**E**ENEVAR**E**KKL	0.82	198.07
		29	MKQ**K**EDKVEE**K**LSKNYH**E**ENEVAR**E**KKL		
		57	MKQ**K**EDKVEE**K**LSKNYH**E**ENEVAR**K**KKL		
		85	MKQ**K**EDKVEE**K**LSKNYH**E**ENEVAR**E**KKL		
84	WT	1	MKQLEDKVEELLSKNYHLENEVARLKKL	1.41	343.01
		29	MKQLEDKVEELLSKNYHLENEVARLKKL		
		57	MKQLEDKVEELLSKNYHLENEVARLKKL		
	30	1	M**L**QL**L**D**L**V**LL**LLS**L**NYHL**L**N**L**VA**LL**KL	1.42	338.20
		29	M**L**QL**L**D**L**V**LL**LLS**L**NYHL**L**N**L**VA**LL**KL		
		57	M**L**QL**L**D**L**V**LL**LLS**L**NYHL**L**N**L**VA**LL**KL		

3. Tropomyosin has regions of varied flexibility

Previous crystallographic studies identified regions of varying radius and pitch across the length of tropomyosin [38], which suggests that it may not be mechanically uniform along the length. We investigated this by constructing the flexibility map calculated from a 10-ns MD simulation. Fig. 3 shows example distributions of ω_i. To check whether the simulation time was sufficient, we calculated Δs and the elastic moduli for select triads separately across 2.5 ns intervals during the production run (Fig. 4). Δs does not change notably over time (Fig. 4(a)). However, measured values of moduli vary more strongly over time. Yet it is not clear whether they fluctuate or drift (Fig. 4(b-d)). Although a longer MD simulation may reveal a clearer trend, distribution of moduli along the molecule (*i.e.*, as a function of the triad number) is already apparent and is not likely to change in any major way even in longer simulations. Besides, as mentioned briefly in our NMA on leucine zipper, at longer times, parts of the molecule may develop instability, which further complicates elasticity analysis.

The flexibility map reveals several interesting features that could be relevant to the function of tropomyosin. Part (a) of the figure in page 21 traces the distance between triads Δs averaged over the production run. It mostly stays within 7.35–7.55 Å, but increases to about 8.3 Å between triads 43–45. This is the region surrounding Glu218. Crystallographic studies show an increased radius in this region due to improper knob into hole packing [10, 42]. But Δs stays at the elevated value without any further increase (Fig. 4(a)). We also did not observe any notable unfolding of this region within the simulation time.

Comparing bending stiffness in two directions, if the molecule is depicted as a twisted tape, it is more flexible with respect to splay (l_{p1}) than to bending (l_{p2}) (parts (b,c) of the figure on page 21). The regions at Asp137 (d position) and Glu218

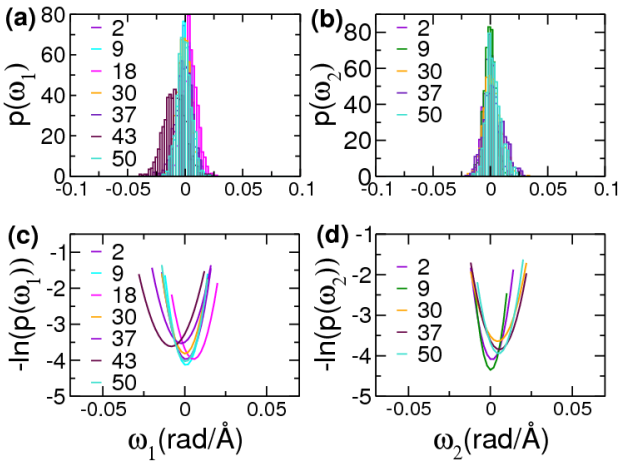

Fig. 3. Example distributions of (a) ω_1 and (b) ω_2, and (c,d) quadratic fits to their logarithm. Corresponding triad numbers are marked in the graph. While equilibrium curvatures ω_{01} & ω_{02} are generally 0 along the length of tropomyosin, at triad 43 (lowest rigidity region Fig. 5(b)) ω_{01} is about -0.01.

(a position) are highly flexible ($l_{p1} \sim 250$ nm, 116 nm, and $l_{p2} \sim 68$ nm, 196 nm respectively). As we see from Table. I, non-hydrophobic residues in the a & d positions reduce the stiffness of the coiled-coil. Improper knob into hole packing and increased spacing between the two α-helices as explained above, could be destabilizing the molecule at these regions, leading to increased flexibility.

Fig. 5(b) also reveals that along all the α-zones (orange filled circles), the putative actin binding sites (magenta stars) form local rigidity minima, which would assist with actin binding. These sites are composed of regular repeats of negatively charged residues in b and f positions of the heptad.[4] The enhanced flexibility is likely because of more polar residues occupying the a and d positions at the hydrophobic core (such as Tyr or Gln in the d position), which is consistent with our mutational analysis of leucine zipper (Table I). In the blocked state and further in the potentiated state, when the molecule moves into the actin groove, flexible actin binding interfaces would render the transition as a succession of local movements, so that the actin

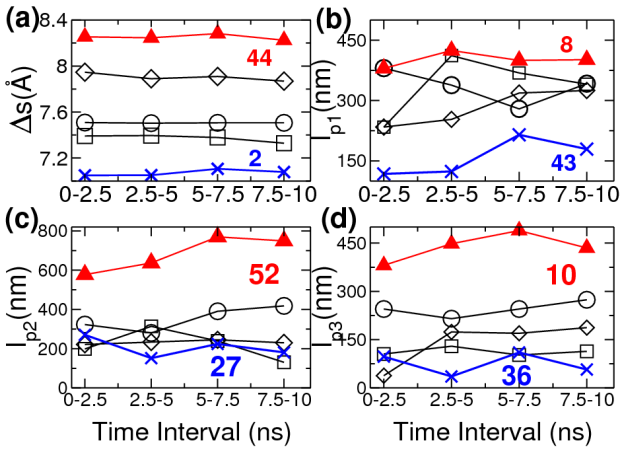

Fig. 4. Time evolution of Δs and l_{pi} for select triads. Averages were made over 2.5-ns intervals, for triad 15 (circle), 30 (square) and 45 (diamond). Data for triads that occupy the minimum (blue cross) and maximum (red triangle) in Fig. 5 are also shown, with triad numbers marked.

binding domains first reach the binding site, followed by the movement of the rest in a deformable way. Otherwise, the entire 40-nm long molecule would have to move on actin more as a rigid body, which would be a difficult task. Likewise, flexible domains would assist with reverse transitions out of the actin groove.

Overall, flexibilities in all three directions of deformation increase towards the C-terminus, including torsional rigidity, l_{p3} (Fig. 5). The globular head of the troponin complex binds to the region around triad 38, and the tail of troponin T binds to the C-terminal part of tropomyosin. The C-terminal half of tropomyosin interacts with the troponin complex, while the N-terminal half may need to move in a more independent fashion, which may be why the N-terminal part is stiffer. Furthermore, we did not find any particular reduction in flexibility in regions of alanine clusters. Thus, although they may induce a bend through improper knob-into-hole packing [4], they are not necessarily more flexible.

In this long coiled-coil, backbone hydrogen bonds in each α-helix do not stay

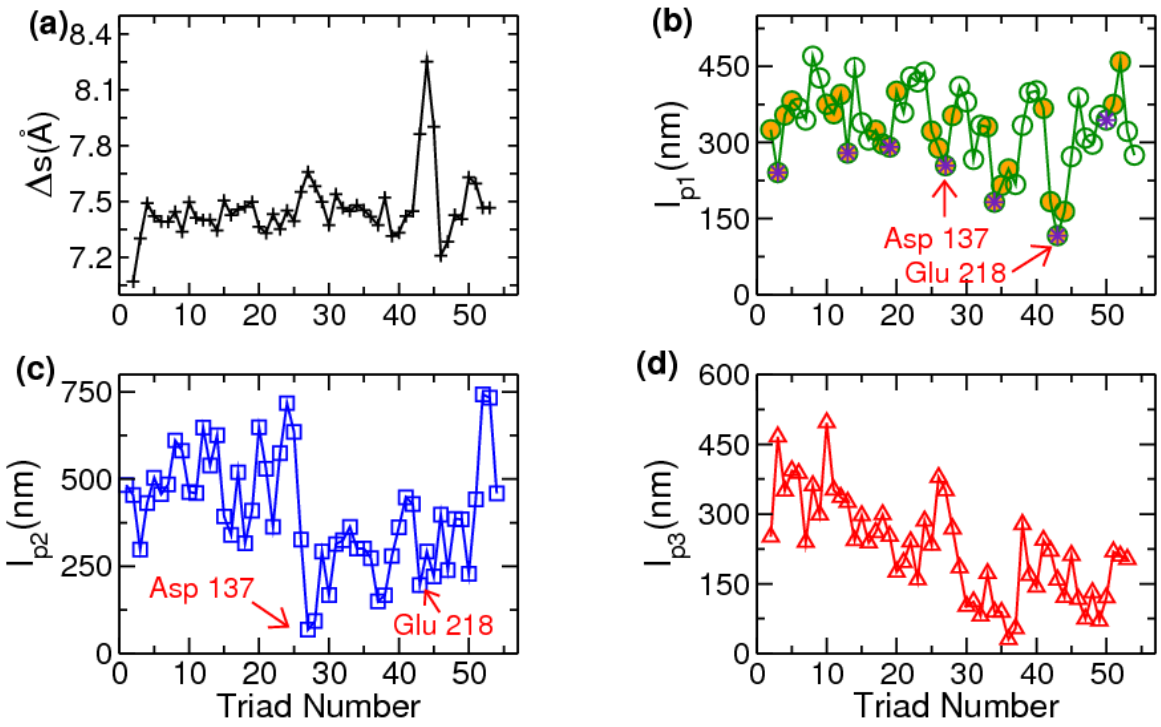

Fig. 5. Flexibility map of Tropomyosin. (a) Δs, showing a jump near the most labile region at Glu218 (triad 43). (b) l_{p1} regarding local splay deformation. Minimum occurs again at triad 43. Marked in orange represent α zones (*cf.*, Fig. 2), which contain actin binding sites (magenta stars) that are locally the most flexible. (c) l_{p2} regarding bend of the broad face. (d) l_{p3} representing torsional stiffness. Overall, the molecule is more flexible towards the C-terminus.

always formed throughout the simulation. Since earlier studies indicated its importance in elasticity of α-helices [12] and β-sheets [45], we plotted percentage of time that they are formed within five residues for each triad (Fig. 6). Hydrogen bonds mostly stay intact with occupancy higher than 80%. Regions where the hydrogen bond occupancy is low correspond to flexible regions shown in Fig. 4, such as triads 27 and 43. In these regions, deformation is accompanied by breakage of backbone hydrogen bonds, thus their elastic properties are likely nonlinear. Local persistence length, or stiffness κ_i (Eg. 2.3) are thus simple indicators of local lability, but these

regions should not be regarded as linearly elastic.

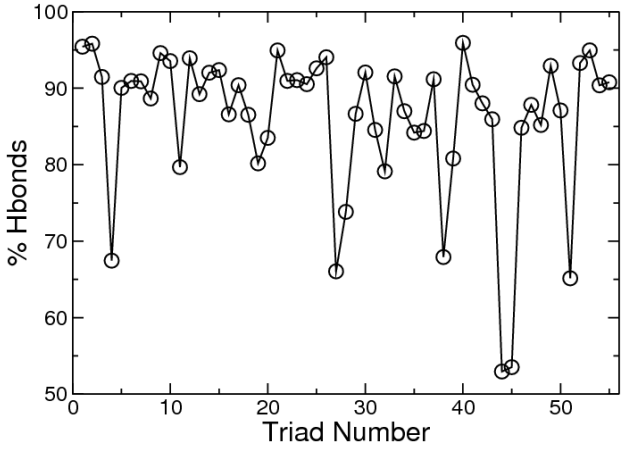

Fig. 6. Occupancy of backbone hydrogen bonds during the simulation. A cutoff distance of 2.4 Å was used to identify hydrogen bond formation. Regions of low hydrogen bond occupancy correspond to labile regions in Fig. 5.

E. Discussion

To a first approximation, a fibrous protein may be described as a uniform elastic rod. This is the case for filaments such as F-actin and microtubule, which are built by assembly of identical subunits. Earlier works suggested that elasticity of α-helices is roughly independent of the amino acid sequence, so they can be described as mechanically uniform [12, 39]. Coiled-coils, however, have stronger sequence dependence in its elasticity. We found that mutations in the a and d positions of the leucine-zipper coiled-coil affects its elasticity whereas those on other positions do not. Residues on a and d positions are typically hydrophobic and make knob-into-hole packing to hold the two α-helices together. Charged side chains on e and g positions form salt bridges, which, although important for stability [58], we find do not affect the elasticity signif-

icantly. Here we emphasize the difference between stability and flexibility: flexibility is determined by the local curvature of the conformational free energy minimum of the molecule, while stability is related to the height of the energy barrier to escape from this minimum. In mechanical terms, stability can be related to the yield strength. Also, as our hydrogen bond analysis in Fig. 6 shows, regions of high flexibility may not follow linear elasticity, so that their elastic moduli should be interpreted with caution.

Our analysis thus shows that long coiled-coils may not be treated as uniform elastic rods. Global persistence length or flexural rigidity would only be a coarse indicator. In the past, the coiled-coil neck of Rad50 has been observed to have regions of varying flexibility [59]. Common variations in the heptad periodicity such as stutters (deletion of 3 residues in a heptad) and stammers (deletion of 4 residues) have also been suggested to lead to local flexibility changes [60].

F. Conclusion

We find that tropomyosin, despite having a sequence that mostly follows the heptad periodicity, also has varied rigidities between functionally distinct domains across its length (Fig. 5). Overall the molecule is more flexible in the C-terminal region, and in the actin binding sites. Regions with charged residues at the hydrophobic face (Asp137 and Glu218) are particularly flexible. Such regular variations in flexibility by more than twofold may have implications in tropomyosin function, in particular for its movement along the actin filament. More structural data regarding tropomyosin bound to F-actin, and/or with other tropomyosin binding proteins such as the troponin complex, would further allow to elucidate how the distribution of elastic properties control the tropomyosin function.

CHAPTER III

HYSTERESIS BASED MECHANISM FOR THE DIRECTED MOTILITY OF THE NCD MOTOR*

A. Introduction

All motor proteins in the kinesin family share a similar ATPase catalytic core [61, 62]. Different motility behaviors are achieved by modifying subdomains such as those mediating track binding, force generation, and allosteric transduction of ATPase or mechanical events to other parts of the motor [16]. A prime example is the direction reversal in Ncd compared to that of Kinesin-1 [63, 64]. Unlike Kinesin-1 that has the motor head (MH) at the N-terminal end, the MH of Ncd is at the C-terminal end (called a C-terminal kinesin) [62]. Having nearly identical MH structures, the two kinesins differ mainly in the neck domain that connects the MH to the coiled-coil stalk [17]. Instead of a flexible *neck linker* as in Kinesin-1, Ncd has an α-helical *neck* that continues from the stalk and connects directly to the MH (Fig. 7). Mutational studies showed that directionality is partly determined by the neck domains: A chimeric Kinesin-1 with Ncd's neck showed microtubule (MT) minus-end directed motility whereas an Ncd with Kinesin-1's neck linker was plus-end directed, although motility in both cases was impaired [17, 18, 19, 20]. However, the underlying structural mechanism is still not well-understood, in particular for Ncd.

In x-ray structures of Ncd in the pre- and post-stroke states, the neck orients and makes contacts with the MH respectively in the the plus- and minus-end directions (Fig. 7 shows a list of contacts). However, the atomistic details of the transition

*Portions of this chapter are reprinted with permission from Sirish Kaushik Lakkaraju and Wonmuk Hwang, "Hysteresis based mechanism for the directed motility of the ncd motor", BioPhys.J, In press. Copyright 2011 by Cell Press.

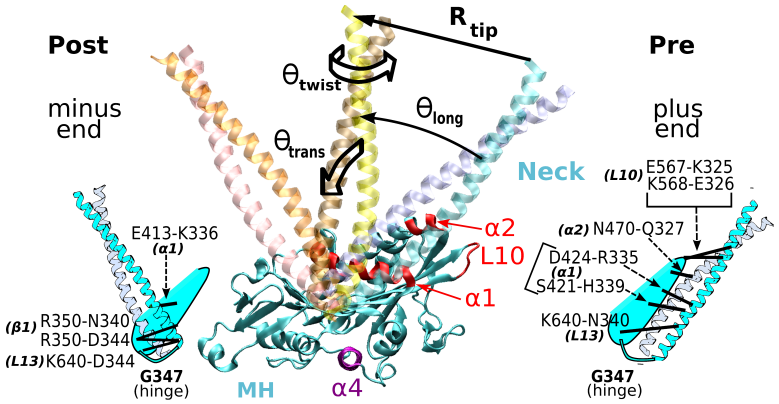

Fig. 7. Major MH-neck contacts of Ncd in the pre- and post-stroke structures. Hydrophobic contacts (not shown) play less specific role during the neck travel, and they are less conserved within the Kinesin-14 family (Table III). We call the α-helical coiled-coil ($\alpha 0$) (A295-R346) as the neck. The MT plus end is on the right. We measured the orientation of the neck using three angles, $\theta_{\rm long}$, $\theta_{\rm trans}$ and $\theta_{\rm twist}$. $R_{\rm tip}$ is the distance of the tip of the neck (the S297 C_α atom) from its pre-stroke position. When the MH is bound to the MT, $\alpha 1$ is approximately parallel to the MT axis and guides the neck motion by forming intermediate contacts with it. The relay helix $\alpha 4$ mediates the nucleotide-dependent 'see-saw' motion of the MH (Fig. 16). Atomistic structures are rendered by using VMD.

between the two states are unknown.

Here we use molecular dynamics (MD) simulations and structural analyses to elucidate the motion of Ncd's neck between the pre- and post-stroke orientations. We find several intermediate contacts between the neck and the MH not seen in x-ray structures representing the end states. For the neck motion, the $\alpha 1$ subdomain of the MH serves as a *guide rail*. The free energy profile along the path of the moving neck (potential of mean force; PMF) has an energy barrier in the forward motion. But lacking a strong directional bias, the neck moves mostly via diffusion guided by the intermediate contacts. In contrast, the PMF for the reverse motion (recovery stroke)

is very different and has no major energy barrier. This is due to the compliance of the protein that causes different intermediate bond patterns in the two directions of motion. Also, relaxation of the torsional strain of the neck in the post-stroke position partly drives the recovery stroke. The PMF profile is consistent with cryo-EM data showing a lower stability of the neck in the post-stroke position, and it explains a $\sim 10^{\circ}$ mismatch in the orientation of the neck in x-ray and cryo-EM structures [25]. The importance of residues in making the intermediate contacts correlates with the differences in MT gliding velocities of the corresponding mutants [26]. We also find that the mobile C-terminal tail of Ncd [28] may not play a direct role during the neck motion. The present results suggest that guided diffusion enables Ncd to walk under load, and hysteresis in energetics provides directionality in the mechanochemical cycle of Ncd.

B. Overview of methods and analyses

1. Structures used

We used x-ray structures of the Ncd dimer, Protein Data Bank (PDB) ID 1CZ7 [65], 1N6M [24], and 3L1C [28]. Both heads in PDB 1CZ7 have the neck in the pre-stroke orientation. In PDB 1N6M and 3L1C, the two heads of the dimer are respectively in pre- and post-stroke states. We used various combinations of these structures (Sec. C1 in Simulation Details and the table in page 50), and the pathways of the neck between the two conformations were all very similar. We also tested 10 mutants of Ncd to elucidate their behaviors in MT gliding experiments [26, 27] (table in page 50).

2. Choice of simulation modality for finding the transition path

To find the pathways of the neck between the pre- and post-stroke orientations, we performed multiple restricted-perturbation targeted molecular dynamics (RP-TMD) simulations [66] (table in page 50) and analyzed trajectories statistically (figure on page 51 and Sec.C1). In the original formulation of targeted molecular dynamics, transition between the initial and target structures is accomplished by applying a biasing force that reduces the RMSD between the two [67]. Since the biasing force can push the system over large energy barrier that is otherwise inaccessible, in RP-TMD, the magnitude and direction of the biasing force is regulated so that the transition follows the minimum free energy path more closely [68].

To test whether features from TMD trajectories are a part the minimum free energy path, for a representative trajectory, we performed explicit-water equilibrium simulations of the key intermediate structures without the bias of RP-TMD (Sec. 2). Additional structural analysis revealed that the observed trajectories also provide a sterically plausible picture (explained in Results).

In addition to RP-TMD [66, 68], we considered two other methods for characterizing the pathway of the neck: the normal mode superposition model [69] and the minimum energy path (MEP) method [70, 71]. In normal mode superposition model (NMSM), normal modes of two conformations of a protein are used to build a path between them [69]. However, for Ncd, the cumulative involvement coefficient which measures the contribution of a given set of normal modes to the conformational transition, was only 0.49–0.51 for the first 100 modes, in contrast to 0.9 for myosin V between the rigor and post-rigor conformations [69]. This implies that akin to the case of conformational changes in Kinesin-1 [72] normal modes may not be directly related to the motion of Ncd's neck.

Minimum energy path (MEP) is a path optimization technique, where a trial path between two conformations (such as via linear interpolation) is refined using conjugate peak refinement [70]. While it was successfully used to find conformational changes across the relay helix that are coupled to the switch II during the recovery stroke of myosin [71], we could not determine the first order saddle points for the neck rotation in Ncd, possibly because the neck diffuses over a large range while forming multiple intermediate contacts. Without incorporating the effect of thermal fluctuation, MEP may not offer a good picture of such a transition [66].

3. Orientation of the neck

We quantified the orientation and elastic deformation of the neck during the transition by adopting the methods we developed for the analysis of α-helical filaments [12, 73] (Chapter II, Section B4).

To measure the three angles defined in Fig. 7, we first assigned unit vectors along the axis of the neck; $\mathbf{u}_{\mathrm{pre}}$, $\mathbf{u}_{\mathrm{post}}$, and $\mathbf{u}$, respectively in the pre-, post-, and an intermediate state during the travel. If we denote the projection of $\mathbf{u}$ on the plane spanning $\mathbf{u}_{\mathrm{pre}}$ and $\mathbf{u}_{\mathrm{post}}$ by $\mathbf{u}'$, the angle between $\mathbf{u}_{\mathrm{pre}}$ and $\mathbf{u}'$ is θ_{long}, and that between $\mathbf{u}$ and $\mathbf{u}'$ is θ_{trans}. To measure θ_{twist}, we first translated the three conformations of the neck mentioned above so that their axes merge at the C-terminal end. The merging point of the three axes was used as a pivot for rotation. We rotated the intermediate structure (containing $\mathbf{u}$) towards $\mathbf{u}'$ by $-\theta_{\mathrm{trans}}$, followed by the rotation on the plane spanning $\mathbf{u}_{\mathrm{pre}}$ and $\mathbf{u}_{\mathrm{post}}$ by $-\theta_{\mathrm{long}}$. These operations align the neck in the intermediate state to the pre-stroke conformation without affecting rotation about its axis. For the neck each in the pre-stroke and intermediate conformations, we assigned local triads [73] (see the next section). θ_{twist} is the axial rotation angle of the triads at the N-terminal end of the neck between the intermediate and pre-stroke conformations.

In addition, rigid body rotation during the travel was quantified by measuring the axial rotation angles of the triads at the C-terminal end of the neck (close to the hinge). At the end of the travel, it was 10.5°. The net torsion in the neck is the difference between θ_{twist} and the rigid-body rotation angle, which is $\simeq 21.8°$ for the trajectory used in figure on page 37.

4. Deformation of the neck

Local Strain. We assigned local triads to individual α-helices and also to the neck coiled-coil as a whole. For the former, we assigned centroids of an α-helix with a 3-residue interval using C_α atoms in an overlapping manner (residue 297–299 for triad 1, 298–300 for triad 2, *etc*). In total there were 47 centroids on each α-helix. The arm $\mathbf{e}_3^{(n)}$ of the n-th triad ($n = 1 \cdots 46$) in the direction of the α-helical axis is defined along the line from the n-th to the $(n+1)$-th centroids. The second arm $\mathbf{e}_2^{(n)}$ is the unit vector normal to both $\mathbf{e}_3^{(n)}$ and a vector formed by connecting the n-th centroid to the second C_α among the three atoms defining the centroid. This fixes $\mathbf{e}_1^{(n)} = \mathbf{e}_3^{(n)} \times \mathbf{e}_2^{(n)}$.

The rotation angle between two successive triads about $\mathbf{e}_3^{(n)}$ represents the local twist, which can be found by calculating the corresponding Euler angle. Similarly, rotation angles about $\mathbf{e}_1^{(n)}$ and $\mathbf{e}_2^{(n)}$ quantify local bending in two orthogonal directions. The difference in the local twist angles between post- and pre-stroke structures provides the local torsional strain map shown in the part B of figure on page 52.

Triads for the coiled-coil were defined similarly. We located the mid-point between each pair of centroids assigned to the two α-helices. The axial arm $\mathbf{e}_3^{(n)}$ of the triad is the unit vector along the line joining two successive mid-points. The next arm $\mathbf{e}_2^{(n)}$ is perpendicular to both $\mathbf{e}_3^{(n)}$ and the line joining the corresponding centroids of the individual α-helices, and $\mathbf{e}_1^{(n)} = \mathbf{e}_3^{(n)} \times \mathbf{e}_2^{(n)}$. Local strain was measured using the

same method as for the individual α-helices. The difference in local torsional angles between the pre- and post-stroke structures of the neck is in the part A of the figure on page 53. The sum of local torsional angles lies in the 23.7-27.2° range for the PDB structures tested, which is consistent with the net torsional angle calculated as a difference between θ_{twist} and the rigid-body rotation angle in Sec. 3 above.

Torsional Energy. We isolated the neck (A295-R346) of PDB 1CZ7 and performed a 20-ns explicit-water MD simulation at 300 K. Denoting $\omega_i^{(n)}$ as the Euler angle divided by the length between triads n and $n+1$ of the coiled-coil with $\mathbf{e}_i^{(n)}$ as the rotation axis ($n = 1, \cdots, 46$), we measured its variance during the simulation, $\text{var}(\omega_i^{(n)})$. The local stiffness $\kappa_i^{(n)}$ of the coiled-coil is [73]

$$\kappa_i^{(n)} = \frac{k_B T}{\text{var}(\omega_i^{(n)})\Delta s} \tag{3.1}$$

where $\Delta s = 1.44$ Å is the average distance between triads. Using the torsional stiffness $\kappa_3^{(n)}$ and the measured local torsional angles of the traveling neck, we calculated the elastic energy in the part D of figure on page 52.

5. Tug-of-war sampling (TOWS)

For calculating the PMF along RP-TMD trajectories, we applied the tug-of-war sampling (TOWS) method that we previously used for the study of Kinesin-1 [22], with higher-order terms included for greater accuracy in the calculated force (free energy gradient) [74].

For a given RP-TMD trajectory, we took structures with a spacing in R_{tip} by about 2 Å. For each structure, we harmonically constrained the MH backbone in the regions that are in the vicinity of the neck (I349-C352 (β1), D410-Y475 (α1-α2), E560-S575 (β6-β7), and L630-V645 (α5-β8)) with a spring constant of 5 kcal/(mol·Å^2),

while fixing atoms in the rest of the MH that are further away. Instead of fixing, we also used harmonic constraints (spring constant 15 kcal/(mol·Å^2)) on the entire MH backbone, but the resulting potential of mean force (PMF) was similar (part C of the figure on page 55). Since using harmonic constraints is computationally more expensive than fixing the MH atoms, for other TOWS simulations we used the latter.

For sampling, we applied another harmonic constraint on the S297 C_α atom at the N-terminal tip of the neck with a spring constant of 5 kcal/(mol·Å^2). Using 2 or 15 kcal/(mol·Å^2) did not affect the result (part B of figure on page 55). At each value of $R_{\rm tip}$, we performed an 800-ps MD simulation at 300 K. Coordinates were saved every 1 ps. During the simulation, S297 C_α fluctuates around the center $\vec{r}_0$ of the harmonic potential. Denoting its deviation from $\vec{r}_0$ by $\vec{\delta r}$, the i-th ($i = 1, 2, 3$) Cartesian component of the force f_i on it at $\vec{r}_0$ is [74]:

$$\begin{aligned} f_i &\simeq \frac{k_B T}{\mathrm{var}(\delta r_i)} \langle \delta r_i \rangle + \sum_{j \neq i} F_{ij} \langle \delta r_j \rangle, \\ F_{ij} &\simeq -k_B T \frac{\mathrm{cov}(\delta r_i, \delta r_j)}{\mathrm{var}(\delta r_i)\mathrm{var}(\delta r_j)}, \end{aligned} \tag{3.2}$$

where $\langle \cdot \rangle$ denotes average over the simulation time, var() and cov() are respectively variance and covariance, and F_{ij} is the second-order partial derivative of the free energy in the i- and j-directions. PMF was obtained by projecting the negative of force vectors (free energy gradient) along the path defining $R_{\rm tip}$ and integrating. For some structures we extended the simulation time up to 5 ns, but 800 ps was sufficient, which can also be seen by the nearly identical PMF profiles obtained from the first and second half of the 800-ps simulation (part D of the figure on page 55). To further test the consistency of the PMF profile, we selected 11 intermediate structures from the explicit water RP-TMD simulation in the range $R_{\rm tip}$ = 16–40 Å over the first energy

barrier (*cf.*, **2** in the part B of the figure on page 54) and performed TOWS simulation using the GBSW implicit solvent model [75]. Consistent with PMFs obtained under other conditions, the energy barrier was preserved (part A of figure on page 55).

6. First passage time

We calculated the first passage time to diffuse over the PMF, which allowed comparison with experimentally measured stepping time of Ncd [15, 30].

Treating the neck coiled-coil as a cylinder with diameter $d = 15.3$ Å and length $L = 75.4$ Å, its rotational diffusion coefficient D_r with one end (G347) pivoted is [76, 77]

$$D_r = \frac{3k_BT}{4\pi\eta L^3}[\ln(p) + \delta_r] \simeq 3.01 \times 10^6 \text{rad}^2/s \tag{3.3}$$

where $p = L/d$ is the aspect ratio, $\delta_r = -0.662 + 0.917p^{-1} - 0.050p^{-2}$ is the correction factor accounting for the end effect, and $\eta = 8.56 \times 10^{-4}$ Ns/m^2 is the dynamic viscosity of water at 300 K.

If the neck does not interact with the MH and performs pure rotational diffusion with a pivoted end, the first passage time τ_{free} to reach $\theta_{\text{long}} = 73.2°$ is

$$\tau_{\text{free}} = \frac{\theta_{\text{long}}^2}{2D_r} = 271 \text{ ns} \tag{3.4}$$

In the presence of the PMF $U(x)$ as in the part B of the figure on page 54, the first passage time from $x = 0$ to reach $x = R_{\text{tip}}$ is [78]

$$\tau(R_{\text{tip}}) = \frac{1}{L^2 D_r} \int_0^{R_{\text{tip}}} dx\, e^{U(x)/k_BT} \int_0^x dy\, e^{-U(y)/k_BT}. \tag{3.5}$$

The first passage times for the two PMFs in the part A of the figure on page 55 are plotted in Fig. 15.

In a 3-bead single molecule assay of Ncd [15], the moving part is a 4.3-μm long

MT (25 nm in diameter), whose axial drag coefficient is $\zeta_{MT} = 4.67 \times 10^{-9}$ Ns/m [79]. In addition, there are two 1-μm diameter beads attached to the ends of the MT, whose drag coefficient is $\zeta_b = 8.07 \times 10^{-9}$ Ns/m each. Compared to these, the drag coefficient of the moving MH that has a 20.3 Å radius of gyration is 3.28×10^{-11} Ns/m, which is negligible. The axial diffusion coefficient of the MT is then $D_{MT} = k_B T/(\zeta_{MT} + 2\zeta_b) = 1.99 \times 10^{-13}$ m^2/s. The first passage time can be estimated using Eq. 3.5, with D_{MT} replacing $L^2 D_r$, which is $L^2 D_r / D_{MT} = 857$ times longer than those for the case when the neck moves without load.

C. Simulation details

1. Structure preparation and simulation protocol

We used PDB 1CZ7 [65], 1N6M [24], and 3L1C [28]. While PDB 2NCD [80] also represents the pre-stroke conformation, we chose 1CZ7 as one of its chains has the neck coiled-coil visible by 7 more residues. There are point mutations in 1N6M (N600K) and 3L1C (T436S). We replaced them back to the wild-type (WT) residues. They are in the microtubule (MT) binding domain (N600) and the nucleotide-binding pocket (T436), and do not interact with the neck. The missing loops were filled using MODLOOP [81]. None of these loops contact the neck except for L10 (E567–Q569). However, the L10-neck bonds (Fig. 7) broke during the motor head (MH) rearrangement phase of our restricted-perturbation targeted molecular dynamics (RP-TMD) simulation [66]. Furthermore, alanine mutations in L10 had 99% of the MT gliding velocity of the WT [26], suggesting that L10 plays little role. The MH conformation is controlled by a biasing potential during RP-TMD simulations, and during equilibrium simulations the MT-binding domains were harmonically constrained, thus a bound nucleotide has no influence and was not modeled.

We applied harmonic constraints with a force constant of 5 kcal/(mol·Å^2) to all atoms of the protein except the added loops and the WT residues restored in the PDB structures (N600 for 1N6M and T436 for 3L1C), and the system was energy minimized by 400 steps of steepest descent followed by 1000 steps of adopted basis Newton-Raphson methods. The system was heated in an implicit solvent (table in page 50) to 300 K with a rate of 5 K per 0.5 ps and equilibrated for 70 ps. During equilibration, velocities of atoms were rescaled if the simulation temperature deviated from 300 K by more than ±5 K. Subsequently, we applied harmonic constraints only to the protein backbone and further equilibrated the system for 200 ps. The integration time step used in this study was 1 fs. The equilibrated structures were used as the initial and target structures of the RP-TMD. For explicit-water RP-TMD simulations, our structures were prepared as follows: We built a solvation box of size 150 × 130 × 75 Å^3 around the pre- and post-stroke structures, and filled it with 45,973 water molecules. We then energy minimized and heated the system following the same protocol as mentioned above, with a periodic boundary condition applied to the simulation box. The structures were equilibrated for 500 ps with the backbone harmonically constrained with a force constant of 5 kcal/(mol·Å^2). These structures were used for explicit-water RP-TMD simulations.

For simulations of point mutations, side chains of the affected residues were replaced in the equilibrated structures as described above. The entire protein except for the mutated residues were harmonically constrained, and energy minimization and 100-ps equilibration MD at 300 K were performed to relax the mutated side chains. Similarly, in simulations where the neck has different conformations or sequences, the backbone of the replacing neck coiled-coil was aligned with that of the original one, followed by the energy minimization and equilibration procedure with harmonic constraints applied.

In RP-TMD, if the maximum allowed perturbation of the biasing potential (MAXF, in Å) is too small, the system does not reach the target structure. Conversely, too high values of MAXF leads to the system going over potential energy barriers that are otherwise inaccessible [66]. In our system, we determined MAXF= 0.05 or 0.1 to be adequate. With these values, time to reach the target structure (root mean square deviation (RMSD) with the target less than 0.8 Å) was 18–92 ps (table in page 50). The biasing potential of the RP-TMD was not applied to the loops constructed by MODLOOP. In RP-TMD trajectories, we considered a bond between residues to be formed when H and O atoms in respective side chains are closer than 2.4-Å. Coordinates were saved every 0.5 ps. In each coordinate frame, we calculated $R_{\rm tip}$ and made a list of MH-neck contacts. Across 10 simulations under each condition in Table II, we built a histogram of bonds with a 2-Å bin size in $R_{\rm tip}$, which was used to calculate the probability as in the figure on page 51.

2. Explicit-water simulation of intermediate structures in RP-TMD

We took four intermediate structures in one of the 1CZ7 (pre)→1N6M (post) RP-TMD simulation with MAXF= 0.1 and in the ACE2 implicit solvent (Table S1). We also took another structure from the 3L1C (pre)→3L1C (post) RP-TMD simulation. These five structures represent: (a) Right before the breakage of R335-D424 bond ($R_{\rm tip} \sim 22$ Å, before **2** in Fig. 8), (b) After the breakage of R335-D424 and formation of the K336-D424 bond ($R_{\rm tip} \sim 35$ Å), (c) Formation of the K336-Q420 bond ($R_{\rm tip} \sim 60$ Å), (d) After **3** in Fig. 8, with the K336-E413 bond ($R_{\rm tip} \sim 80$ Å). (e) From the RP-TMD of 3L1C, with the D344-K674 bond ($R_{\rm tip} \sim 7$ Å).

For each structure, we performed a 2-ns explicit water simulation with the backbone atoms in domains interfacing the MT ($L7$, $L11$ and $\alpha 4$) harmonically constrained with a force constant of 2.3 kcal/(mol·Å^2). The simulation followed the protocol men-

tioned above except that we used GROMACS [82] instead of CHARMM [83]. Also, we neutralized the net charge of the system by randomly replacing 26 water molecules with Na^+ ions. The particle mesh Ewald summation method [84] was used to calculate electrostatic interactions. In cases (a)–(d), the intermediate bonds kept forming and breaking, with an average occupancy of 87% during the 2-ns simulation time. However, the N340-Y426 in (a) broke at 0.1 ns, and K674-D344 in (e) broke at 0.2 ns, and they stayed broken throughout the simulation.

D. Results

1. Two-step RP-TMD for Ncd conformational change

With suitable choices for parameters in RP-TMD (Sec. C1), the neck moves between pre- and post-stroke structures. In Fig. 7, if the MH is treated as bound to the MT, the other unbound head of the Ncd dimer (not shown) passively moves with the neck without affecting its interaction with the bound head. This is consistent with the comparable MT gliding velocities of the monomeric and dimeric Ncd constructs [25]. Results discussed below are thus obtained using a single head as in Fig. 7.

TMD in general has a tendency to make transition to occur first in regions with large root mean square deviation (RMSD) between the initial and target structures [66]. When RP-TMD is applied directly between pre- and post-stroke structures (we performed 50 such simulations under different conditions), the neck rotates first, followed by rearrangement of the MH. In reality, however, when the neck is in the pre-stroke position, a chemical event such as ATP binding [25] or ADP release [24, 28] would cause the MH to change conformation and trigger the neck motion. It would thus be more natural for the MH to make the pre→post conformational change, followed by the transition of the neck. To test, we applied the biasing potential of the

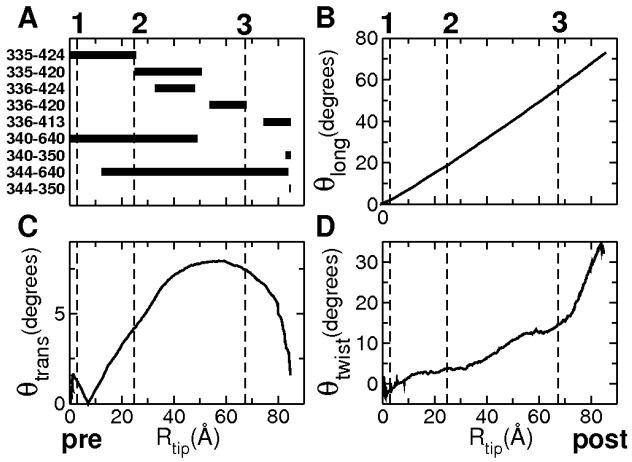

Fig. 8. A representative forward trajectory of the neck with PDB 1CZ7 as the pre- and 1N6M as the post-stroke structure. The same trajectory was used for the forward case in Figs. 10 and 12. (A) Major bond pattern. (B,C,D) Orientation angles defined in Fig. 7. Three vertical dashed lines numbered **1**–**3** mark the substep events noted in Fig. 12.

RP-TMD only to the MH to drive it to the post-stroke state while the neck remains in the pre-stroke position. This caused the K325-E567 and E326-K568 bonds (Fig. 7) to break, weakening the MH-neck contact. The neck consequently became more mobile, as can be seen by the increase in the range of thermal motion of the tip of the neck in 1-ns MD simulations, from 9.3 Å (before) to 17.6 Å (after MH rearrangement). Weakening of the MH-neck contacts by the MH rearrangement also leads to a reduction in the energy barrier that needs to be overcome for the neck to move, which is about 4.5 k_BT, down from 9.7 k_BT for the case when the neck moves first (see below). Thus, the forward RP-TMD trajectories discussed below are obtained through two steps so that the MH rearranges first, then the neck rotates to the post-stroke position. For the reverse motion from post- to pre-stroke state, we found that it is more likely for the neck to move first, followed by the MH rearrangement to the pre-stroke conformation (see below).

2. Substeps during the neck motion

For the forward motion of the neck, we performed 70 RP-TMD runs using two different implicit solvent models under different conditions, and one explicit-water simulation (Table II). We sought features that are common to these RP-TMD trajectories. Most notably, instead of a free swing, the neck forms and breaks a series of bonds with the MH. The main players on the neck are R335 and K336, which interact with E413, Q420 and D424 of α1. Closer to the G347 hinge, N340 and D344 interact with K640 in L13 and R350 in β_1 (Fig. 7).

We recorded a bond formation event as a function of the distance of the tip of the neck from its pre-stroke position, $R_{\rm tip}$ (Fig. 7). An example trajectory is shown in Fig. 8A: After partial breakage of the MH-neck contacts by the MH rearrangement, the Q327-N470 and H339-S421 bonds, and other hydrophobic contacts (between F329, M333 and L471, W473; not shown) break soon after the neck starts to move. At $R_{\rm tip} \simeq 25$ Å, R335 breaks from D424 and forms a transient bond with Q420 until $R_{\rm tip} \simeq 51$Å. K336 that does not interact with the MH in the pre-stroke state, follows the neighboring R335 and sequentially forms and breaks bonds with D424 and Q420. At $R_{\rm tip} \simeq 67$ Å, K336 breaks away from Q420. Subsequently, at $R_{\rm tip} \simeq 74$ Å the K336-E413 bond forms, followed by others that are in the post-stroke x-ray structure (Fig. 7). K640 switches contacts with N340 (pre) and D344 (post) in an overlapping manner (Fig. 8A).

Since nearly all residues forming intermediate contacts participate in the pre- or post-stroke contacts (Fig. 7), intermediate contact formation is a natural consequence of the neck switching its binding partners between the two states. The order of forming the contacts is determined mainly by the geometric proximity between the residues of the moving neck and those of the MH (*cf.*, part A of the figure on page 52),

which should be overall preserved in different simulation trajectories. The probability of forming a bond as a function of R_{tip} indeed shows a common pattern (Fig. 9). The precise values of R_{tip} at which a given bond is formed or broken are likely to vary even among steps that Ncd actually makes. The only way the neck can avoid the intermediate contacts would be a large transverse motion away from the MH, which is unlikely.

While the above shows that intermediate contacts are sterically plausible, due to the biasing potential of RP-TMD, they might also be a result of poor relaxation of the system as the neck motion is rapid, lasting less than 200 ps (Table II). To test whether they stay formed without the biasing potential of RP-TMD, we took 4 structures from RP-TMD trajectories and performed regular explicit-water simulations at 300 K. The identified contacts persisted during the 2-ns simulation time (Sec. E2). An exception was the N340-Y426 bond, which broke within 0.1 ns, hence was excluded in the above analysis.

Aside from polar or charged residues that mediate intermediate contacts, hydrophobic residues M414, P417 and L418 at the N-terminal half of $\alpha 1$ form a groove through which M343 travels (Fig. 10A), further highlighting its role as a guide rail. The same set of contacts were observed during the reverse travel (post→pre) in 61 RP-TMD runs (Fig. 9H-J and Table II). The main difference from the forward travel is in the range of R_{tip} over which a given bond is present (see below).

3. Twist of the neck towards the post-stroke state

We quantified the orientation of the neck using the three angles shown in Fig. 7 (Sec. B3). The longitudinal angle θ_{long} grows monotonically to 73°, as in x-ray structures (Fig. 8B). The transverse angle θ_{trans} for the motion of the neck away from the MH, grows no more than 7.9° (Fig. 8C). This reflects that the neck maintains

contact with $\alpha 1$ (Fig. 10A) whose 7°-bend is responsible for the bell-shaped profile of θ_{trans}. Interestingly, θ_{twist} for the axial rotation of the neck, grows to 32.3° in the post-stroke position, which may indicate untwisting of the left-handed coiled-coil in the post-stroke state.

We further analyzed the distribution of angular strains in individual α-helices of the neck in the post-stroke relative to the pre-stroke structure (Fig. 10B and Sec. B4). Bending angles were at most 2° whereas torsional angles varied more: The α-helix of the neck belonging to the MT-bound head (Fig. 10B, 'Bound') is strained in V301-L303 (11°), K325-E326 (9°), and K336 (7°). The second α-helix extending into the unbound MH (Fig. 10B, 'Unbound') is also strained, with a maximum at S331 (10°). Among these, only the K325-K336 region contains residues that interact with the MH (Fig. 7). Other domains may develop strains via a non-local response to perturbation in α-helical coiled-coils [85]. Since the torsional angles in Fig. 10 are positive, the right-handed α-helices in the post-stroke state are *over*-twisted, which is consistent with unwinding of the coiled-coil as the two have opposite chirality [79].

Distribution of torsional strains across the neck coiled-coil in the post-stroke structures had a similar trend with an overall positive twist (Fig. 11A). The cumulative torsion on the tip of the neck is 24° (Fig. 11B). The remaining $\sim 8°$ in θ_{twist} (Fig. 8D) is achieved by rigid-body axial rotation of the coiled-coil with G347 as a pivot (Sec. B4). G347 becomes α-helical in the post-stroke state, as the Ramachandran plot shows (Fig. 10C). Note that torsional strains (Fig. 10B and Fig. 11A) are present in x-ray structures, and they are not outcomes of simulation. RP-TMD shows that the torsional strain increases more steeply for $R_{\text{tip}} > 60$ Å (Fig. 11B), similar to θ_{twist} in Fig. 8D.

To find the strain energy, we measured the local elastic moduli of the coiled-coil by applying a fluctuation analysis method that we developed for studying the coiled-

coil protein tropomyosin (Sec. B4) [73]. On average, its stiffness in two orthogonal bending directions is 8.28×10^{-28} Nm^2 and 7.63×10^{-28} Nm^2 each, and for torsion, 4.96×10^{-28} Nm^2. These are about 1/3 of those for the leucine zipper [12, 73]. This is consistent with experiments showing a lower stability of the neck [86]. Using these results, we found that the neck is about 2.5 k_BT higher in torsional energy in the post-stroke structure (Fig. 10D).

4. Free energy changes during the forward transition

Existence of intermediate contacts suggests that the forward motion of the neck is not a free diffusion. To quantify its energetics, we used the TOWS simulation (Sec. B5) [22, 74]. For a given RP-TMD trajectory, we selected snapshots in ∼2-Å intervals of R_{tip}. The number of snapshots varied between 45–57, depending on the trajectory used. For each snapshot, we applied a harmonic constraint to the tip and performed a 0.8-ns MD while holding the MH. The positional fluctuation of the tip can be used to calculate the force generated at the center of the harmonic constraint (negative of the free energy gradient) [74].

In contrast to the strong directional bias found for the cover-neck bundle of Kinesin-1 [22], the force vectors do not point in the post-stroke direction (Fig. 12A). Their large axial components are due to the high extensional modulus of the neck coiled-coil [73, 87] and they do not contribute to the rotation of the neck. Only components along the direction of travel are relevant, which provide the PMF when integrated along the path (circles in Fig. 12B). Using R_{tip} as a reaction coordinate allows to compare PMFs for different RP-TMD trajectories where paths of the neck differ slightly. Upon the pre→post MH rearrangement and partial breakage of bonds with the MH, the PMF rises by ∼4 k_BT. This energy is likely provided by an ATPase event in reality. We denote the MH rearrangement as the first substep (**1** in Figs. 8 and

12B). Next, a major 8.5-k_BT energy barrier (4.5 k_BT after the MH rearrangement) is imposed by the R335-D424 bond (**2** in Figs. 8 and 12B), the breakage of which marks the beginning of a downhill free energy gradient until the K336-Q420 bond breaks (**3** in Figs. 8 and 12B). Last, the PMF goes uphill as the neck reaches the post-stroke orientation.

If the neck transitions ahead of the MH rearrangement as predicted by the more "direct" TMD, an energy barrier of nearly 9.7 k_BT (Fig. 14) is encountered. This higher barrier is caused by R335 having to break its bonds with both D424 & Q420 in the pre-stroke MH, in contrast with the two-step TMD where due to the MH-rearrangement R335 encounters D420 a little later in the neck travel. Further, at the post-stroke, the net free energy difference between the two-step and direct TMD paths is nearly 7 k_BT, which arises from the neck un-twisting by nearly 25° past **3** (in the two-step TMD, the untwisting of the neck by about 18° past **3** (Fig. 8) is more "gradual"). It is thus unlikely that in the forward motion, the neck travels ahead of the MH.

To ensure these features are robust, we verified the following (Sec. B5): The PMFs calculated using two other RP-TMD trajectories including one in explicit-water, had similar profiles (Fig. 13A), and the type and strength of constraints used in the TOWS had no major effect (Fig. 13B,C). Quality of sampling was also good, as the PMFs obtained using the first and the second half of the 0.8-ns sampling time matched well (Fig. 13D). Similar profiles of PMFs in these tests also suggest that the RP-TMD trajectories closely follow the minimum free energy path.

The PMF is higher on the post-stroke side, which agrees with the higher mobility of the neck [25]. An energetically favored post-stroke position is **3** in Fig. 12B, not at the end of travel. This also agrees with the report where ∼10° rotation of the neck in PDB 1N6M gives a better fit to the cryo-EM density map [25]. In 15% of the

RP-TMD trajectories, the neck at **3** was further stabilized by another R335-E413 bond (Fig. 9C,G). Nevertheless, the **3**→post transition may occur through thermal fluctuation, whereby the neck is captured and stabilized by the bonds with the MH.

We estimated the first passage time for the neck to diffuse across the PMF from the pre-stroke position (Sec. B6). Assuming the neck to be a cylinder 15.3 Å in diameter and 75.4-Å long, its rotational diffusion coefficient with one end pivoted is 3.01×10^6 rad^2/s [76, 77]. The first passage time [78] is then 2.32–8.25 μs for the pre→**3** transition and another ∼1.92–11.53 μs for the **3**→post transition (Fig. 15). By comparison, a single-molecule experiment of a full-length Ncd dimer estimates a 200∼400 ms stepping time [15]. This is likely an upper bound due to the 50-ms dynamic response time of their system and the large drag on the moving MT and the trapping beads while Ncd remains stationary in the 3-bead assay. As in the experiment, if we regard the tip of the neck to be stationary and the MH translocates a 4.3-μm long MT with two beads 1-μm in diameter attached, the estimated first passage time is 1.98–7.07 ms (pre→**3**) and 1.64-9.88 ms (**3**→post), which would be even longer if the full-length stalk were used in simulation. On the other hand, the first passage time with a flat PMF is only 271 ns when the neck is assumed to move with a stationary MH, and 243 μs when the MT is translocated as in the single-molecule experiment. Therefore, the neck moves to the post-stroke position likely through a series of sub-steps driven by thermal fluctuations rather than by pure diffusion.

5. Hysteresis in the neck travel

As mentioned above, the MH rearrangement upon an ATPase event precedes the forward travel of the neck. In the reverse motion, it is more likely that the neck moves prior to the MH rearranging back to the pre-stroke state: If the MH has the pre-stroke conformation before the recovery stroke (*cf.*, Fig. 6D→E), it may re-

bind to the MT site where it detached from. To test, we performed two types of RP-TMD simulations of the reverse motion. In one, the neck first moves, then the MH rearranges to the pre-stroke state (neck first; 'NF' in Fig. 12B). In the other, the order is reversed and the MH rearranges first ('HF' in Fig. 12B). The trajectories differ mainly in the values of $R_{\rm tip}$ at which a given bond is formed and broken (Fig. 9). However, the net free energy change for the NF case matches better with that of the forward PMF than the HF case does, since the NF PMF ends at 0.1 k_BT at $R_{\rm tip} = 0$ Å (open triangle in Fig. 12B) whereas the HF PMF ends at 3.0 k_BT (solid triangle). Furthermore, the HF PMF is mostly uphill below $R_{\rm tip} \simeq 30$ Å, as the R335-Q420 and K336-D424 bonds that persist near the end of motion, impede the return of the neck to the pre-stroke position (Figs. 9H *vs.* 9I). These results indicate that the recovery stroke of the neck precedes the MH rearrrangement. Below we use the NF case for the reverse motion.

The forward and recovery strokes differ qualitatively since there is no energy barrier in the latter. This difference originates from the compliance of the protein: During the forward motion, since the R335-D424 bond persists until **2**, these residues become strained (Fig. 12C, lower left panel). After the bond breaks, the distance between R335 and D424 rapidly increases as they relax. During the reverse motion, the bond can thus form again only near the end of the transition (Fig. 12C, $\diamond$ to $\star$). This can also be seen in explicit-water RP-TMD simulations (Figs. 9B *vs.* 9J). The strained state of the R335-D424 bond near **2** is not an outcome of the biasing force of RP-TMD, since it was also maintained during the TOWS simulation without any bias on the bond. Neither did it break during a 2-ns equilibrium simulation in explicit-water (Sec. E2). Although the R335-D424 bond may eventually break in longer simulations, its importance is consistent with a large reduction in the MT-gliding velocity of a mutant without the bond [26] (see Concluding Discussion).

Another notable feature of the reverse PMF is the nearly monotonic downhill gradient in the post→**2** region. To see whether this is related to the torsional strain of the neck, we changed its conformation in the post-stroke orientation to that of the pre-stroke state. When the replacement includes G347, the extra α-helical turn at this position in the post-stroke state (Fig. 10C) disappears. In either case, the calculated PMF does not decrease in the post→**3**, but in **3**→**2** the PMF still decreases (Fig. 11C), suggesting that the torsional strain of the neck affects the PMF in the **3**–post region. The opposite trends of the forward and reverse PMFs between **2** and **3** are likely collective results of multiple bonds involved in this region (Fig. 9).

6. Role of the C-terminal tail

Since available x-ray structures align reasonably well with cryo-EM maps [25], and the neck and α1 are spatially separated from the MT, the present results are unlikely to be affected by the presence of MT. A domain that might have a potential influence is the C-terminal tail(C-tail; V666-K700) that is mostly invisible in available structures. Earlier we hypothesized that it may play a dynamical role similar to the cover-neck bundle formation in Kinesin-1 [22], which is supported by the recently published PDB 3L1C [28]: The C-tail is visible up to K674 and it points to the MT plus end, analogous to the neck linker of Kinesin-1 in the MH-docked state. In RP-TMD of 3L1C, K674 forms a bond with D344 of the neck after the MH rearrangement. But this bond is unstable and breaks within 0.2 ns in an explicit water simulation, unlike the contacts between the MH and α1 that are present in all solvent models tested (Sec. E2). We constructed a model of a MT-bound Ncd, with the C-tail and the mobile E-hook domains at the C-terminus of tubulins [88] added (Fig. 17). Depending on whether the MH is in the ADP or ATP-like state, initially, C-tail out of the MH points to either the MT minus or plus end (see below). In both cases, due to its length and

positive charges, the C-tail can interact with the negatively charged E-hook of β-tubulin, suggesting that this interaction may assist with the binding of Ncd to the MT. Indeed, a chimera without the C-tail fails to bind [20, 28].

The neck linker-like conformation of the C-tail in 3L1C is coupled to the tilting of $\alpha 4$ out of the MH (Fig. 16). This 'see-saw motion' occurs in many kinesin families, to make room for the neck linker docking in the ATP state [89, 90, 91]. In Ncd, $\alpha 4$ does not interact with the neck, and its orientation does not affect the RP-TMD trajectory, as can be seen in our simulations with PDB 1N6M and 3L1C that respectively have $\alpha 4$ in orientations before and after the see-saw motion (Fig. 9C,G). This may reflect the weaker coupling of the Ncd stepping event to the nucleotide state [30]. By comparison, the C-tail is more clearly defined in x-ray structures of another Kinesin-14 motor, Kinesin-like calmodulin binding protein (KCBP) [92, 93, 94]. Its 51-residue long C-tail consists of the 10-residue 'neck mimic' that is homologous to the neck linker of Kinesin-1, a calmodulin binding helix, and the negatively charged C-terminal coil [94]. In the ATP-like state, the neck mimic binds to the MH [92, 93]. However, Ncd and KCBP belong to different sub-families, Kinesin-14A and 14B, respectively [62], and their C-tails have no sequence homology. It is thus unclear how much of the properties of the KCBP C-tail are applicable to Ncd. On the other hand, key residues mediating the MH-neck contacts are conserved between the two, and they have comparable MT gliding velocities (table on page 60). Although further study is necessary, other than mediating the MT binding, the C-tail of Ncd might interact with the neck at most for the initiation of the forward motion in the ATP state, as hypothesized for KCBP [92].

E. Concluding discussion

1. Validation of the RP-TMD result

Since RP-TMD uses a bias to drive conformational change, the resulting trajectories do not represent the actual motion of the neck [66, 68]. They instead reveal the likely minimum free energy path along which the neck performs diffusion. Since the full energy landscape is unknown, whether the trajectories indeed follow the minimum free energy path should be validated by considering the possible effect of the bias in RP-TMD and also by considering whether they are physically and sterically plausible. As explained in Results, the common pattern of intermediate contacts over a large number of RP-TMD simulations (Fig. 9 and Suporting Table II) suggests that they are unlikely to be artifacts of RP-TMD. This is further supported by their persistence in TOWS and other equilibrium simulations (Sec. E2). The α1 guide rail assists with a longitudinal motion of the neck, and the intermediate contacts mainly follow the placement of residues in α1 (Fig. 10A). In simulations of mutants without these contacts, the neck indeed swivels away from the MH (see below). Furthermore, RP-TMD has a tendency to select a path that is more accessible in the vicinity of the initial structure. The fact that the forward PMF starts with an energy barrier (Fig. 12B) instead of following the downhill path of the reverse PMF near $R_{\text{tip}} = 0$ Å suggests that the hysteresis behavior represent a property inherent in the Ncd structure ather than a consequence of using RP-TMD. Besides, the present results are consistent with a wide range of structural and motility data.

2. Ncd mechanochemical cycle

Combining the present result and previous experiments, a possible mechanochemical cycle of Ncd is proposed (Fig. 18). At the beginning, binding of the MH to the MT

leads to the release of ADP (Fig. 18A) [95, 96]. In the nucleotide-free state, the neck points to the MT plus end [25], and binding of an ATP leads to a conformational change that breaks the head-neck contacts at least partially. It also has been suggested that ADP release leads to the rotation of the neck (**"?"** in Fig. 18B) [28, 29]. Regardless of whether the neck rotation is initiated by ADP release or ATP binding, in the ATP state, the mobile neck reaches the post-stroke position via guided diffusion (Fig. 18C). The MH detaches from the MT upon ATP hydrolysis [97, 25] or release of γ phosphate [95] (Fig. 18D). Finally, recovery stroke advances the detached MH to the MT minus-end direction (Fig. 18E). Since the moving neck interacts mainly with the $\alpha 1$ guide rail, whose conformation does not depend on the nucleotide state, the proposed mechanisms for the forward and recovery strokes of the neck (Fig. 18, B→C and D→E) are likely to hold regardless of which ATPase event initiates the transition. Furthermore, a recent single-molecule analysis indicates that the motion of the neck is not as strongly coupled to the nucleotide state as in Kinesin-1, for 30% of the stepping events were MT plus-end directed [30].

3. Guided diffusion and hysteresis

Diffusion guided by intermediate contacts is an efficient strategy for generating unidirectional motion. Conformational relaxation after the breakage of the R335-D424 bond will make it difficult to re-form (Fig. 12C). The neck instead forms other bonds after **2**, to reach **3** (Figs. 8A and 9). A similar diffusion and binding mechanism may move the neck beyond **3** at the expense of an increased torsion. Compared to free diffusion, the intermediate contacts can reduce the burden imposed by external load during the forward travel. This scenario is also energetically plausible since ADP release and ATP binding would respectively provide a few to several k_BT [79], which are comparable to the changes in the PMF of the neck (Fig. 12B). While the

recovery stroke may be initially powered by the accumulated torsion of the neck, below $R_{\mathrm{tip}} \sim 30$ Å it may reach the pre-stroke position via diffusion without a bias (Fig. 12B, NF). Since the recovery stroke occurs in the unbound Ncd (Fig. 18E), it may not require as much tolerance to load. These are consistent with the slower speed and smaller step size of the plus-end directed stepping event of Ncd suggested from experiments [30].

4. Comparison with mutants and other Kinesin-14 members

The role of the intermediate contacts can also be seen in the effects of mutations on motility. In a study where MT gliding velocities of several Ncd mutants were compared [26], more than 50% reduction in velocity was observed in alanine mutations of key residues that are involved with intermediate contacts, including R335, K336, Q420 and K640. Blocking intermediate contacts would reduce velocity because the neck has to diffuse over a wider range. By comparison, mutants of E567 and K568 that break bonds with the neck upon MH rearrangement in RP-TMD (Fig. 7), had 99% of the WT velocity. The Y426A mutant had 57% of the WT velocity, even though the N340-Y426 bond was not maintained in explicit-water MD simulation (Sec. E2). Y426 is at the border between $\alpha 1$ and $\beta 3$ of the central β-sheet of the MH core, so it may be structurally important.

Table II. Conditions used in RP-TMD simulations. The pre- and post-stroke conformations of 1N6M or 3L1C are respectively from chain A and B in the PDB file. The simulation stopped at time t when the root-mean-square deviation of the system from the target structure fell below 0.8 Å. 'HF' and 'NF' refer to two different ways for the reverse motion mentioned in Fig. 12. References for mutations are mentioned in the text. Ncd-ran12 is a 12 residue substitution where the 335RKELHNTVMDLR346 in the WT neck was replaced by 335ESGAKQGEKGES346. For the LZ-neck, the Ncd neck residues 320ELETCKEQLFQSNMERKELHNTVMDLR346 were replaced with that of a leucine zipper sequence 320KLMKQLEDKVEELLSKNYHLENEVARLK346. MAXF: Maximum allowed perturbation in RP-TMD.

Motor	Direction of Motion	MAXF (Å)	Pre (PDB)	Post (PDB)	Solvent model	Time (t) (ps)	No. of Runs
WT	Forward (pre→post)	0.05	1CZ7	1N6M	ACE2	87.3±5.2	10
					FACTS	79.4±10.2	
		0.1	1CZ7	1N6M	ACE2	53.3±7.1	
					FACTS	45.2 ± 12.4	
					TIP3P	207	1
		0.1	1N6M	1N6M	ACE2	41.8 ± 9.7	10
					FACTS	30.4± 12.4	
			3L1C	3L1C	ACE2	49.8 ± 6.9	
	Reverse (post→pre)	0.05 (NF)	1CZ7	1N6M	ACE2	52.7 ± 7.2	10
		0.1(HF)	1CZ7	1N6M	ACE2	57.8 ± 11.3	
		0.1(NF)	1CZ7	1N6M	ACE2	47.3 ± 15.2	
					FACTS	42.4 ± 12.4	
					TIP3P	143	1
			1N6M	1N6M	ACE2	62.7 ± 8.2	10
			3L1C	3L1C	ACE2	54.5 ± 23.1	
R335A	Forward (pre→post)	0.1	1CZ7	1N6M	ACE2	37.2 ± 5.7	10
N340A						38.7 ± 3.5	
N340K						47.2 ± 12.6	
D344A						56.2 ± 11.4	
K640A						47.2 ± 9.2	
K640N						62.5 ± 7.6	
R335A/K336A						44.2 ± 7.1	
N340K/K640N						55.3 ± 20.3	
Ncd-ran12						29.8	1
LZ-neck						20.2	1
D344A	Reverse (post→pre)	0.1(NF)	1CZ7	1N6M	ACE2	47.1 ± 11.2	10
N340K/K640N						42.8 ± 9.1	
Ncd-ran12						34.1	1

t

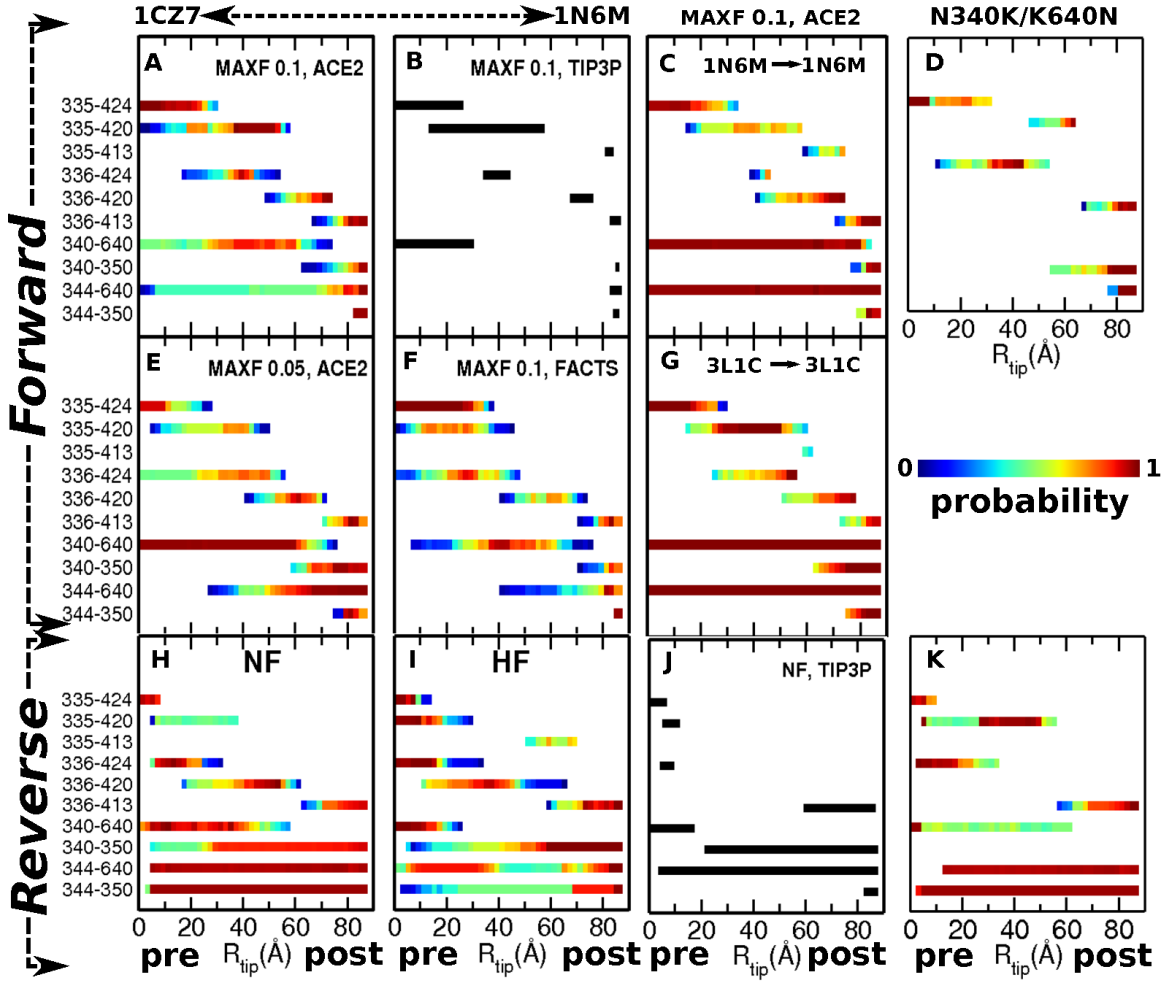

Fig. 9. Probability of forming MH-neck contacts in RP-TMD under various conditions (Table II and Sec. C1). The structures used are PDB 1CZ7 (pre) and 1N6M (post), except (C) 1N6M, (G) 3L1C used for both pre- and post-stroke structures. (D,K) A double mutant N340K/K640N. (A-G): Forward, (H-K) Reverse trajectories. The maximum perturbation allowed in RP-TMD (MAXF) is 0.1 except (E) MAXF=0.05. Solvent model used is ACE2 except (F) FACTS, and (B,J) explicit-water. In (H,J,K), the biasing potential of RP-TMD is applied to the neck first ('NF') whereas in (I) it is applied to the MH first ('HF') (*cf.*, Fig. 12B). In (B,J), bond patterns are for single explicit-water simulations. The R335-D424 bond persists over a wider range in forward than in reverse trajectories, which is responsible for the barrier at **2** in the forward PMF (*cf.*, Fig. 12B).

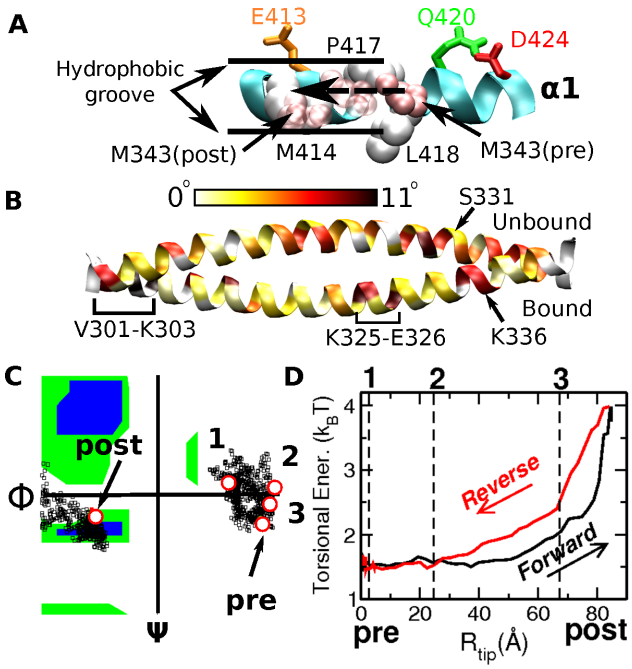

Fig. 10. Guidance and conformational changes of the neck. (A) $\alpha 1$ as a guide rail. R335 and K336 of the neck sequentially form bonds with D424, Q420 and E413 (Fig. 8A), whereas M343 of the neck moves in the hydrophobic groove formed by M414, P417, and L418. (B) Distribution of torsional strains in the α-helices of the neck in the post- relative to the pre-stroke structure. (C) Ramachandran plot for the G347 hinge during the forward motion. Substeps **1**–**3** in Figs. 8 and 12 are marked by circles. G347 becomes α-helical past **3**. (D) Increase in the torsional energy of the neck in the post-stroke state, notably after **3** where the cumulative torsion increases (Fig. 8D and Fig. 11B). The reference structure for measuring the elastic energy is an isolated and equilibrated neck coiled-coil, which causes a $\sim$1.5 k_BT basal energy when the neck is attached to the MH.

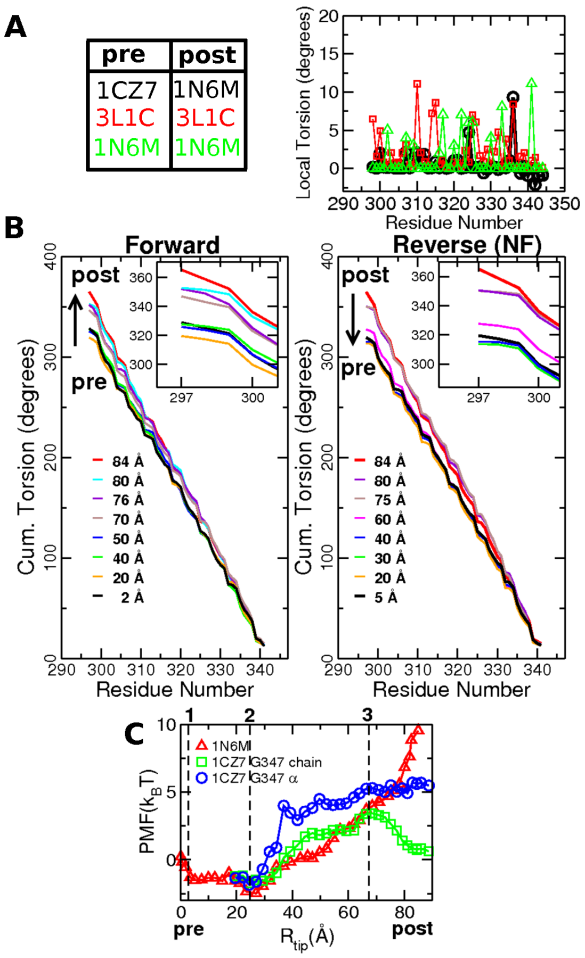

Fig. 11. Torsional deformation of the Ncd neck and its contribution to the PMF. (A) Distribution of torsional strains on the neck coiled-coil with different pre- and post-stroke structures used. Vertical axis is the local twist angle of the neck in the post-stroke relative to the pre-stroke structure. Overall positive angles suggest unwinding of the left-handed coiled-coil. (B) Cumulative torsional angle at different values of $R_{\rm tip}$ for the trajectory in Figs. 8 and 12. Torsion develops mostly in the region $R_{\rm tip} > 60$ Å. (C) Contribution of the torsion of the neck to the PMF. Red triangle: PMF for the WT (Fig. 12B, rev NF). Green square: Neck in the pre-stroke conformation of PDB 1CZ7 (lacking torsional strain) used for the post-stroke conformation, including G347 in the random-coil state (*cf.*, Fig. 10C). Blue circle: With the 1CZ7 neck, but G347 in the post-stroke α-helical conformation. The sharp change in PMF between **3** and the post-stroke state is absent in the chimeras. The PMF curves for the chimeras were vertically shifted to match with the WT PMF at $R_{\rm tip} = 19.5$ Å.

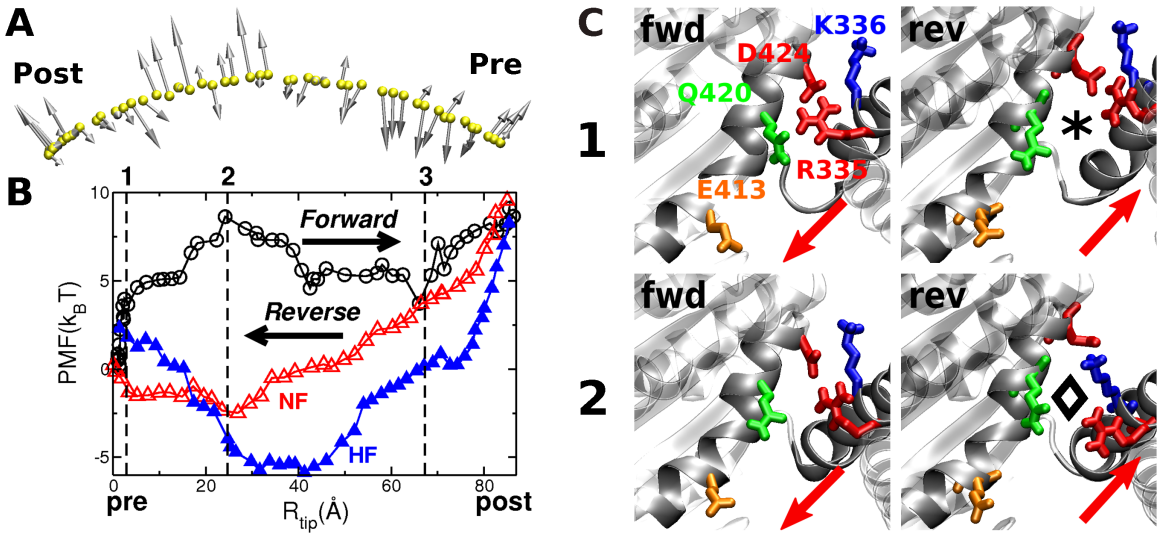

Fig. 12. Energetics during the neck travel. (A) Force vectors obtained using the TOWS simulation at the tip of the neck for the trajectory in Fig. 8. Forces range between 6–43 pN. Viewing direction is the same as in Fig. 7. (B) PMF curves obtained by integrating the components of the force vectors along the direction of travel, for forward (*circle*) and reverse (*triangle*) trajectories. Substeps marked **1**–**3** coincide with those in Fig. 8. For the reverse motion, two types of trajectories were used: the MH rearranges prior to the neck travel (head first; HF, *solid triangle*), and conversely, the neck travels first (NF, *open triangle*). (C) Comparison between forward and reverse trajectories at $R_{\rm tip}$ = 5 Å (near **1**) and 21 Å (before **2**). Arrow indicates the direction of travel. In the reverse trajectory, the R335-D424 bond is formed only when the neck almost finishes its travel ($\diamond$ *vs.* $\star$).

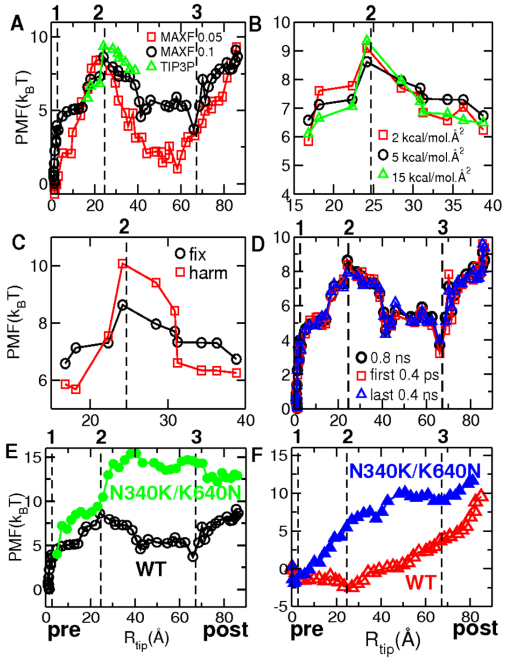

Fig. 13. Testing the reliability of the calculated PMF for WT (A–D), and PMF of the double mutant N340K/K640N (E,F). (A) Comparison between PMF curves calculated using different TMD trajectories in the ACE2 implicit solvent (MAXF=0.1 and 0.05), and in explicit water. For the explicit-water trajectory, TOWS was carried out using the GBSW implicit solvent model, which is known to match the analytic Poisson-Boltzmann result within 2% error. (B) PMF curves around the barrier **2** obtained using different spring constants in TOWS. (C) Using harmonic constraints on the MH backbone instead of fixing the domains of the MH that do not interact with the neck. Although changes in energy is somewhat different, the overall profile including the location of the peak is the same. (D) Dividing the 0.8-ns sampling interval into two and calculating PMF for each, which resulted in very little change. For the TIP3P simulation in (A), and the simulations in (B) and (C), the sampling was performed only around the neighborhood of **2**, and the corresponding PMFs were vertically shifted to compare with the reference PMF. (E) Forward and (F) reverse PMFs of the double mutant N340K/K640N.

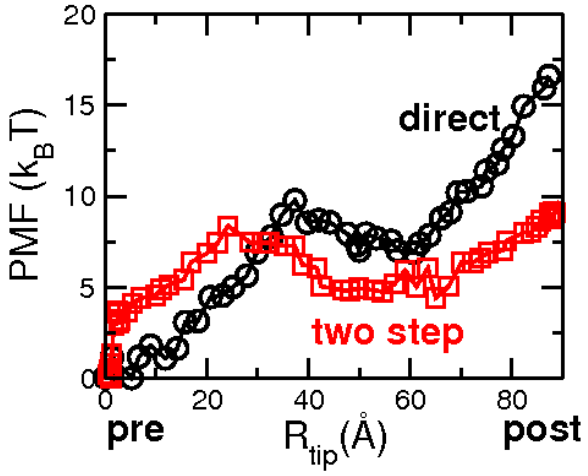

Fig. 14. PMF curves from the one-step TMD where the neck travels ahead of MH-rearrangement. Two-step TMD curve from Fig. 12B is shown for comparison.

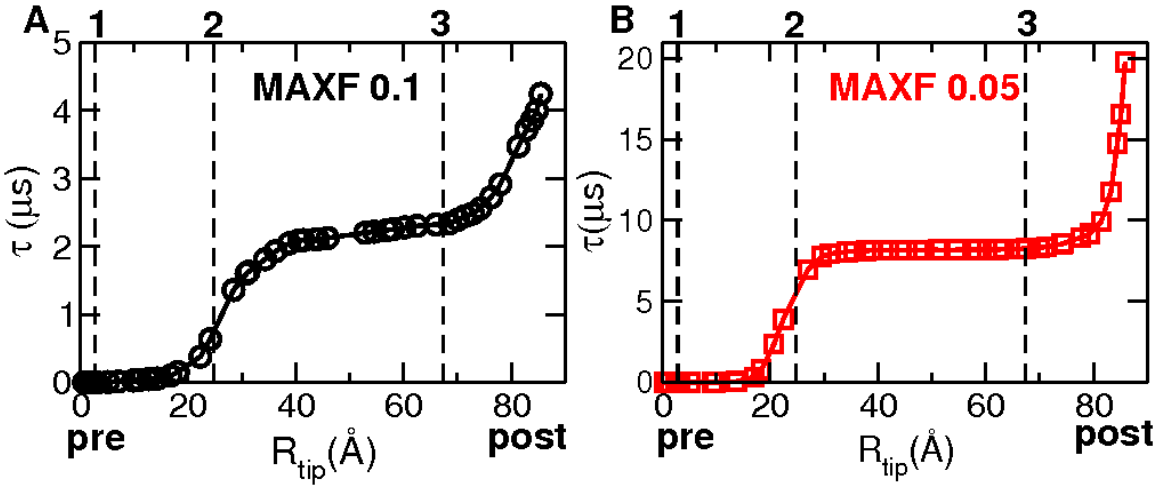

Fig. 15. First passage time for the Ncd's neck to reach R_{tip} from the pre-stroke position. (A) MAXF= 0.1, (B) MAXF= 0.05. The PMF used are from Figs. 12B and 13A.

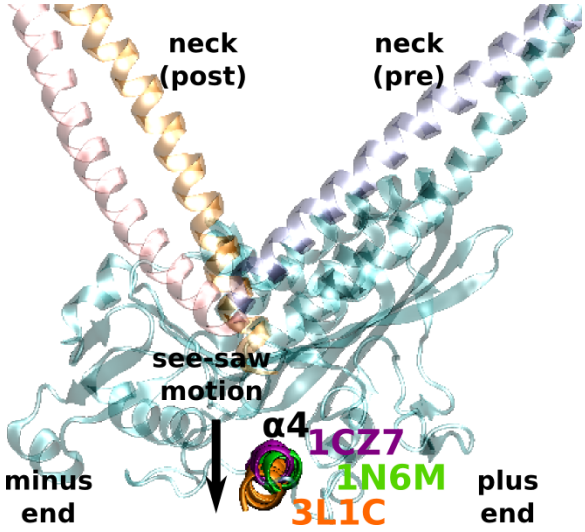

Fig. 16. Conformation of $\alpha 4$ in different crystal structures. Viewing direction is the same as in Fig. 7. In PDB 3L1C, $\alpha 4$ is further away from the MH (the see-saw motion), and the C-terminal tail points to a direction similar to the docked neck linker in Kinesin-1. Both PDB 1N6M and 3L1C have the neck in the post-stroke orientations despite the difference in the conformation of $\alpha 4$. Using either of them as a post-stroke conformation in RP-TMD does not affect the result significantly (Fig. 9C,G).

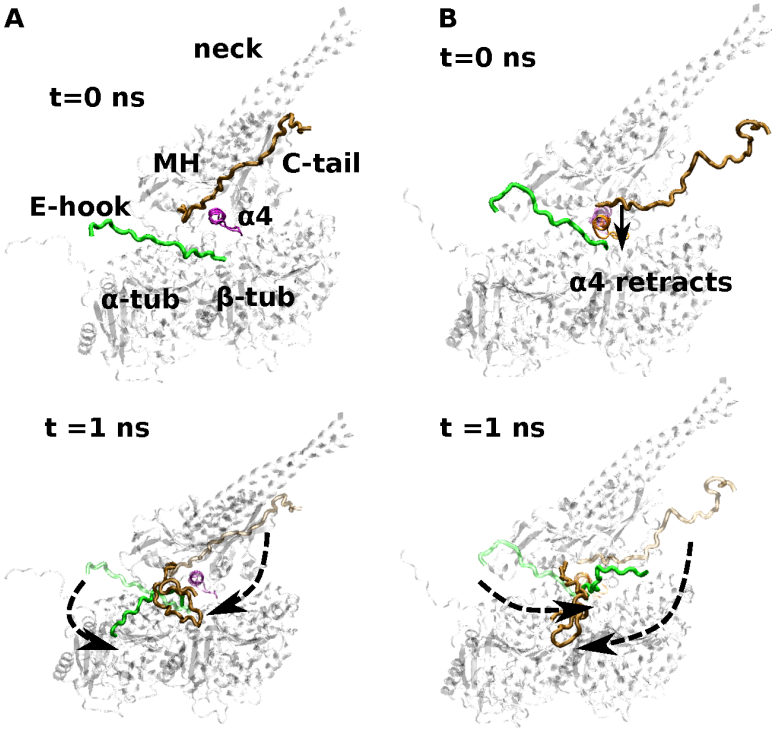

Fig. 17. A model of MT-bound Ncd with C-tail and the MT E-hooks. MH conformation used are (A) PDB 1CZ7 (ADP state) and (B) PDB 3L1C (ATP-like) (Fig. 16). Orientation of the motor head on the tubulin dimer is based on PDB 2P4N. The tubulin dimer structure is from PDB 1JFF. After building the system, a 1-ns all-atom explicit water simulation was performed using GROMACS (333455 atoms in total) to relax the structure. In (B) the MT plus-end pointing C-tail moved and made contact with the E-hook of β-tubulin. C-tail conformations at the beginning and the end of the simulations are colored ochre, while an intermediate configuration where the contact with the e-hook begins in the simulation is colored cyan. Likewise E-hooks at the beginning and end of the simulations are colored green, while the intermediate configuration is colored pink.

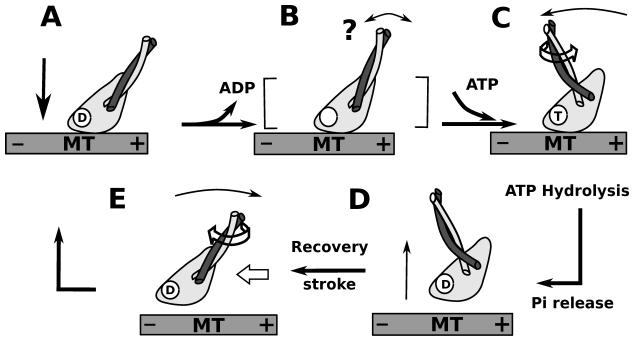

Fig. 18. Possible Ncd mechanochemical cycle. (A) MH of an Ncd dimer in the ADP state binds to the MT (the unbound head is not shown). (B) ADP releases during or after binding to the MT. Whether the motion of the neck is initiated by the ADP release or ATP binding is unclear (marked by **?**) (C) ATP binding leads to travel of the neck to the post-stroke side. (D) The MH detaches upon ATP hydrolysis or γ phosphate release. (E) The unbound MH advances to the minus-end direction via recovery stroke driven by torsional relaxation and diffusion.

Table III. Comparison of the amino acid sequence and MT gliding velocities ($v_m(\mu\mathrm{m/min})$) in the Kinesin-14 family. Residues corresponding to those forming the MH-neck contacts in Ncd are highlighted in boldface, and colored blue and red. On these sites, residues that deviate from those of Ncd are shown in italic. In Kar3, K453 replaces E413 of Ncd that forms the K336-E413 bond (Fig. 7), which may be related to its slower MT gliding velocity. Residues of Ncd forming hydrophobic contacts between the MH and the neck are colored in green. They show poorer conservation except for L418, which faces the central β-sheet of the MH core (Fig. 10A). Sequence comparison with Kinesin-1 (Kin-1) shows critical differences in the sites where the neck interacts. Note that Ncd's neck matches with a C-terminal region of the stalk of Kinesin-1.

	Neck	MH					v_m
	α_0	β_1	α_1	α_2	$L10$	$L13$	
Ncd	325**K E Q** - - - L **F** Q S N **M** E - - - - - - - - - - **R K** E - L **H N** T V **M D** 344	349**I R** 350	413**E M** V S **P L** I **Q S** A L **D** G **Y** 426	470**N L** G **W** 473	567**E K** 568	639 S **K** 640	8.4-15.2
Kcbp	805 *Y K* **Q** - - - - - - E Q V L - - - - - - - - - - **R K** R - Y *Y* **N** T I E **D** 820	815**I R** 816	884**E** D T K Y L V **Q S** A V **D** G **Y** 897	941**N** - K Y 943	1038 *Q T* 1039	1113 A **K** 1114	8-12
Cho2	234 *A* **E Q** G D R L H G L E M E - - - - - - - - - - **R R** R - L **H N** Q L Q **E** 256	261**I R** 262	336**E** E I S M L V **Q S** A L **D** G **Y** 352	396 *G* Q G W 399	501 *A* **R** 502	581 A **K** 582	1.0-8.4
Pkl1	446 *Q Q L* - - - E R R N E D M Y N K L L A E E I I R **R R** K - L **H N** D I Q **E** 475	480**I R** 481	554**E** E I S Q L I **Q S** A I **D** G **Y** 567	608 *E* K G W 611	708 *R T* 709	791 A **K** 792	2.76
Kar3	363 *N* **E** *I* - - - L I K E E T V - - - - - - - - - - **R R** T - L **H N** E L Q **E** 382	387**I R** 388	453 *K* E V G Q L V **Q S** S L **D** G **Y** 466	508 *T* K G W 511	613 *K T* 614	692 S **K** 693	1-2
Kifc1	289 *G* **D** *R* - - - L Y G L E M E - - - - - - - - - - **R R** R - L **H N** Q L Q **E** 307	312**I R** 313	390**E** E I A M L V **Q S** A L **D** G **Y** 403	451 *G* Q G W 454	553 *A* **R** 554	633 A **K** 634	
Kifc2	385**K** *T* **Q** - - - L S E G N Q A - - - - - - - - - - *P P* T G C *S G* R L L **E** 404	409**I R** 410	465 *R* Q L E P A V *L* **S** C L *Q* **G Y** 478	518 *G* T G G 521	616 *P* **R** 617	701 T *T* 702	
Kifc3	411 *I* **E** *E* - - - V N S N N Q E L L R K Y R R E L Q L **R K** K - C **H N** E L V *R* 439	444**I R** 445	505 *Q* E V Q A L I *T* **S** C I **D** G *F* 518	561 *A* S D W 564	659 *S T* 660	701 T *T* 702	
Kin1	701 *V* **E Q** - - - Q I Q S H - - - - - - - - - - - - **R** *E* T - H *Q K* Q I S *S* 718	9**I K** 10	64**D** C A K K I V *K D* V L **E G Y** 78	123 *D* E N L 126	218 *Q T* 219	294 C **R** 295	42

We performed RP-TMD simulations of 10 mutants from Refs. [26] and [27] (Fig. 9D,K and Table II). Under the assumption that these mutations do not affect the Ncd structure significantly, our results generally agree with the correlation between the loss of key intermediate contacts and the reduction in the MT gliding velocity. Comparing the sequences of the Kinesin-14 family and available MT-gliding velocities (Table III) also suggests that residues forming the intermediate contacts, such as R335, K336, N340, and D344 of the neck, and those in $\alpha 1$, $L13$, and $\beta 1$ of the MH, are highly conserved. In contrast, residues that break contacts after the MH rearrangement in RP-TMD, and those making hydrophobic contacts, show less conservation.

N340K/K640N. A previous study showed that mutants N340K, K640N, or N340K K640N have bidirectional motility with gliding velocities of axoneme-MT complexes comparable to that of the WT [27]. We performed RP-TMD simulations of the N340K/K640N double mutant and calculated the PMF both for the forward and reverse travel. Swapping Asp and Lys between 340 and 640 resulted in loss of the bond between them in the forward travel and loss of the N340-R350 bond in both directions. Furthermore, the K336-Q420 bond did not form, indicating that point mutations can lead to changes in bond formation by other residues (Fig. 9D,K). PMFs for the N340K/K640N mutant are also different, rising nearly monotonically towards the post-stroke side without a clear barrier (Fig. 13E,F). The neck may thus simply fluctuate with the pre-stroke position as the bottom of the energy well. The loss in directionality in the neck motion may then allow bi-directionality in the MT gliding assay via a cooperative effect among multiple motors [27, 33].

N340A. The double mutant H339A/N340A had a moderate reduction in the MT gliding velocity, 79% of the WT value [26]. Since the H339-S421 bond breaks quickly

after the MH-rearrangement, loss in the N340-K640 bond (Figs. 8A and 9), may have a greater effect on motility. We thus performed RP-TMD simulations of the N340A mutant. In 8 out of 10 RP-TMD runs, the D344-K640 bond that overlaps with N340-K640 in WT (Figs. 8A and 9) remained intact, so that the MH-neck contact involving K640 is maintained. This may be responsible for the moderate reduction in the MT gliding velocity.

Other mutants. We also performed RP-TMD simulations of eight other mutants including those with the neck replaced by the leucine-zipper or a random sequence (Ncd-ran12) (Table II) [26]. Overall, the contacts involving mutated residues were broken without affecting other bonds. In the case of leucine-zipper sequence, only N340 in the neck was conserved, which preserved the N340-K640 bond. However, with all other contacts lost, in a 1-ns regular MD simulation in the ACE2 implicit solvent, the neck detached from the pre-stroke position and swiveled. In Ncd-ran12, although all residues of the neck forming bonds with the MH are lost, alternative S336-D424 and K339-D424 bonds formed until $R_{\rm tip}$ $\sim$13.4–24.7 Å. However, these bonds were not enough to hold the neck in the pre-stroke position, and it also detached from the MH in a 1-ns MD.

5. Implication for motor mechanism

In non-motile enzymes, transition paths between different conformations may have less functional significance compared to the end-state conformations. However, since translocating motor proteins work out of equilibrium, hysteresis in conformational transitions may be required for directed motility. In the case of Kinesin-1, the cover-neck bundle formation drives the forward motion [22, 23], whereas the neck linker unbinds likely through the see-saw motion of $\alpha 4$ in reverse [91, 90]. The power- and recovery strokes of myosin occur in different nucleotide and actin-binding states

[98]. Likewise, Ncd's neck moves in two different phases of the mechanochemical cycle (Fig. 18), and hysteresis is achieved by the compliance of the protein, which is similar in origin to the adhesion energy hysteresis between macromolecular surfaces [99]. Elucidating hysteresis in the motility cycle will be important for understanding other translocating motors as well.

CHAPTER IV

HOW DIRECT NEIGHBOR-NEIGHBOR INTERACTIONS REGULATE MICROTUBULE DECORATION AND COOPERATIVITY BY NCD

A. Introduction

For its walking step, Ncd attaches to the MT (template MT) through one of its ADP-bound MH [95]. In its pre-stroke position, the neck points to the plus-end of the MT (part b of figure on page 81). With the neck extending directly from the stalk to the MH, any motion of the neck is amplified by the stalk. An ATPase activity in the MH that attaches to the MT (bound-MH), triggers a large 70° rotation of the neck and the second MH (unbound-MH that attaches passively to the neck) to a minus-end pointing post-stroke position (part c of figure on page 81). Using molecular dynamics, we noted that the neck rotation is driven by guided-diffusion where the coiled-coil neck forms a series of intermediate contacts with the bound-MH [100]. When a second MT (load/transport-MT) is bound to the Ncd through the N-terminal cargo-binding region, it slides over the first MT as the neck-stalk rotate. A subsequent second ATPase activity at the end of this rotation, detaches the bound-MH from the MT and the neck returns to the pre-stroke position as a part of the recovery stroke. With the N-terminal end attached to the transport MT, the neck-stalk's return to the pre-stroke position brings the ADP-bound MH (that detached from the MT), closer to the next MT binding site towards the minus-end of the template MT. The Ncd can then attach to the new MT binding site through the same ADP-bound MH that it used for its previous step. The role of the second MH in the walking step was hence unclear as chimera Ncds with a single MH and a coiled-coil stalk recorded a gliding velocity comparable to the wild-type dimer [25].

Since they are non-processive, and the forces on the sliding (transport-)MTs were greater than those generated by a single Ncd [31], it was proposed [33] that a group of Ncds act cooperatively in sliding an MT. Also, an attractive interaction of about 1.5-1.7 k_BT between neighboring motors on an MT was shown through experiments [35, 36]. Theoretical models predicted the force generated by a group of Ncds and the effect of this cumulative force on the filament [33, 34]. However, these models did not incorporate the effect of this attraction on the motility of a motor. Also unknown was the physical basis of the cooperativity and the attraction between these neighbors.

To understand the physical basis of both the cooperativity and attraction between motors on an MT, we structurally analyzed two Ncd dimers with various combinations of pre- & post-stroke neck positions that occupy immediate neighboring sites on an MT lattice (figure on page 81). We considered three types of neighbors: longitudinal, neighbors along the same protofilament ($D_{i,j}$,$D_{i,j+1}$); lateral, neighbors across adjacent protofilaments ($D_{i,j}$,$D_{i+1,j}$); and at seam ($D_{13,j}$, $D_{1,j+2}$ & $D_{13,j+1}$, $D_{1,j+2}$), where the 3-start helix of the MT leads to an offset between lateral neighbors. Across $D_{i,j+1}$ and $D_{i,j}$, steric repulsions between the neck-stalks of both the dimers induce a synchrony driving longitudinal neighbors to execute their neck-stalk rotation together. Between lateral neighbors, strong attraction exists between the surface loop L2 of a pre-stroke UB-MH of $D_{i,j}$ and the nucleotide binding pocket (NBP) in the bound-MH of $D_{i+1,j}$, thereby impeding the motility in both the dimers. Across the seam, with the 3-start helix introducing a lag, each dimer interacts with two lateral neighbors. Strong attractions between the neck (and the bound-MH) of $D_{1,j+2}$ and the unbound-MHs of $D_{13,j}$ & $D_{13,j+1}$ impede motility in all the three dimers. It is hence unlikely that dimers will occupy MT sites when neighboring sites across a seam are occupied. Thus, although the function of the unbound-MH in the walking step of a single Ncd is likely minimal [25], because off-axis neighbors interact via their

unbound-MH, it plays a critical role in regulating the MT decoration by a group of Ncds. These results are useful in developing "rules" that will guide temporal and spatial decoration of an MT filament by a group of Ncds such that their cooperativity is retained without compromising the motility.

B. Methods

Ncd attaches to the MT through only one of its MH [95] (called bound-MH, hereafter). In crystal structures 2NCD [80] and 1CZ7 [65] (Protein Data Bank, PDB ID) the neck is pre-stroke, while in 1N6M [24] and 3L1C [28], in one of the chains the neck is post-stroke with respect to its MH [25]. For our structural analysis and simulations described below, we used 1CZ7 and 1N6M to represent the pre- & post-stroke positions respectively. It maybe noted that the coiled-coil neck extends directly from the stalk. Hence, although the structural analysis is based on the part of the neck visible through crystal structures (A296-E346), the interactions observed across the necks of two dimers maybe extended to a scenario that involve the stalk as well. When relevant, we will therefore refer to the rigid neck and stalk coiled-coil as neck-stalk.

1. Ncd neighbors on an MT lattice constructed from tubulin-dimers

To study the interactions between neighbors on an MT, we constructed a 13 protofilament MT using the α-β tubulin dimer crystal structure 1JFF as follows: First, we built a protofilament by translating 1JFF along the Z-axis by 8 nm. Successive protofilaments were constructed by translating the previous protofilament by 0.92 nm and rotating by 27 $^\circ$ along the Z-axis. The 0.92 nm stagger between neighboring protofilaments induces a 3-start helix difference between the 1st and the 13th protofilament on the MT and the interface is called a seam (figure on page 81).

Crystal structure 2P4N [101] captured a Kinesin-1 MH (1MKJ) [102] at the α-β tubulin dimer junction (1JFF) [88]. Structurally MH of kinesin-1 and Ncd are very similar, with a root mean square deviation (RMSD) $\sim$ 2 Å. Thus, we super-posed the bound-MH of Ncd onto the kinesin-1 MH in 2P4N to get the orientation of the neck and the unbound-MH with the tubulin-dimer (figure on page 81) shows a pre-stroke Ncd sitting on the tubulin-dimer with the neck pointing to the plus-end after the MT bound-MH was super-imposed with the kinesin-1 MH). Superposing bound-MH of 1N6M onto 1MKJ in 2P4N shows the neck and the unbound-MH pointing to the minus-end of MT (parts b and c of figure on page 81).

The indices i, j of an Ncd dimer $D_{i,j}$ on an MT lattice stand for the protofilament number and the site the dimer occupies on that protofilament respectively. The protofilaments are indexed in a counter-clockwise fashion around the MT helix such that the first and last protofilaments interface across the seam. The dimers on a protofilament are indexed from the plus- to the minus-end such that the dimer closest to the plus-end of the MT is numbered $D_{i,1}$ (part d of figure on page 81). We call the MH with which it binds to the MT as $B_{i,j}$, the unbound-MH as $U_{i,j}$ and the neck $N_{i,j}$.

We considered three types of Ncd neighbors along the MT lattice: 1) longitudinal, along the same protofilament:$D_{i,j}$-$D_{i,j+1}$, 2) lateral, across adjacent protofilaments:$D_{i,j}$-$D_{i+1,j}$ 3) seam, across adjacent protofilaments separated by a seam: $D_{13,j}$-$D_{1,j+2}$ and $D_{13,j+1}$-$D_{1,j+2}$. By translating the Ncd-tubulin complex to superpose with the tubulin-dimers along the 13 protofilament MT, (Fig. 19), we constructed the two- or three-neighbor Ncds (in the case of seam).

2. Ncd neighbors from a motor+MT cryo-EM map complexes

As tubulin dimers polymerize to form MT, interactions with neighboring tubulin dimers induce conformational changes [103]. The structure of the MT may hence be different from that constructed by translating and rotating tubulin-dimers as shown in Fig. 19. Further, MH-attachment is also believed to change the structure of MT [104]. Hence, the interacting regions between two neighboring motors maybe different from those recorded from motors on an MT lattice constructed by translating and rotating tubulin-dimers as described above.

To test this, we fit high-resolution motor crystal structures into cryo-electron microscopy (EM) maps densities of motor+MT complexes using SITUS [105]. Towards this, we first obtained the bound-MH density maps by subtracting the bare 13-protofilament MT EM map [103] from the monomer-decorated MT EM-map[106]. Likewise, we obtained the unbound-MH density maps by subtracting the monomer-decorated MT EM-maps from the dimer-decorated MT EM-maps [25] in AMPPNP conditions. We then cropped a small region that holds two lateral and longitudinal neighboring motors close to the MT surface in both the extracted bound & unbound-MH map densities. Finally, we docked the MH-region of the crystal 1CZ7 into the neighboring bound- & unbound-MH densities.

C_α-C_α distance across residues between the longitudinal neighboring unbound-MHs (part b of figure on page 82) or between the unbound-MH and the bound-MH of a lateral neighbor (part d of figure on page 82) remain the same whether measured from crystal-structures fitted into cryo-EM maps (parts a & c of figure on page 82) or from Ncd crystals that occupied neighboring sites on a MT constructed by translating the tubulin dimers(Fig. 20b,d). With the backbone C_α atom distances well preserved, the interacting regions that we obtained from motor crystal structures placed at

neighboring sites on an MT lattice are hence not affected by any possible changes in the MT structure either due to change in the tubulin-dimers or due to MH binding.

C. Simulation details

All MD simulations were carried out using GROMACS [82] with the charmm force field [107] at 300 K. Structures were prepared as follows: We built a solvation box around the two- or three dimers and filled it with water molecules. Ions were added to neutralize the system. The system was first energy minimized by 1000 steps of adopted basis Newton-Raphson methods. Then harmonic constraints with a force constant of 2.3 kcal/(mol·Å^2) were applied to the backbone atoms and the system was heated to 300 K with a rate of 5 K per 0.5 ps and equilibrated for 200 ps. During equilibration, velocities of atoms were rescaled if the simulation temperature deviated from 300 K by more than ±5 K. We finally ran the molecular dynamics simulations by harmonically constraining the MT-interacting regions in the bound-MH ($L7$, $L11$ and $\alpha 4$) again with a force constant of 2.3 kcal/(mol·Å^2). The integration time step used in this study was 2 fs.

D. Results

1. Longitudinal interactions

We considered different combinations of pre- & post-stroke positions among two dimers that occupy immediate neighboring sites ($\mathrm{D}_{i,j}$ & $\mathrm{D}_{i,j+1}$) along the same protofilament (P_i). From these configurations, we record the closest interacting regions across the two dimers. Across 2 ns molecular dynamics (MD) simulations of these combinations across the two dimers, we traced three parameters: d_{inte}, the distance between the center-of-masses (COM) of two closest interacting regions across the dimers; d_{head},

Table IV. Closest regions and residues between longitudinal neighbors $D_{i,j}$ & $D_{i,j+1}$. $d_{\min}$ measures the distance between the O & H atoms in the respective side-chains of the closest residues across the two dimers.

Dimer states		Interacting Regions		Closest Neighbors		
$D_{i,j}$	$D_{i,j+1}$	$D_{i,j}$	$D_{i,j+1}$	$D_{i,j}$	$D_{i,j+1}$	$d_{\min}$ (nm)
pre	pre	$U_{i,j}$	$N_{i,j+1}$	L8	α0	2.3
				N510	V300	
pre	post	$U_{i,j}$	$U_{i,j+1}$	L11	L1	2.2
				E595	N365	
post	pre	$N_{i,j}$	$N_{i,j+1}$	α0	α0	0.2
				T298	T307	
post	post	$N_{i,j}$	$N_{i,j+1}$	L11	L1	2.6
				N598	N365	

the distance between the COM of the unbound-MHs; & d_{tip}, the distance between the two neck tips. Any attraction/repulsion between the two structures would reflect as a change in either/all of the three parameters. Table IV summarizes the closest regions and residues between the two neighbors.

When both $D_{i,j}$ & $D_{i,j+1}$ are in their pre- or post-stroke positions, the closest interacting regions in these dimers are separated by more than 2 nm (Table IV). The effect of interaction between the two dimers on each other is minimal as there was no significant changes in d_{inte}, d_{head} or d_{tip} through a 2-ns MD simulation (parts a &c of figure on page 83).

Interaction between the two dimers is also minimal when $D_{i,j}$ is in pre-stroke, while $D_{i,j+1}$ is in post-stroke. Here too, the closest interacting regions are separated by more than 2 nm and no significant change was recorded in d_{inte}, d_{head} or d_{tip} through a 2-ns MD simultion (part b of figure on page 83).

The plus-end positioned $D_{i,j}$ however, cannot execute its walking step before the minus-end positioned dimer. Steric repulsions prevent the neck of $D_{i,j}$ to rotate ahead

of $D_{i,j+1}$ (Fig. 21d). For the coiled-coil visible in the crystal structures (A296-R346), $D_{i,j}$'s neck can rotate upto 56° towards the minus-end (post-stroke position is achieved by $\sim 73°$ rotation), before it encounters the pre-stroke neck of $D_{i,j+1}$. Since the neck of ncd is considerably stiff (the elastic stiffness of the coiled-coil neck is 8.28×10^{-28} Nm^2 and 7.63×10^{-28} Nm^2 for two orthogonal bending directions), and that throughout its rotation, the neck makes continuous contacts with the bound-MH through a series of electrostatic and hydrogen-bonded interactions [100], it is unlikely that either $D_{i,j}$ or $D_{i,j+1}$'s necks will explore alternate configurations such as a transverse travel or bending to avoid this steric clash with the neighbor. As the neck extends directly into coiled-coil stalk, with longer stalks, the range of longitudinal rotations that $D_{i,j}$'s neck-stalk can explore with a pre-stroke $D_{i,j+1}$, reduces. Thus, for a chimera dimer with a coiled-coil from N236 [25], the neck-stalk of $D_{i,j}$ cannot rotate more than $\sim$16° before it encounters $D_{i,j+1}$. Since the rotation is guided diffusion, with the ATPase event, the $D_{i,j}$'s neck-stalk will continue to diffuse within the limited range of few degrees that $D_{i,j+1}$'s neck-stalk allows. Once, $D_{i,j+1}$'s neck-stalk starts executing its own walking step, $D_{i,j}$'s neck-stalk will then start to progressively travel forward by a series of interactions with the MH. The further $D_{i,j+1}$'s neck-stalk rotates towards the minus-end, the greater the range of rotation that neck-stalk of $D_{i,j}$ can explore without hindrance.

At the end of the neck rotation, after an ATPase event, the motor likely detaches from the MT, triggering the recovery stroke where due to the swivel action of the newly freed MH, the neck returns to the pre-stroke position [100]. When $D_{i,j+1}$ and $D_{i,j}$'s neck-stalks reach their post-stroke positions in succession (that is $D_{i,j}$'s neck rotates after $D_{i,j+1}$), $D_{i,j+1}$'s recovery is regulated by $D_{i,j}$. Here too, steric hindrances from the post-stroke neck of $D_{i,j}$ limit the range of $D_{i,j+1}$'s neck-stalk rotation to pre-stroke. In this case, $D_{i,j}$ can execute its reverse (rotation to pre-stroke) neck-

stalk motion with $D_{i,j+1}$ still in its post-stroke, while $D_{i,j+1}$'s neck-stalk can travel to pre-stroke only with or after $D_{i,j}$ neck-stalk's reverse travel. Thus, regulation of the forward motion of $D_{i,j}$'s neck-stalk by $D_{i,j+1}$ and the reverse motion of $D_{i,j+1}$'s neck-stalk by $D_{i,j}$ leads to a synchrony between the two longitudinal neighbors.

2. Lateral interactions

a. Neighbors across adjacent protofilaments (P_i & P_{i+1})

As we travel counter-clockwise along the left-handed helical axis of a microtubule, when two ncd dimers occupy neighboring binding sites across adjacent protofilaments (P_i & P_{i+1}), strong interactions are seen between the unbound- and the MT-bound MHs of the first and second dimers ($U_{i,j}$ and $B_{i+1,j}$) respectively. Table V summarizes the closest interactiong regions and residues across different combinations of the pre- & post-stroke lateral dimers.

When both $D_{i,j}$ and $D_{i+1,j}$ are in their pre-stroke positions, $U_{i,j}$ is in close contact with $B_{i+1,j}$ (Table V). A contact map between the two MHs reveal that the closest interacting regions are the surface loops L1, L2 in $U_{i,j}$ and the loops L1,L5 & L9 that form the nucleotide binding pocket (NBP) in $B_{i+1,j}$. L2 interactions with the NBP are well preserved over a 3 ns MD simulation (part a of figure on page 84). Since the rotation of the neck is triggered by an ATPase event, the blocking of NBP in $B_{i+1,j}$ by $U_{i,j}$, impedes the mechano-chemical cycle of $D_{i+1,j}$. Thus $D_{i+1,j}$ cannot execute its walking step while $D_{i,j}$ is in pre-stroke. Further, the strong interactions with the NBP in $B_{i+1,j}$ is likely to offer resistance (probably in the form of an energy barrier) to the diffusive travel of the neck in $D_{i,j}$. With the walking steps in both the dimers strongly impeded by their interactions, it hence becomes unfavorable for two Ncds to occupy lateral neighboring binding sites on an MT lattice when both of them are at

Table V. Closest regions and residues between lateral neighbors $D_{i,j}$ & $D_{i+1,j}$. $d_{\min}$ measures the distance between the O & H atoms in the respective side-chains of the closest residues across the two dimers.

Dimer states		Interacting Regions		Closest Neighbors		
$D_{i,j}$	$D_{i+1,j}$	$D_{i,j}$	$D_{i+1,j}$	$D_{i,j}$	$D_{i+1,j}$	d_{inte} (nm)
pre	pre/post	$U_{i,j}$	$B_{i+1,j}$	L2	L1	
				Q386	E360	0.63
				S389	E360	0.79
				K390	E360	0.57
				K390	E363	1.3
				L2	L4	
				I380	P448	0.8
				L2	L5	
				Q386	E449	1.1
				L2	α3	
				Q381	H533	0.47
post	pre/post	$U_{i,j}$	$B_{i+1,j}$	L12	L5	
				Q617	E449	1.3
				L12	L9	
				Q617	E560	1.8
post	post	$U_{i,j}$	$N_{i+1,j}$	L7	α0	
				D499	Q303	2.2

the beginning of their walking cycle.

However, when $B_{i,j}$ has rotated by nearly 20° around its relay-helix $\alpha 4$ after an ATPase event, while the neck $N_{i,j}$ is still in pre-stroke, interactions between $U_{i,j}$ & $B_{i+1,j}$ weaken (part a of figure on page 84). Here, the closest interacting residues in L2 of $U_{i,j}$ & L5 of & $B_{i+1,j}$ are separated by nearly 15 Å, thereby allowing mechanochemical cycles to proceed in both the dimers.

Thus, a post-stroke $D_{i+1,j}$, with a pre-stroke $N_{i,j}$ (Fig. 22) can only be possible when the neck rotation in $D_{i+1,j}$ happens before $D_{i,j}$ binds to MT or after $B_{i,j}$ has rotated to its post-stroke configuration due an ATPase event.

When $D_{i,j}$ is in post-stroke, $U_{i,j}$ moves away from blocking the NBP in $B_{i+1,j}$. Here, the interacting regions are $\alpha 4$-L12 in $U_{i,j}$ and L9-$\alpha 3$ in $U_{i+1,j}$. A 3 ns MD simulation with this post-stroke $U_{i,j}$ and a pre-stroke $B_{i+1,j}$ resulted in a decrease of d_{inte} by about 0.5 nm, indicating an attractive interaction between the two MHs. When $D_{i+1,j}$ is also in post-stroke, apart from the weak attractive interactions between $U_{i,j}$ & $B_{i,j}$, $N_{i+1,j}$ also interacts weakly with $U_{i,j}$ (Table V). Attractive interactions between the two dimers in both of their end-states imply that lateral neigbors will execute their walking step asynchronously. $D_{i,j}$ binding to the MT after $D_{i+1,j}$ finishes its walking step and its neck in post-stroke will ensure least possible impedence to the motility in both the dimers.

b. Neighbors across a seam (P_{13} & P_1)

Due to the 3 start-helix and the associated stagger, interactions between dimers across a seam are different from those between lateral neighbors elsewhere. Dimers across protofilaments without a seam separating them, interact with only the lateral neighbor and not with those at sites preceding or after the lateral neighbor (for instance, $D_{i,j}$ interacts only with $D_{i+1,j}$ and not $D_{i+1,j+1}$ or $D_{i+1,j-1}$). However, across the seam,

each dimer $D_{1,j+2}$ interacts with two lateral neighbors ($D_{13,j}$ and $D_{13,j+1}$) (part a of figure on page 85). Table VI summarizes the closest interactiong regions and residues across different combinations of these pre- & post-stroke seam dimers. Since we have already established how two longitudinal neighbors execute their walking step in synchrony, discussed below is how the motility of these two longitudinal dimers and the lateral neighbor across the seam are coordinated.

$D_{13,j}$-$D_{1,j+2}$: When both the dimers are in their pre-stroke, $U_{13,j}$ weakly interacts through L8 with L2 in $B_{1,j+2}$ (Table VI, Fig 23b). When $D_{13,j}$ is in post-stroke while $D_{1,j+2}$ is in pre-stroke, $U_{13,j}$ interacts with $N_{1,j+2}$. This interaction is likely to impede the recovery stroke of $D_{13,j}$ and the forward travel of $N_{1,j+2}$. When both the dimers are in their post-stroke they lose all interactions. Thus, to save motility in both the dimers, it is likely that $D_{1,j+2}$ binds to MT and travels to post-stroke ahead of $D_{13,j}$ binding to the MT. $D_{1,j+2}$ & $D_{13,j}$ execute their walking steps in succession.

$D_{13,j+1}$-$D_{1,j+2}$: When both the dimers are in their pre-stroke there is little interaction between them. Post-stroke $N_{1,j+2}$ interacts strongly with a pre-stroke $U_{13,j+1}$ (Table VI, Fig 23c) thereby impeding the recovery stroke of $D_{1,j+2}$ and the forward travel of $D_{13,j+1}$. Post-stroke $U_{13,j+1}$ blocks the NBP of $B_{1,j+2}$ through strong interactions between their respective L2 & L5 loops. Further, post-stroke $N_{1,j+2}$ also interacts with post-stroke $U_{13,j+1}$, leading to additional constraints in the motility cycles of both the dimers. Since through these different combinations of pre- & post-stroke positions motility in both the dimers are impeded, it is unlikely that $D_{13,j+1}$ and $D_{1,j+2}$ will attach to the MT when the other is present.

Thus across the seam, when the two longitudinal neighbors $D_{13,j}$ & $D_{13,j+1}$ bind and execute their walking step in synchrony, $D_{1,j+2}$ will not attach to the MT. If it does, there is bound to be loss in motility in all three dimers.

Table VI. Closest regions and residues between lateral neighbors across seam: $D_{13,j}$ & $D_{1,j+2}$; $D_{13+1,j}$ & $D_{1,j+2}$. $d_{\min}$ measures the distance between the O & H atoms in the respective side-chains of the closest residues across the two dimers.

Dimer states		Interacting Regions		Closest Neighbors		
$D_{13,j}$	$D_{1,j+2}$	$D_{13,j}$	$D_{1,j+2}$	$D_{13,j}$	$D_{1,j+2}$	$d_{\min}$ (nm)
pre	pre	$U_{13,j}$	$B_{1,j+2}$	L2	L8	
				Q386	E520	0.78
pre	post	$U_{13,j}$	$B_{1,j+2}$	L2	α3	
				K390	D524	0.93
				Q386	T521	0.58
post	pre	$U_{13,j}$	$N_{1,j+2}$	L11	α0	
				T594	Q305	1.0
post	post	$U_{13,j}$	$B_{1,j+2}$	α4	L8	
				K618	Q516	2.1
$D_{13,j+1}$	$D_{1,j+2}$	$D_{13,j+1}$	$D_{1,j+2}$	$D_{13,j+1}$	$D_{1,j+2}$	
pre	pre	$U_{13,j+1}$	$B_{1,j+2}$	L1	β1	
				T369	E360	1.75
pre	post	$U_{13,j+1}$	$N_{1,j+2}$	L1	α0	
				E360	R312	1.42
				L9	α0	
				T544	Q305	0.97
post	pre	$U_{13,j+1}$	$B_{1,j+2}$	L2	L5	
				K390	E449	0.38
post	post	$U_{13,j+1}$	$N_{1,j+2}$	L11	α0	
				T594	E308	0.33
		$U_{13,j+1}$	$B_{1,j+2}$	L2	L5	
				K390	E449	0.85

E. Discussion

1. Longitudinal decoration

Our structural analysis reveals that steric hindrances from a pre-stroke neck-stalk of a minus-end sided neighbor ($D_{i,j+1}$) limits the neck-stalk rotation of a plus-end sided dimer ($D_{i,j}$) thereby regulating its walking step (Fig. 21). The synchrony between $D_{i,j+1}$ & $D_{i,j}$ extends across $D_{i,j+2}$ & $D_{i,j+1}$, $D_{i,j+3}$ & $D_{i,j+2}$ and so on. Hence, when the protofilament P_i is completely occupied by dimers, all of them execute their walking step together.

When a motor tries to attach to an MT site where the neighboring site is occupied, steric hindrance with a pre-stroke neck of a minus-ended longitudinal neighbor may prevent it from attaching to the MT at that site. Steric hindrances with a post-stroke neck-stalk of a plus-ended neighbor may also prevent MT attachment. The motor may then explore an alternative site that has a pre-stroke plus-ended neighbor and/or a post-stroke minus-ended neighbor. In either of the cases, the stalk rotation of this newly attached motor will eventually be influenced by the pre-/post-stroke positions of its neighbors thereby leading to cooperativity among this group. Over time, when a group of motors begin to decorate a filament and most dimers are in their pre-stroke, the steric hindrances with the pre-stroke neck-stalks coupled with the regulation of the neck-stalk rotation to post-stroke by a minus-ended neighbor, will make the minus-ended MT sites more favorable, driving a minus-end sided accumulation by a group of motors.

2. Lateral decoration

Strong attractive interactions between the surface loop L2 in unbound-MH ($U_{i,j}$) and the NBP in the bound-MH ($U_{i+1,j}$) of two lateral neighbors in their pre-stroke explain

the attractive energy between two kinesins on an MT [35, 36]. Such an attraction however affects the motility cycle in both the motors. Our structural analysis reveals that if $D_{i,j}$ attaches to its MT site ahead of $D_{i+1,j}$, steric hindrance with the $U_{i,j}$ prevents $D_{i+1,j}$ from attaching to its site. On the other hand, when $D_{i+1,j}$ occupies its MT site first, $D_{i,j}$ can bind to its own MT site later. Although this clockwise lateral decoration along the super-helical axis of MT is structurally possible, it will lead to loss in motility cycles across all lateral neighbors and hence unlikely to be adopted by a group of motors. Since the interaction between the $U_{i,j}$ and $B_{i+1,j}$ is minimal when $D_{i,j}$ is in its post-stroke, it is more likely that $D_{i+1,j}$ will attach to the MT after either $B_{i,j}$ or $N_{i,j}$ reaches post-stroke. Thus anti-clockwise lateral decoration along the axis of MT is likely separated in time, where every new motor ($D_{i+1,j}$) attaches to its MT site only after an ATPase event in its lateral neighbor's bound-head.

3. Lateral decoration across the seam

Among all the possible configurations of the three neighbors across the seam ($D_{1,j+2}$, $D_{13,j}$ & $D_{13,j+1}$), attractive interactions exist that would impede motility in all the three motors. To avoid loss in motility, at any point of time, all the three dimers cannot be bound to the MT. When $D_{13,j}$ & $D_{13,j+1}$ are attached (and their longitudinal interactions drive them to execute their walking step together), $D_{1,j+2}$ cannot attach to its MT site. Because of the interactions between the $U_{13,j+1}$ and the neck of $D_{1,j+2}$ in all of their pre- & post-stroke combinations, $D_{1,j+2}$ cannot attach to the MT when $D_{13,j+1}$ is bound to the MT. Similarly, $D_{1,j+2}$ cannot attach to the MT when $D_{13,j}$ is already bound to the MT. However, if $D_{1,j+2}$ attaches to the MT first, $D_{13,j}$ can attach to the MT after $D_{1,j+2}$ in its post-stroke. It maybe noted that because of the interactions between $U_{13,j}$ and $B_{1,j+2}$, $D_{1,j+2}$ cannot complete its recovery stroke till $D_{13,j}$'s neck travels to post-stroke. Ideally, a motor would hence avoid binding to the

MT at a site that interfaces with the seam, when the lateral neighbor sites are already occupied.

Rules for MT decoration: To summarize our analysis, we propose the following rules/conditions that will govern a motor binding to a particular site ($D_{1,j}$) where immediate neighbors exist, such that its motility cycle is not affected upon attaching to the MT at that site.

- $D_{i,j-1}$ in pre-stroke: $D_{i,j}$ binds to MT and the neck rotations in both the motors synchronized.
- $D_{i,j-1}$ in post-stroke: $D_{i,j}$ does not bind.
- $D_{i,j+1}$ in pre-stroke: $D_{i,j}$ does not bind.
- $D_{i,j+1}$'s neck is traveling to or is already in post-stroke: $D_{i,j}$ binds to MT and executes its post-stroke travel. As the neck of $D_{i,j}$ rotates to post-stroke, $D_{i,j+1}$ will synchronize its recovery stroke with $D_{i,j}$.

When $i \neq 1$,

- $D_{i-1,j}$ in pre-stroke: $D_{i,j}$ does not bind (steric repulsion due to neck-stalk).
- $D_{i-1,j}$ in post-stroke: $D_{i,j}$ binds to MT and executes its walking step.
- $D_{i+1,j}$ in pre-/post-stroke: $D_{i,j}$ does not bind (if it does loss in motility in both the dimers).

When $i = 1$, lateral interactions with neighbors across the seam (on P_{13}) start only from $j \geq 2$. For $j = 2$ and irrespective of whether $D_{13,1}$ is in pre-/post-stroke, interactions with the $U_{13,1}$ prevents $D_{1,2}$ to bind as it leads to loss in motility in both dimers. For $j > 2$:

- $D_{13,j-2}$ in pre-/post-stroke: $D_{1,j}$ does not bind (if it does, loss in motility in both dimers).

- $D_{13,j-1}$ in pre-/post-stroke: $D_{1,j}$ does not bind (if it does, loss in motility in both dimers).

When $i = 13$,

- $D_{1,j+2}$ in pre-stroke: $D_{13,j}$ does not bind (if it does, loss in motility in both dimers).

- $D_{1,j+2}$ in post-stroke: $D_{13,j}$ may bind, but due to interactions between $U_{13,j}$ and $B_{i,j+2}$, loss in motility in $D_{13,j}$ (no such loss in motility in $D_{1,j+2}$).

Across all the lateral neighbors, we note that the unbound-MH mediates interactions between the two dimers. Thus, although the unbound-MH may have a minimal role in the rotation of the neck of a single Ncd [25, 100], it plays a critical role in regulating cooperativity and decoration of an MT filament by a group of motors.

F. Conclusion

Using structural analysis we noted that steric hindrances between the neck-stalks of longitudinal neighbors drive synchrony among a group of motors on a single protofilament. Control by minus-end sided neighbors on the motility of plus-end sided dimers drive a MT minus-end accumulation by a group of motors. To prevent loss in motility, Ncds would attach to the MT after it's lateral neighbor's MH has undergone ATPase event and proceeded to post-stroke configuration. Thus, unbound-MH regulates the spatial and temporal decoration of the MT by a group of motors. Information about the regions within an Ncd dimer that are involved in interactions with a neighbor maybe useful for engineering motors to decorate a filament in a particular fashion.

Additionally, continuous time monte-carlo simulations incorporating the rules described above will elucidate MT decoration and motility characteristics by a group of motors. MD simulations with coarse-grained Go-like models [108] of an Ncd dimers on an MT lattice are likely to capture the effect of a neighbor on the diffusive travel of the neck thereby corroborating our structural analysis findings. Elucidating the physical basis of cooperativity and interactions between neighbors will be crucial for understanding the collective behavior of cooperative motors on a filament.

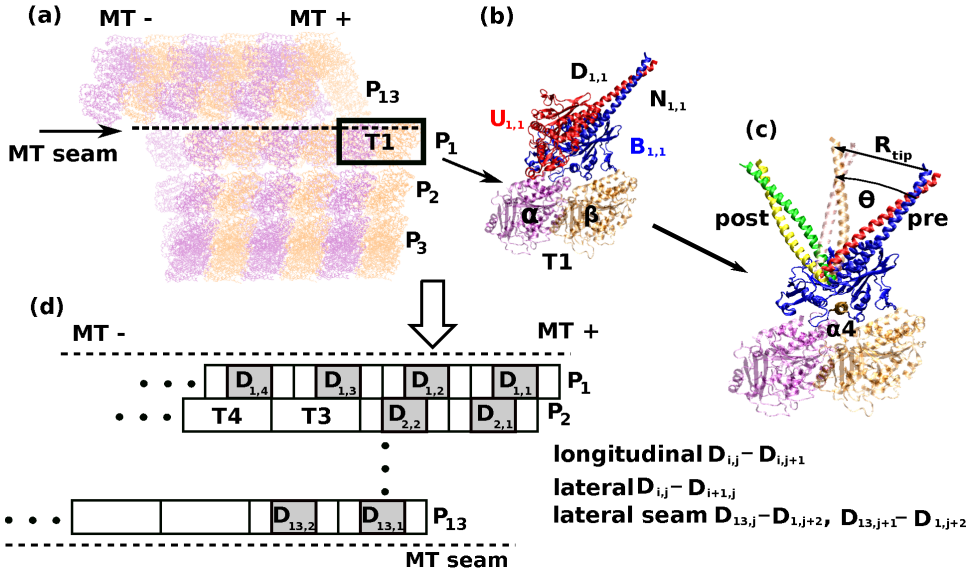

Fig. 19. (a) 13 protofilament (P_1, P_2,...,P_{13}) microtubule built from the α-β tubulin dimer (PDB:1JFF). (b) Ncd dimer interacts with the α-β tubulin dimer (T1) through one of its MH (bound MH, $B_{1,1}$), while the second MH (unbound MH, $U_{1,1}$) travels passively with the neck ($N_{1,1}$). Orientation of the bound MH, $B_{1,1}$ on T1 dimer is obtained by superposing $B_{1,1}$ onto the kinesin-MH 1MKJ in the PDB 2P4N. (c) Neck rotates from the plus-end pointing pre-stroke position to the minus-end pointing post-stroke position through guided diffusion where it makes series of intermediate contacts with the bound-MH. Neck travel is possibly triggered by an ATPase event that leads to a see-saw motion of the bound-MH mediated by the relay helix $\alpha 4$ (colored in ochre). $R_{\rm tip}$, the distance of the tip of the neck (the S297 C_α atom) from its pre-stroke position; and θ, the longitudinal angle traversed by the neck from its pre-stroke position are used to measure the neck travel. (d) When Ncds thus decorate the MT filament, there are two possible neighbors for each Ncd dimer (along the longitudinal axis, and off-axis or lateral). Lateral interactions between Ncds at the seam are different from the interactions between two Ncds occupying neighboring protofilaments elsewhere in the MT.

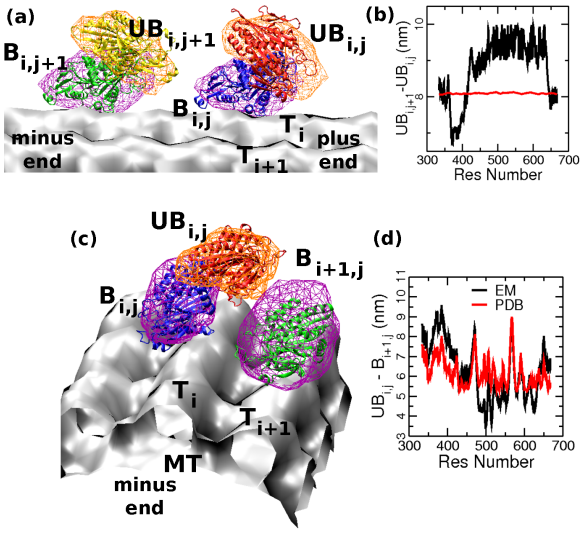

Fig. 20. Longitudinal ($D_{i,j}$-$D_{i,j+1}$) (a,b) and lateral ($D_{i,j}$-$D_{i+1,j}$) neighbors (c,d) from fitting MH from crystal 1CZ7 into cryo-EM maps of Ncd with AMPPNP bound to MT using SITUS. C_α-C_α distances between unbound-MH of longitudinal neighbors (c) and the unbound-MH and bound-MH of lateral neighbors (d) are similar to those recorded between neighbors on an MT lattice constructed by translating and rotating tubulin-dimers 1JFF.

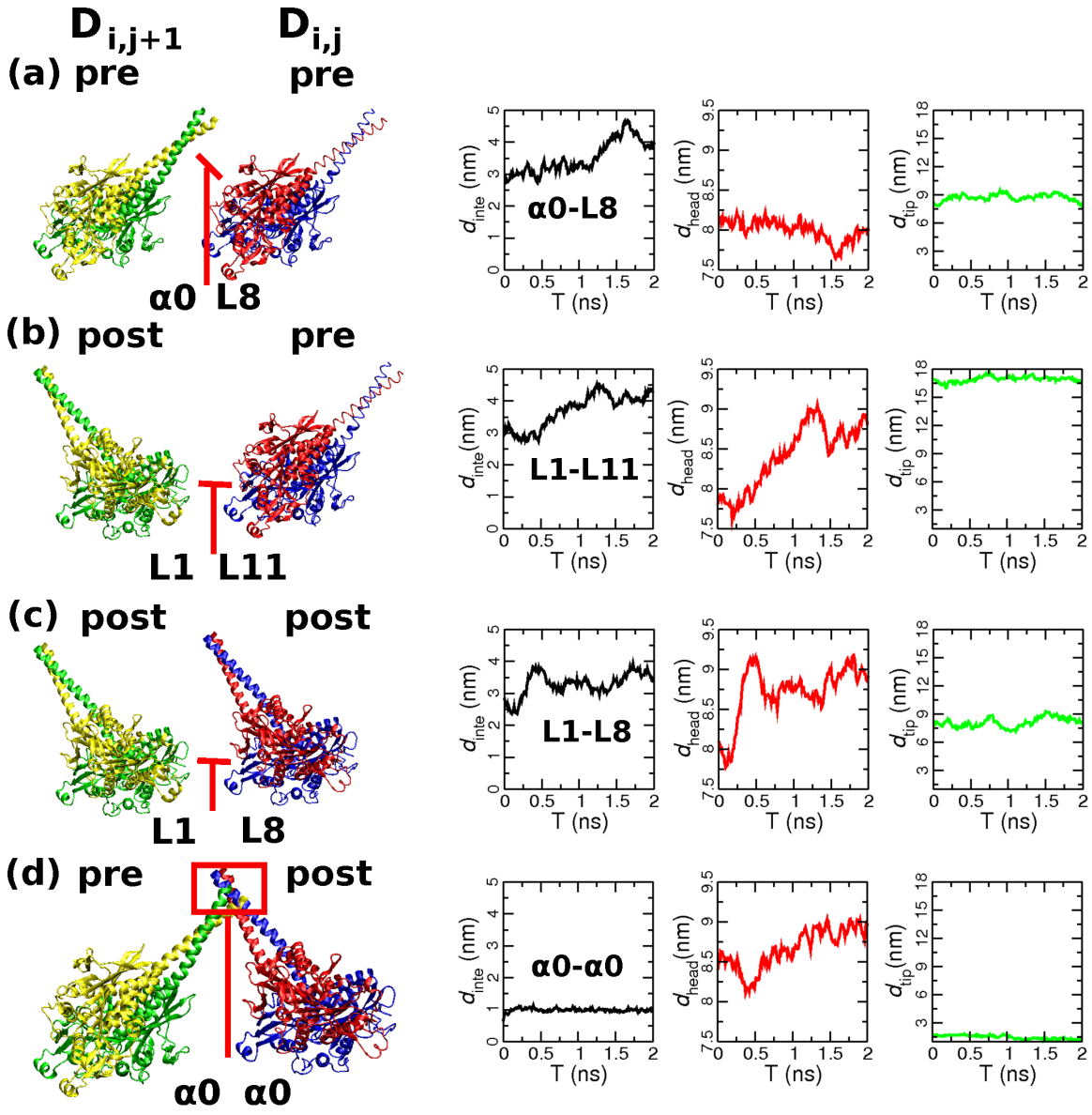

Fig. 21. Interactions between longitudinal neighbors. (a-c) Minimal interactions between the neighbors as observed by little or no change in d_{inte}, d_{head} or d_{tip} (refer text for definitions). (d) Steric hindrance prevents this conformation, thereby synchronizing the neck travel across the two dimers.

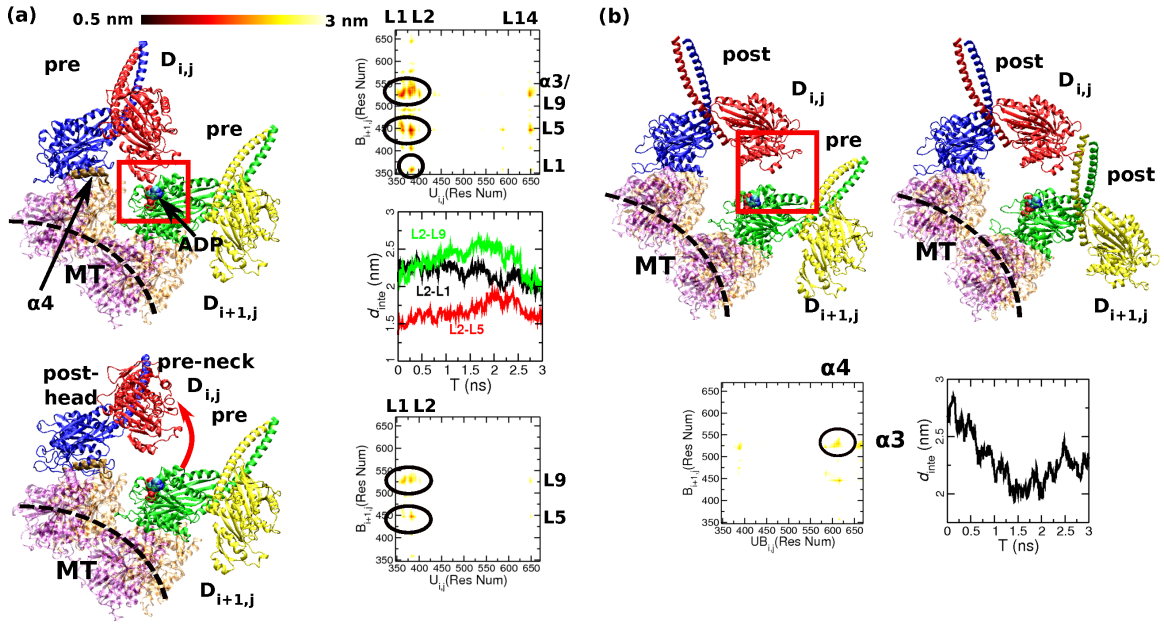

Fig. 22. Interactions between lateral neighbors $D_{i,j}$ & $D_{i+1,j}$. Residues from the two dimers are considered to form a potential contact when their C_α atoms are lesser than 3 nm away. (a) When both the dimers are in their pre-stroke, $U_{i,j}$ blocks the NBP in $B_{i+1,j}$ thereby regulating $D_{i+1,j}$'s mechanochemical cycle. Contact map and d_{inte} from a 3-ns MD simulation reveal a strong attractive interaction between the surface loop L1 of $U_{i,j}$ and the NBP of $B_{i+1,j}$. These contacts weaken when an ATPase event triggers a nearly 20 ° rotation of $B_{i,j}$ around its $\alpha 4$ relay helix, and $U_{i+1,j}$ moves away from $B_{i+1,j}$. (b) When $D_{i,j}$ is in post-stroke, the distance between $U_{i,j}$ and $B_{i+1,j}$ further increases. The interaction between the two dimers (closest interacting regions are $\alpha 4$ in $U_{i,j}$ and $\alpha 3$ in $B_{i+1,j}$) is minimal as seen from the contact map and d_{inte} through a 3-ns MD simulation.

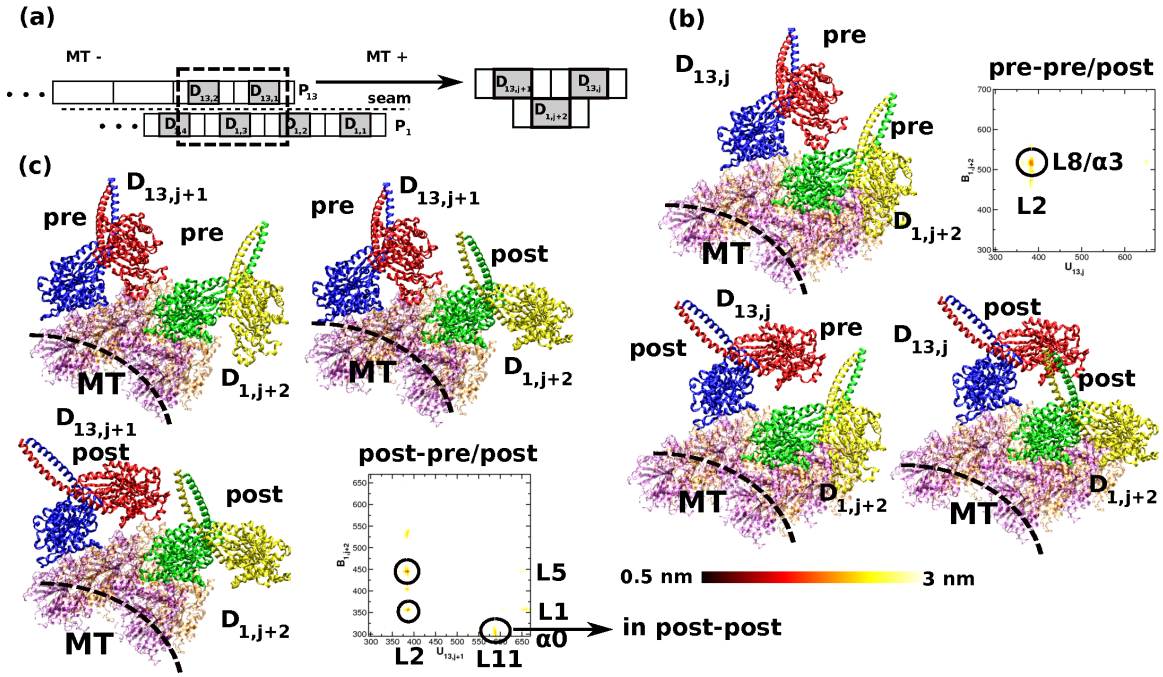

Fig. 23. Interactions between lateral neighbors across seam. (a) Across the seam, there are two types of neighbors: $D_{13,j}$ & $D_{1,j+2}$; $D_{13,j+1}$ & $D_{1,j+2}$. (b) When both $D_{13,j}$ & $D_{1,j+2}$ are in their pre-stroke, L2 in $U_{13,j}$ interacts with L8 in $B_{1,j+2}$. While, post-stroke $U_{13,j}$ does not interact with $B_{1,j+2}$, it forms contacts via L11 with the pre-stroke neck of $D_{1,j+2}$ (refer Table 2). When both $D_{13,j}$ & $D_{1,j+2}$ are in post-stroke, no interactions are observed. (c) When both $D_{13,j+1}$ and $D_{1,j+2}$ are in pre-stroke, they do not interact. L2 of post-stroke $U_{13,j+1}$ interacts strongly with L5 of $B_{1,j+2}$. When $D_{1,j+2}$ is also in post-stroke, $N_{1,j+2}$ also interacts with $U_{13,j+1}$ through L11. Contact map distances follow the same criteria as Fig. 22.

CHAPTER V

CONCLUSION

Normal mode analysis of coiled-coils revealed that weak non-bonded forces induce a buckling instability which we characterized using a critical buckling length (l_c). Since, these non-bonded forces are not screened in physiological conditions, such an instability is likely to be present in all biofilaments. For coiled-coils, l_c was lesser than the persistence length and hence it modulates the filament conformational ensemble. Notably, coiled-coils with mechanical roles such as tropomyosin or the neck-stalks of kinesins have lengths lesser than l_c.

Using local fluctuation analysis, we found that tropomyosin has regions of varying flexibilities. Our results showed that while stiffnesses of α-helices are relatively insensitive to amino-acid composition, in α-helical coiled-coils, hydrophobic core residues involved in the knob-into-hole packing significantly modulate their elasticity. Regional variations in flexibilities due to such breaks in the hydrophobic core of the coiled-coil are tailored for the function of tropomyosin.

A future direction for this work involves studying the mechanics and energetics of tropomyosin's interactions with the F-actin. Since EM-maps of tropomyosin in all of its three known states over the F-actin surface are now available [109], it is possible to fit high-resolution crystal structures into the EM-map densities and determine the physical basis of tropomyosin's transition across these states. As point mutations in the actin-binding contacts of tropomyosin are associated with various abnormalities and disease conditions [8, 9], atomistic simulations of tropomyosin with the F-actin filament across each of the three known states are likely to offer insights into the role of such contacts in tropomyosin's function on F-actin.

Also, the local flexibility map analysis we developed is not specific to coiled-coils

or a particular length-scale. It maybe applied to study the flexibilities of large (such as f-actin or microtubules) or smaller (DNA fragments) filaments, thereby providing useful insights into their mechanical function.

In Kinesin-14 Ncd, using molecular dynamics simulations and structural analysis, we found that the α-helical coiled-coil neck motion was a guided diffusion along a mostly longitudinal path through a series of intermediate contacts with the MH. Energetics of the forward and reverse motion revealed a hysteresis that is due to the mechanical compliance of the protein. We note that such a hysteresis in forward and reverse motion is useful for the directed motility of the ncd motor. More generally, elucidating hysteresis and the physical basis of the motility mechanism on an atomistic scale will be important for understanding other translocating motors such as myosins as well.

A limitation of the current work is the lack of understanding the role of the C-terminal tail in the walking step of Ncd. Studies have long hypothesized that it may play a dynamical role similar to the cover-neck bundle formation in Kinesin-1 [22]. However, possibly because of their flexible nature they are invisible in crystal structures of Ncd published so far. In the crystal 3L1C the C-tail is visible up to K674 and it points to the MT plus end, analogous to the neck linker of Kinesin-1 in the MH-docked state. Although we did run preliminary simulations of an MT-bound Ncd with the C-tail and E-hook domains, more all-atom and/or coarse-grained simulations are needed to determine the energetics and the dynamics of the C-tail interactions with the E-hooks of the MT and possibly the pre-stroke neck of Ncd. Understanding the role of the C-tail in neck motion will hence complete the atomistic picture of the walking step of the Ncd motor.

Apart from rotating towards the minus-end of MT in the walking step, we found that α-helical coiled-coil neck-stalks of Ncds are seen to regulate cooperativity among

a group of motors that decorate a single protofilament of the MT. Our results also revealed that the unbound-MH whose role was minimal in the walking step of a single Ncd is useful in regulating MT decoration by a group of motors. Although our structural analysis hypothesize the possible effect of attractive interactions between neighbors on the motility cycle, additional all-atom or coarse grained simulations with multiple dimers are needed to understand the influence of such interactions between neighbors on the cooperative functioning of the group.

REFERENCES

[1] S. Perry, "Vertebrate tropomyosin: Distribution, properties and function," *J. Mus. Res. Cell Motil.*, vol. 22, no. 1, pp. 5–49, 2001.

[2] P. Naumanen, P. Lappalainen, and P. Hotulainen, "Mechanisms of actin stress fibre assembly," *J. Microscopy*, vol. 231, no. 3, pp. 446–454, 2008.

[3] M. Greenberg, C. Wang, W. Lehman, and J. Moore, "Modulation of actin mechanics by caldesmon and tropomyosin," *Cell Motil Cytoskeleton*, vol. 65, no. 2, pp. 156–64, 2008.

[4] J. Brown and C. Cohen, "Regulation of muscle contraction by tropomyosin and troponin: How structure illuminates function," *Adv. Protein Chem.*, vol. 71, pp. 121–59, 2005.

[5] A. McLachlan and M. Stewart, "The 14-fold periodicity in alpha-tropomyosin and the interaction with actin." *J. Mol. Biol.*, vol. 103, no. 2, pp. 271–98, 1976.

[6] A. Singh and S. E. Hitchcock-DeGregori, "Tropomyosin's periods are quasi-equivalent for actin binding but have specific regulatory functions," *Biochemistry*, vol. 46, no. 51, pp. 14 917–14 927, 2007.

[7] G. Phillips Jr., J. Fillers, and C. Cohen, "Tropomyosin crystal structure and muscle regulation." *J. Mol. Biol.*, vol. 192, no. 1, pp. 111–31, 1986.

[8] R. Gaffin, K. Gokulan, J. Sacchettini, T. Hewett, R. Klevitsky, J. Robbins, and M. Muthuchamy, "Charged residue changes in the carboxy-terminus of α-tropomyosin alter mouse cardiac muscle contractility," *The Journal of Physiology*, vol. 556, no. 2, pp. 531–543, 2004.

[9] T. M. Olson, N. Y. Kishimoto, F. G. Whitby, and V. V. Michels, "Mutations that alter the surface charge of alpha-tropomyosin are associated with dilated cardiomyopathy," *Journal of Molecular and Cellular Cardiology*, vol. 33, no. 4, pp. 723–732, 2001.

[10] J. Brown, Z. Zhou, L. Reshetnikova, H. Robinson, R. Yammani, L. Tobacman, and C. Cohen, "Structure of the mid-region of tropomyosin: Bending and binding sites for actin," *Proc. Natl. Acad. Sci. USA*, vol. 102, no. 52, pp. 18 878–18 883, 2005.

[11] G. Phillips Jr. and S. Chacko, "Mechanical Properties of tropomyosin and implications for muscle regulation," *Biopolymers*, vol. 38, pp. 89–95, 1996.

[12] S. K. Lakkaraju and W. Hwang, "Critical buckling length versus persistence length: What governs a biofilament conformation?" *Phys. Rev. Lett.*, vol. 102, no. 11, p. 118102, 2009.

[13] S. Endow, S. Henikoff, and L. Soler-Niedziela, "Mediation of meiotic and early mitotic chromosome segregation in Drosophila by a protein related to kinesin," *Nature*, vol. 345, no. 1, pp. 81–83.

[14] S. Endow, "Meiotic chromosome distribution in Drosophila oocytes: Roles of two kinesin-related proteins," *Chromosoma*, vol. 102, no. 1, pp. 1–8, 1992.

[15] M. deCastro, R. Fondecave, L. Clarke, C. Schmidt, and R. Stewart, "Working strokes by single molecules of the kinesin-related microtubule motor ncd." *Nat. Cell Biol.*, vol. 2, no. 10, pp. 724–729, 2000.

[16] W. Hwang and M. J. Lang, "Mechanical design of translocating motor proteins," *Cell Biochem. Biophys.*, vol. 54, no. 1, pp. 11–22, 2009.

[17] R. H. Wade and F. Kozielski, "Structural links to kinesin directionality and movement," *Nat. Struct. Biol.*, vol. 7, pp. 456–460, 2000.

[18] U. Henningsen and M. Schliwa, "Reversal in the direction of movement of a molecular motor," *Nature*, vol. 389, no. 6646, pp. 93–96, 1997.

[19] R. B. Case, D. W. Pierce, N. Hom-Booher, C. L. Hart, and R. D. Vale, "The directional preference of kinesin motors is specified by an element outside of the motor catalytic domain," *Cell*, vol. 90, no. 5, pp. 959–966, 1997.

[20] S. A. Endow and K. W. Waligora, "Determinants of kinesin motor polarity," *Science*, vol. 281, no. 5380, pp. 1200–1202, 1998.

[21] S. Rice, A. W. Lin, D. Safer, C. L. Hart, N. Naberk, B. O. Carragher, S. M. Cain, E. Pechatnikova, E. M. Wilson-Kubalek, M. Whittaker, E. Pate, R. Cooke, E. W. Taylor, R. A. Milligan, and R. D. Vale, "A structural change in the kinesin motor protein that drives motility," *Nature*, vol. 402, pp. 778–784, 1999.

[22] W. Hwang, M. J. Lang, and M. Karplus, "Force generation in kinesin hinges on cover-neck bundle formation," *Structure*, vol. 16, no. 1, pp. 62–71, 2008.

[23] A. S. Khalil, D. C. Appleyard, A. K. Labno, A. Georges, M. Karplus, A. M. Belcher, W. Hwang, and M. J. Lang, "Kinesin's cover-neck bundle folds forward to generate force," *Proc. Natl. Acad. Sci. USA*, vol. 105, pp. 19 247–19 252, 2008.

[24] M. Yun, C. E. Bronner, C. G. Park, S. S. Cha, H. W. Park, and S. A. Endow, "Rotation of the stalk/neck and one head in a new crystal structure of the kinesin motor protein, Ncd," *EMBO J.*, vol. 22, no. 20, pp. 5382–5389, 2003.

[25] N. F. Endres, C. Yoshioka, R. A. Milligan, and R. D. Vale, "A lever-arm rotation drives motility of the minus-end-directed kinesin Ncd," *Nature*, vol. 439, no.

7078, pp. 875–878, 2006.

[26] E. P. Sablin, R. B. Case, S. C. Dai, C. L. Hart, A. Ruby, R. D. Vale, and R. J. Fletterick, "Direction determination in the minus-end-directed kinesin motor ncd," *Nature*, vol. 395, no. 6704, pp. 813–816, 1998.

[27] S. A. Endow and H. Higuchi, "A mutant of the motor protein kinesin that moves in both directions on microtubules," *Nature*, vol. 406, no. 6798, pp. 913–916, 2000.

[28] E. Heuston, C. E. Bronner, F. J. Kull, and S. A. Endow, "A kinesin motor in a force-producing conformation," *BMC Struct. Biol.*, vol. 10, no. 1, pp. 19–31, 2010.

[29] M. A. Hallen, Z. Y. Liang, and S. A. Endow, "Two-state displacement by the kinesin-14 Ncd stalk," *Biophys. Chem.*, vol. 154, pp. 56–65, 2011.

[30] A. E. Butterfield, R. J. Stewart, C. F. Schmidt, and M. Skliar, "Bidirectional power stroke by ncd kinesin," *Biophys. J.*, vol. 99, no. 12, pp. 3905–3915, 2010.

[31] G. Fink, L. Hajdo, K. Skowronek, C. Reuther, A. Kasprzak, and S. Diez, "The mitotic kinesin-14 Ncd drives directional microtubule–microtubule sliding," *Nat. Cell Biol.*, vol. 11, no. 6, pp. 717–723, 2009.

[32] G. Goshima, F. Nedelec, and R. Vale, "Mechanisms for focusing mitotic spindle poles by minus end-directed motor proteins," *J. Cell Biol.*, vol. 171, no. 2, p. 229, 2005.

[33] M. Badoual, F. Julicher, and J. Prost, "Bidirectional cooperative motion of molecular motors," *Proc. Natl. Acad. Sci. USA*, vol. 99, no. 10, pp. 6696–6702, 2002.

[34] C. Sciambi, D. Komma, H. Skold, K. Hirose, and S. Endow, "A bidirectional kinesin motor in live Drosophila embryos," *Traffic*, vol. 6, no. 11, pp. 1036–1046, 2005.

[35] A. Vilfan, E. Frey, F. Schwabl, M. Thormahlen, Y. Song, and E. Mandelkow, "Dynamics and cooperativity of microtubule decoration by the motor protein kinesin1," *J. Mol. Biol.*, vol. 312, no. 5, pp. 1011–1026, 2001.

[36] H. Roos, O. Campàs, F. Montel, G. Woehlke, J. Spatz, P. Bassereau, and G. Cappello, "Dynamic kinesin-1 clustering on microtubules due to mutually attractive interactions," *Physical Biology*, vol. 5, pp. 046 004–046 014, 2008.

[37] J. Cope, S. Gilbert, I. Rayment, D. Mastronarde, and A. Hoenger, "Cryo-electron tomography of microtubule-kinesin motor complexes," *J. Struct. Biol.*, vol. 170, no. 2, pp. 257–265, 2010.

[38] F. Whitby and G. Phillips Jr, "Crystal structure of tropomyosin at 7 angstroms resolution," *PROTEINS: Structure, Function, and Genetics*, vol. 38, pp. 49–59, 2000.

[39] S. Choe and S. X. Sun, "The elasticity of alpha-helices," *J. Chem. Phys.*, vol. 122, no. 24, pp. 244 912–244 919, 2005.

[40] C. Wolgemuth and S. Sun, "Elasticity of α-Helical coiled coils," *Phys. Rev. Lett.*, vol. 97, no. 24, pp. 248 101–4, 2006.

[41] F. Crick, "The packing of α-helices: simple coiled-coils," *Acta Cryst.*, vol. 6, no. 8-9, pp. 689–697, 1953.

[42] S. Minakata, K. Maeda, N. Oda, K. Wakabayashi, Y. Nitanai, and Y. Maeda, "Two-crystal structures of tropomyosin C-terminal fragment 176-273: exposure

of the hydrophobic core to the solvent destabilizes the tropomyosin molecule," *Biophys. J.*, vol. 95, no. 2, pp. 710–719, 2008.

[43] L. Landau and E. Lifshitz, *Course of Theoretical Physics, Vol. 7: Theory of Elasticity*. Elsevier Science, Nauka, Moscow, 1987.

[44] A. Goriely and M. Tabor, "Nonlinear dynamics of filaments i. dynamical instabilities," *Physica D*, vol. 105, pp. 20–44, 1997.

[45] J. Park, B. Kahng, R. Kamm, and W. Hwang, "Atomistic simulation approach to a continuum description of self-assembled β-sheet filaments," *Biophys. J.*, vol. 90, no. 7, pp. 2510–2524, 2006.

[46] F. Reif, *Fundamentals of Statistical and Thermal Physics*. Tokyo, Japan: McGraw-Hill, 1965.

[47] G. Arfken and H. Weber, *Mathematical Methods for Physics*, 6th ed. Burlington, MA: Academic Press, 1997.

[48] I. Adamovic, S. Mijailovich, and M. Karplus, "The elastic properties of the structurally characterized myosin II S2 subdomain: A molecular dynamics and normal mode analysis," *Biophys. J.*, vol. 94, no. 10, pp. 3779–3789, 2008.

[49] B. Brooks, R. Bruccoleri, B. Olafson, D. States, S. Swaminathan, and M. Karplus, "CHARMM: A program for macromolecular energy, minimization, and dynamics calculations," *J. Comp. Chem.*, vol. 4, pp. 187–217, 1983.

[50] W. Humphrey, A. Dalke, and K. Schulten, "VMD: Visual molecular dynamics," *J. Mol. Graphics*, vol. 14, no. 1, pp. 33–38, 1996.

[51] E. Neria, S. Fischer, and M. Karplus, "Simulation of activation free energies in molecular systems," *J. Chem. Phys.*, vol. 105, pp. 1902–1921, 1996.

[52] G. Offer and R. Sessions, "Computer modelling of the alpha-helical coiled coil: packing of side-chains in the inner core," *J. Mol. Biol.*, vol. 249, pp. 967–987, 1995.

[53] M. Schaefer and M. Karplus, "A comprehensive analytical treatment of continuum electrostatics," *J. Phys. Chem.*, vol. 100, pp. 1578–1599, 1996.

[54] M. Schaefer, C. Bartels, F. Leclerc, and M. Karplus, "Effective atom volumes for implicit solvent models: comparison between Voronoi volumes and minimum fluctuation volumes," *J. Comp. Chem.*, vol. 22, pp. 1857–1879, 2001.

[55] M. de Cuevas, T. Tao, and L. Goldstein, "Evidence that the stalk of Drosophila kinesin heavy chain is an alpha- helical coiled coil," *J. Cell Biol.*, vol. 116, no. 4, pp. 957–965, 1992.

[56] S. Hvidt, F. H. M. Nestler, M. L. Greaser, and J. D. Ferry, "Flexibility of myosin rod determined from dilute solution viscoelastic measurements," *Biochemistry*, vol. 21, pp. 4064–4073, 1982.

[57] D. Lee, S. Ivaninskii, P. Burkhard, and R. Hodges, "Unique stabilizing interactions identified in the two-stranded alpha-helical coiled-coil: Crystal structure of a cortexillin i/gcn4 hybrid coiled-coil peptide," *Protein Science*, vol. 12, pp. 1395–1405, 2003.

[58] Y. Yu, O. Monera, R. Hodges, and P. Privalov, "Ion pairs significantly stabilize coiled-coils in the absence of electrolyte," *J. Mol. Biol.*, vol. 255, no. 3, pp. 367–372, 1996.

[59] J. van Noort, T. van der Heijden, M. de Jager, C. Wyman, R. Kanaar, and C. Dekker, "The coiled-coil of the human Rad50 DNA repair protein contains

specific segments of increased flexibility," *Proc. Natl. Acad. Sci. USA*, vol. 100, no. 13, pp. 7581–7586, 2003.

[60] J. Brown, C. Cohen, and D. Parry, "Heptad breaks in alpha-helical coiled coils: Stutters and stammers." *Proteins*, vol. 26, no. 2, pp. 134–45, 1996.

[61] R. D. Vale, "The molecular motor toolbox for intracellular transport," *Cell*, vol. 112, no. 4, pp. 467–480, 2003.

[62] H. Miki, Y. Okada, and N. Hirokawa, "Analysis of the kinesin superfamily: Insights into structure and function," *Trends Cell Biol.*, vol. 15, no. 9, pp. 467–476, 2005.

[63] H. B. McDonald, R. J. Stewart, and L. S. B. Goldstein, "The kinesin-like *ncd* protein of Drosophila is a minus end-directed microtubule motor," *Cell*, vol. 63, no. 6, pp. 1159–1165, 1990.

[64] R. A. Walker, E. D. Salmon, and S. A. Endow, "The *Drosophila claret* segregation protein is a minus-end directed motor molecule," *Nature*, vol. 347, pp. 713–714, 1990.

[65] F. Kozielski, S. De Bonis, W. P. Burmeister, C. Cohen-Addad, and R. H. Wade, "The crystal structure of the minus-end-directed microtubule motor protein ncd reveals variable dimer conformations," *Structure*, vol. 7, no. 11, pp. 1407–1416, 1999.

[66] A. van der Vaart and M. Karplus, "Simulation of conformational transitions by the restricted perturbation–targeted molecular dynamics method," *J. Chem. Phys.*, vol. 122, p. 114903, 2005.

[67] J. Schlitter, M. Engels, P. Kruger, E. Jacoby, and A. Wollmer, "Targeted molecular dynamics simulation of conformational change-application to the t↔r transition in insulin," *Mol. Simulat.*, vol. 10, no. 2, pp. 291–308, 1993.

[68] A. van der Vaart and M. Karplus, "Minimum free energy pathways and free energy profiles for conformational transitions based on atomistic molecular dynamics simulations," *J. Chem. Phys.*, vol. 126, p. 164106, 2007.

[69] M. Cecchini, A. Houdusse, and M. Karplus, "Allosteric communication in myosin V: From small conformational changes to large directed movements," *PLoS Comp. Bio*, vol. 4, no. 8, p. e1000129, 2008.

[70] S. Fischer and M. Karplus, "Conjugate peak refinement: An algorithm for finding reaction paths and accurate transition states in systems with many degrees of freedom," *Chem. Phys. Lett*, vol. 194, no. 3, pp. 252–261, 1992.

[71] S. Fischer, B. Windshugel, D. Horak, K. C. Holmes, and J. C. Smith, "Structural mechanism of the recovery stroke in the myosin molecular motor," *Proc. Natl. Acad. Sci. USA*, vol. 102, no. 19, pp. 6873–6878, 2005.

[72] W. Zheng and S. Doniach, "A comparative study of motor-protein motions by using a simple elastic-network model," *Proc. Natl. Acad. Sci. USA*, vol. 100, no. 23, pp. 13 253–13 258, 2003.

[73] S. K. Lakkaraju and W. Hwang, "Modulation of elasticity in functionally distinct domains of the tropomyosin coiled-coil," *Cell. Mol. Bioeng.*, vol. 2, no. 1, pp. 57–65, 2009.

[74] W. Hwang, "Calculation of conformation-dependent biomolecular forces," *J. Chem. Phys.*, vol. 127, pp. 175 104–175 109, 2007.

[75] W. Im, M. S. Lee, and C. L. Brooks, "Generalized Born model with a simple smoothing function," *J. Comp. Chem.*, vol. 24, no. 14, pp. 1691–1702, 2003.

[76] S. Broersma, "Rotational diffusion constant of a cylindrical particle," *J. Chem. Phys.*, vol. 32, pp. 1626–1631, 1960.

[77] M. A. Tracy and R. Pecora, "Dynamics of rigid and semirigid rodlike polymers," *Ann. Rev. Phys. Chem.*, vol. 43, no. 1, pp. 525–557, 1992.

[78] C. W. Gardiner, *Stochastic Methods: A Handbook for the Natural and Social Sciences*, 4th ed. Berlin Heidelberg: Springer, 2009.

[79] J. Howard, *Mechanics of Motor Proteins and the Cytoskeleton*. Sunderland, MA: Sinauer, 2001.

[80] E. P. Sablin, F. J. Kull, R. Cooke, R. D. Vale, and R. J. Fletterick, "Crystal structure of the motor domain of the kinesin-related motor ncd," *Nature*, vol. 380, no. 6574, pp. 555–559, 1996.

[81] A. Fiser and A. Sali, "ModLoop: Automated modeling of loops in protein structures," *Bioinformatics*, vol. 19, no. 18, pp. 2500–2501, 2003.

[82] D. van der Spoel, E. Lindahl, B. Hess, G. Groenhof, A. E. Mark, and H. J. C. Berendsen, "GROMACS: Fast, flexible, and free," *J. Comp. Chem.*, vol. 26, no. 16, pp. 1701–1718, 2005.

[83] B. Brooks, C. Brooks III, A. Mackerell Jr, L. Nilsson, R. Petrella, B. Roux, Y. Won, G. Archontis, C. Bartels, S. Boresch, *et al.*, "CHARMM: The biomolecular simulation program," *J. Comp. Chem.*, vol. 30, no. 10, pp. 1545–1614, 2009.

[84] T. Darden, D. York, and L. Pedersen, "Particle mesh Ewald: An N·log(N) method for computing Ewald sums," *J. Chem. Phys*, vol. 98, pp. 10 089–10 092, 1993.

[85] O. N. Yogurtcu, C. W. Wolgemuth, and S. X. Sun, "Mechanical response and conformational amplification in α-helical coiled coils," *Biophys. J.*, vol. 99, no. 12, pp. 3895–3904, 2010.

[86] M. Ito, H. Morii, T. Shimizu, and M. Tanokura, "Coiled coil in the stalk region of ncd motor protein is nonlocally sustained," *Biochemistry*, vol. 45, no. 10, pp. 3315–3324, 2006.

[87] I. Adamovic, S. M. Mijailovich, and M. Karplus, "The elastic properties of the structurally characterized myosin II S2 subdomain: a molecular dynamics and normal mode analysis," *Biophys. J.*, vol. 94, no. 10, pp. 3779–3789, 2008.

[88] J. Lowe, H. Li, K. Downing, and E. Nogales, "Refined structure of $\alpha beta$-tubulin at 3.5 Å resolution," *J. Mol. Biol.*, vol. 313, no. 5, pp. 1045–1057, 2001.

[89] R. Vale and R. Milligan, "The way things move: looking under the hood of molecular motor proteins," *Science*, vol. 288, no. 5463, p. 88, 2000.

[90] C. V. Sindelar, M. J. Budny, S. Rice, N. Naber, R. Fletterick, and R. Cooke, "Two conformations in the human kinesin power stroke defined by x-ray crystallography and EPR spectroscopy," *Nat. Struct. Biol.*, vol. 9, pp. 844–848, 2002.

[91] C. V. Sindelar and K. H. Downing, "An atomic-level mechanism for activation of the kinesin molecular motors," *Proc. Natl. Acad. Sci. USA*, vol. 107, no. 9, pp. 4111–4117, 2010.

[92] M. Vinogradova, V. Reddy, A. Reddy, E. Sablin, and R. Fletterick, "Crystal structure of kinesin regulated by ca2+-calmodulin," *J. Biol. Chem.*, vol. 279, no. 22, p. 23504, 2004.

[93] M. Vinogradova, G. Malanina, V. Reddy, A. Reddy, and R. Fletterick, "Structural dynamics of the microtubule binding and regulatory elements in the kinesin-like calmodulin binding protein," *J. Struct. Biol.*, vol. 163, no. 1, pp. 76–83, 2008.

[94] M. Vinogradova, G. Malanina, A. Reddy, and R. Fletterick, "Structure of the complex of a mitotic kinesin with its calcium binding regulator," *Proc. Natl. Acad. Sci. USA*, vol. 106, no. 20, p. 8175, 2009.

[95] E. Pechatnikova and E. Taylor, "Kinetics processivity and the direction of motion of Ncd," *Biophys. J.*, vol. 77, no. 2, pp. 1003–1016, 1999.

[96] K. A. Foster, A. T. Mackey, and S. P. Gilbert, "A mechanistic model for Ncd directionality," *J. Biol. Chem.*, vol. 276, no. 22, pp. 19 259–19 266, 2001.

[97] K. A. Foster, J. J. Correia, and S. P. Gilbert, "Equilibrium binding studies of non-claret disjunctional protein (Ncd) reveal cooperative interactions between the motor domains," *J. Biol. Chem.*, vol. 273, no. 52, pp. 35 307–35 318, 1998.

[98] H. Sweeney and A. Houdusse, "Structural and functional insights into the myosin motor mechanism," *Ann. Rev. Biophys.*, vol. 39, pp. 539–557, 2010.

[99] D. Leckband and J. Israelachvili, "Intermolecular forces in biology." *Quarter. Rev. Biophys.*, vol. 34, no. 2, pp. 105–267, May 2001.

[100] S. K. Lakkaraju and W. Hwang, "Hysteresis-based mechanism for the directed motility of the Ncd motor," *Biophys. J.*, 2011.

[101] C. V. Sindelar and K. H. Downing, "The beginning of kinesin's force-generating cycle visualized at 9 Å resolution," *J. Cell Biol.*, vol. 177, no. 3, p. 377, 2007.

[102] C. Sindelar, M. Budny, S. Rice, N. Naber, R. Fletterick, and R. Cooke, "Two conformations in the human kinesin power stroke defined by x-ray crystallography and epr spectroscopy," *Nat. Struct. & Mol. Bio.*, vol. 9, no. 11, pp. 844–848, 2002.

[103] H. Sui and K. Downing, "Structural basis of interprotofilament interaction and lateral deformation of microtubules," *Structure*, vol. 18, no. 8, pp. 1022–1031, 2010.

[104] A. Krebs, K. Goldie, and A. Hoenger, "Complex formation with kinesin motor domains affects the structure of microtubules," *J. Mol. Biol.*, vol. 335, no. 1, pp. 139–153, 2004.

[105] W. Wriggers, R. Milligan, and J. McCammon, "Situs: A package for docking crystal structures into low-resolution maps from electron microscopy* 1," *J. Struct. Biol.*, vol. 125, no. 2-3, pp. 185–195, 1999.

[106] A. Hoenger, E. Sablint, R. Vale, R. Fletterickf, and R. Milligan, "Three-dimensional structure of a tubulin-motor-protein complex," *Biol*, vol. 44, pp. 205–227, 1995.

[107] A. MacKerell Jr, D. Bashford, M. Bellott, R. Dunbrack Jr, J. Evanseck, M. Field, S. Fischer, J. Gao, H. Guo, S. Ha, *et al.*, "All-atom empirical potential for molecular modeling and dynamics studies of proteins," *J. Phys. Chem. B*, vol. 102, no. 18, pp. 3586–3616, 1998.

[108] J. Karanicolas and C. Brooks III, "The origins of asymmetry in the folding

transition states of protein l and protein g," *Protein Science*, vol. 11, no. 10, pp. 2351–2361, 2002.

[109] A. Pirani, M. Vinogradova, P. Curmi, W. King, R. Fletterick, R. Craig, L. Tobacman, C. Xu, V. Hatch, and W. Lehman, "An atomic model of the thin filament in the relaxed and ca2+-activated states," *J. Mol. Biol.*, vol. 357, no. 3, pp. 707–717, 2006.

APPENDIX A

LOCAL BENDING STIFFNESS CALCULATIONS

C++ code for retrieving torsion angles from MD data: helix_1.dat and helix_2.dat hold the helical axis information from the two α-helices of the coiled-coil.

build_Triad.h:

```
# include <iostream>
# include <string>
# include <fstream>
#include <sstream>
#include <vector>
using namespace std;
#include <stdlib.h>
#include <stdio.h>
#include <math.h>
#include <vmd_prep.h>
#define PI 3.14159265358979323846264 3

class Triad
{
public:

int i_noOfLines,i_noOfTriads,no_of_pts_per_frame;
char frame_name[100];
float helix_1[500][3],helix_2[500][3],e1[100][3], e2[100][3],
    e3[100][3],e_dash[100][3],centroid[100][3],
   avg_dist_slices,dist_slices[100],mid_pt[100][3];
void build_Triad(char str_pts_1[500][100], char str_pts_2
   [500][100], int no_of_pts_per_frame);
};
\\Returns the absolute value of Nbr
double Abs(double Nbr)
{
        if( Nbr >= 0 )
                return Nbr;
        else
                return -Nbr;
}
```

```
\\Returns squre root of Nbr
double SquareRoot(double Nbr)
{
        double Number = Nbr / 2;
        const double Tolerance = 1.0e-7;

        do Number = (Number + Nbr / Number) / 2;
        while( Abs(Number * Number - Nbr) > Tolerance);

        return Number;
}
\\returns pointer to the cross-product vector of v_1 and v_2
void cross_product (float v_1[],float v_2[], float *result)
{
        //v_1 X v_2
//      cout << "v_1\t" << v_1[0] << "\t" << v_1[1] << "\t"
   << v_1[2] << endl;
//      cout << "v_2\t" << v_2[0] << "\t" << v_2[1] << "\t"
   << v_2[2] << endl;

        result[0] = v_1[1]*v_2[2] - v_2[1]*v_1[2];
        result[1] = v_1[2]*v_2[0] - v_2[2]*v_1[0];
        result[2] = v_1[0]*v_2[1] - v_2[0]*v_1[1];

//      cout << "result\t" << result[0] << "\t" << result[1]
   << "\t" << result[2] << endl;

}
}
```

build_Triad.cpp:

```
#include "build_triad.h"
#include <matrix.h>

#ifndef _NO_NAMESPACE
using namespace std;
using namespace math;
#define STD std
#else
#define STD
#endif

#ifndef _NO_TEMPLATE
typedef matrix<double> Matrix;
#else
typedef matrix Matrix;
#endif
```

```
#ifndef _NO_EXCEPTION
#  define TRYBEGIN()     try {
#  define CATCHERROR()   } catch (const STD::exception& e) { \
                                                    cerr << "
                                                       Error: "
                                                      << e.what
                                                      () << endl
                                                      ; }
#else
#  define TRYBEGIN()
#  define CATCHERROR()
#endif

void Triad::build_Triad(char str_ctr_coor_1[500][100], char
   str_ctr_coor_2[500][100], int no_of_pts_per_frame)
{
        int i=0,j=0,k=0;
        float x_1, x_2, x_3, y_1,y_2,y_3,z_1,z_2,z_3,midpt_i,
            midpt_j,midpt_k,sqr_length;
        float tmp_e_x,tmp_e_y,tmp_e_z,length,*temp;

        char *tmp;
        tmp = (char *) malloc (strlen(str_ctr_coor_1[10]));
        for (i=0; i < no_of_pts_per_frame;i++)
        {

//              cout << str_ctr_coor_1[10] << endl;
                memcpy((void*)tmp,(void*)&str_ctr_coor_1[i
                    ][0],11);
                Triad::helix_1[i][0] = atof(tmp);

                memcpy((void*)tmp,(void*)&str_ctr_coor_1[i
                    ][12],17);
                Triad::helix_1[i][1] = atof(tmp);

                memcpy((void*)tmp,(void*)&str_ctr_coor_1[i
                    ][28],17);
                Triad::helix_1[i][2] = atof(tmp);

        //      cout << Triad::helix_1[i][0] << "\t" << Triad
            ::helix_1[i][1] << "\t" << Triad::helix_1[i][3] <<
             endl;

        }

        for (i=0; i < no_of_pts_per_frame;i++)
```

```
        {

                memcpy((void*)tmp,(void*)&str_ctr_coor_2[i
                    ][0],11);
                Triad::helix_2[i][0] = atof(tmp);

                memcpy((void*)tmp,(void*)&str_ctr_coor_2[i
                    ][12],17);
                Triad::helix_2[i][1] = atof(tmp);

                memcpy((void*)tmp,(void*)&str_ctr_coor_2[i
                    ][28],17);
                Triad::helix_2[i][2] = atof(tmp);

        }

        for (i=0; i < no_of_pts_per_frame;i++)
        {
                Triad::centroid[i][0] = (Triad::helix_1[i][0]
                    + Triad::helix_2[i][0])/2;
                Triad::centroid[i][1] = (Triad::helix_1[i][1]
                    + Triad::helix_2[i][1])/2;
                Triad::centroid[i][2] = (Triad::helix_1[i][2]
                    + Triad::helix_2[i][2])/2;
        }

        for (i=0; i< no_of_pts_per_frame-1;i++)
        {
                tmp_e_x = Triad::centroid[i+1][0] - Triad::
                    centroid[i][0];
                tmp_e_y = Triad::centroid[i+1][1] - Triad::
                    centroid[i][1];
                tmp_e_z = Triad::centroid[i+1][2] - Triad::
                    centroid[i][2];

                sqr_length = (pow(tmp_e_x,2)+pow(tmp_e_y,2)+
                    pow(tmp_e_z,2));
                Triad::dist_slices[i] = length;
                length = SquareRoot((double)sqr_length);

                Triad::e3[i][0] = tmp_e_x/length;
                Triad::e3[i][1] = tmp_e_y/length;
                Triad::e3[i][2] = tmp_e_z/length;
        }

float sum=0;
```

```
for ( i =0; i < no_of_pts_per_frame-1 ; i++)
        sum = sum + Triad::dist_slices[i];

 Triad::avg_dist_slices = sum/(no_of_pts_per_frame-1)
    ;

cout << "Average distance between slices " << Triad::
   avg_dist_slices << endl;

temp = (float *) malloc (sizeof(Triad::e1));
for (i=0; i< no_of_pts_per_frame-1;i++)
{
        tmp_e_x = Triad::centroid[i][0] - Triad::
           helix_1[i][0];
        tmp_e_y = Triad::centroid[i][1] - Triad::
           helix_1[i][1];
        tmp_e_z = Triad::centroid[i][2] - Triad::
           helix_1[i][2];

        sqr_length = (pow(tmp_e_x,2)+pow(tmp_e_y,2)+
           pow(tmp_e_z,2));
        length = SquareRoot((double)sqr_length);

        Triad::e_dash[i][0] = tmp_e_x/length;
        Triad::e_dash[i][1] = tmp_e_y/length;
        Triad::e_dash[i][2] = tmp_e_z/length;

        cross_product( e_dash[i],Triad::e3[i],temp);

        sqr_length = (pow(Abs(temp[0]),2)+pow(Abs(
           temp[1]),2)+pow(Abs(temp[2]),2));
        length = sqrt(sqr_length);

        Triad::e2[i][0] = temp[0]/length;
        Triad::e2[i][1] = temp[1]/length;
        Triad::e2[i][2] = temp[2]/length;
}


for (i=0; i< no_of_pts_per_frame-1;i++)
{

         cross_product ( Triad::e3[i],Triad::e2[i],
            temp);

         sqr_length = (pow(temp[0],2)+pow(temp[1],2)+
            pow(temp[2],2));
```

```
                    length = SquareRoot(sqr_length);

                    Triad::e1[i][0] = temp[0]/length;
                    Triad::e1[i][1] = temp[1]/length;
                    Triad::e1[i][2] = temp[2]/length;
          }

}


void trans_mat(float a[3][3], float b[3][3])
  {
    int i,j,e3,e2,e1,e4;
    for(i=0;i<3;i++)
      {     for(j=0;j<3;j++)
          {
            b[i][j] =  a[j][i];
          }
      }
  }

void det_mat(float a[3][3],float *det )
  {
    int i,j,e3,e2,e1,e4;
    float b[3][3];
    i=0;
    b[0][0] =   (a[1][1]*a[2][2] - a[2][1]* a[1][2]);
    b[0][1] =  -(a[1][0]*a[2][2] - a[2][0]* a[1][2]);
    b[0][2] =   (a[1][0]*a[2][1] - a[2][0]* a[1][1]);
    *det = (a[0][0]*b[0][0]+ a[0][1]*b[0][1]+ a[0][2]*b
       [0][2]);
  }

void minor_mat(float a[3][3], float b[3][3])
  {
    int i,j,e3,e2,e1,e4;
    b[0][0] =   (a[1][1]*a[2][2] - a[2][1]* a[1][2]);
    b[0][1] =  -(a[1][0]*a[2][2] - a[2][0]* a[1][2]);
    b[0][2] =   (a[1][0]*a[2][1] - a[2][0]* a[1][1]);
    b[1][0] =  -(a[0][1]*a[2][2] - a[2][1]* a[0][2]);
    b[1][1] =   (a[0][0]*a[2][2] - a[2][0]* a[0][2]);
    b[1][2] =  -(a[0][0]*a[2][1] - a[2][0]* a[0][1]);
    b[2][0] =   (a[0][1]*a[1][2] - a[1][1]* a[0][2]);
    b[2][1] =  -(a[0][0]*a[1][2] - a[1][0]* a[0][2]);
    b[2][2] =   (a[0][0]*a[1][1] - a[1][0]* a[0][1]);
```

```
  }

void mul_mat(float a[3][3], float b[3][3], float c[3][3])
  {
    int i,j,k;
    for(i=0;i<3;i++)
      {for(j=0;j<3;j++)
          {c[i][j] =  0;}
      }
    for(k=0;k<3;k++)
      {for(i=0;i<3;i++)
          {for(j=0;j<3;j++)
              {
                c[i][k] =  c[i][k] +  a[i][j]*b[j][k];
              }
          }
      }
  }// end mul_mat
void inv_mat(float a[3][3], float b[3][3])
  {
    int i,j;
    float  det, temp[3][3];
    det_mat(a,&det);
    minor_mat(a,temp);
    trans_mat(temp,b);
    for(i=0;i<3;i++)
    {     for(j=0;j<3;j++)
          {
              b[i][j] =  b[i][j];//det;
          }
    }
   }//emd inv_mat
    //
void transformation_mat(float e3[], float e2[], float e1[],
   float e3_dash[], float e2_dash[], float e1_dash[], float t
   [3][3])
  {
    float temp[3][3], A[3][3], B[3][3],det;
    int i,j,k;

    //A,B are the basis vector matrices whose rows contain
       basis vectors.
    for(j=0;j<3;j++)
    {
          B[0][j]=e3[j];
          A[0][j]=e3_dash[j];
```

```
            B[1][j]=e2[j];
            A[1][j]=e2_dash[j];
            B[2][j]=e1[j];
            A[2][j]=e1_dash[j];
    }
/*          for (int i=0;i<3;i++)
                {
                        for(int j=0;j<3;j++)
                        {
                                cout << "E' ["<<i<<"]["<< j
                                   << "] = " << A[i][j] <<
                                    endl;
                        }
                }
            for (int i=0;i<3;i++)
                {
                        for(int j=0;j<3;j++)
                        {
   //                                   cout << "E ["<<i<<"]["<< j
       << "] = " << B[i][j] << endl;
                        }
                } */

    inv_mat(B,temp);
    mul_mat(A,temp,t);
   }// end void transformation_mat
void euler_angle_bet_planes_alpha(float e3[], float e2[],
   float e1[], float e3_dash[], float e2_dash[], float
   e1_dash[], float *alpha,float *beta, float *gamma)
{
        float transform[3][3],theta_temp,sin_beta,cos_beta,
           cos_alpha, tan_alpha,pi,tmp_beta,tmp_gamma;
        pi = acos(-1);
        transformation_mat(e3,e2,e1, e3_dash, e2_dash,e1_dash
           ,transform);

/*          for (int i=0;i<3;i++)
                {
                        for(int j=0;j<3;j++)
                        {
                                cout << "Transform ["<<i
                                   <<"]["<< j << "] = " <<
                                   transform[i][j] << endl;
                        }
                } */
```

```
        tan_alpha = -transform[0][1]/transform[0][0];

//      cout << "alpha from tan calculation " << atan(
    tan_alpha) << endl;

        sin_beta = transform[0][2];
        *beta = asin(sin_beta);
        cos_beta = cos(tmp_beta);
//      cos_alpha = transform[0][0]/cos_beta;
//      cout << "alpha from cos calculation " << acos(
    cos_alpha) << endl;

        tmp_gamma = acos (transform[2][2]/cos_beta);

        *alpha = atan(tan_alpha);
        *gamma = tmp_gamma;

}

void euler_angle_bet_planes_beta(float e3[], float e2[],
    float e1[], float e3_dash[], float e2_dash[], float
    e1_dash[], float *alpha,float *beta, float *gamma)
{
        float transform[3][3],theta_temp,sin_gamma,cos_gamma,
            cos_alpha, cos_beta,tan_beta,pi,tmp_gamma;
        pi = acos(-1);
        transformation_mat(e3,e2,e1, e3_dash, e2_dash,e1_dash
            ,transform);

        tan_beta = -transform[2][0]/transform[2][2];

//      cout << "beta from tan calculation " << atan(tan_beta
    ) << endl;

        sin_gamma = transform[2][1];
        tmp_gamma = asin(sin_gamma);
        *gamma = tmp_gamma;
        cos_gamma = cos(tmp_gamma);
        *alpha = acos(transform[1][1]/cos_gamma);


        //cos_beta = transform[2][2]/cos_gamma;

        *beta = atan(tan_beta);

}
```

```
void euler_angle_bet_planes_gamma(float e3[], float e2[],
   float e1[], float e3_dash[], float e2_dash[], float
   e1_dash[], float *alpha,float *beta, float *gamma)
{
        float transform[3][3],theta_temp,sin_alpha,cos_gamma,
           cos_alpha, cos_beta,tan_beta,pi,tmp_gamma,
           tmp_alpha,tmp_beta,tan_gamma;
        pi = acos(-1);
        transformation_mat(e3,e2,e1, e3_dash, e2_dash,e1_dash
           ,transform);

        tan_gamma = -transform[1][2]/transform[1][1];

//      cout << " gamma from tan calculation " << atan(
   tan_gamma) << endl;

        sin_alpha = transform[1][0];
        tmp_alpha = asin(sin_alpha);
        *alpha = tmp_alpha;
        cos_alpha = cos(tmp_alpha);

//      cout << "gamma from cos calculation " << acos(
   transform[1][1]/cos_alpha) << endl;;

        tmp_beta = acos(transform[0][0]/cos_alpha);
        *beta = tmp_beta;
        *gamma = atan(tan_gamma);

}
void calc_Angle(vector<Triad> &vec_Triad, int triad_num)
{
//      cout << " Inside calc_Angle " << endl;
        float e3[3],e2[3],e1[3],e3_dash[3],e2_dash[3],e1_dash
           [3],pi;
        float e1_alpha,e1_beta,e1_gamma,e2_alpha,e2_beta,
           e2_gamma, e3_alpha,e3_beta,e3_gamma;
        float alpha,beta,gamma;
        int i;
        pi = acos(-1);
        char tmp[100];
        sprintf(tmp ,"./triad_angles/alpha_%d.dat",triad_num)
           ;
        ofstream f_alpha(tmp,ios_base::out);

        sprintf(tmp ,"./triad_angles/beta_%d.dat",triad_num);
        ofstream f_beta(tmp,ios_base::out);
```

```
        sprintf(tmp ,"./triad_angles/gamma_%d.dat",triad_num)
            ;
        ofstream f_gamma(tmp,ios_base::out);

        sprintf(tmp,"./triad_angles/dist_%d.dat",triad_num);
        ofstream f_dist(tmp,ios_base::out);

        float sum = 0;
 for (i=0;i<=1000;i++)
        {
                euler_angle_bet_planes_alpha(vec_Triad[i].e3[
                    triad_num-1], vec_Triad[i].e2[triad_num
                    -1], vec_Triad[i].e1[triad_num-1],
                    vec_Triad[i].e3[triad_num], vec_Triad[i].
                    e2[triad_num], vec_Triad[i].e1[triad_num],
                     &e1_alpha,&e1_beta,&e1_gamma);
                euler_angle_bet_planes_beta(vec_Triad[i].e3[
                    triad_num-1], vec_Triad[i].e2[triad_num
                    -1], vec_Triad[i].e1[triad_num-1],
                    vec_Triad[i].e3[triad_num], vec_Triad[i].
                    e2[triad_num], vec_Triad[i].e1[triad_num],
                     &e2_alpha,&e2_beta,&e2_gamma);
                euler_angle_bet_planes_gamma(vec_Triad[i].e3[
                    triad_num-1], vec_Triad[i].e2[triad_num
                    -1], vec_Triad[i].e1[triad_num-1],
                    vec_Triad[i].e3[triad_num], vec_Triad[i].
                    e2[triad_num], vec_Triad[i].e1[triad_num],
                     &e3_alpha,&e3_beta,&e3_gamma);

//              cout << alpha << "\t" << beta << "\t" <<
   gamma << endl;
                alpha = e1_alpha/(vec_Triad[i].dist_slices[
                    triad_num-1]);
                beta = e2_beta/(vec_Triad[i].dist_slices[
                    triad_num-1]);
                gamma = e3_gamma/(vec_Triad[i].dist_slices[
                    triad_num-1]);
//              cout << alpha << "\t" << beta << "\t" <<
   gamma << endl;


/*              alpha = e1_alpha*180/pi;
                beta = e2_beta*180/pi;
                gamma = e3_gamma*180/pi; */
```

```
                if(abs(alpha) < 0.0001)
                {
                        f_alpha << 0 << endl;
                }
                else
                {
                        f_alpha << alpha << endl;
                }

                if(abs(beta) < 0.0001)
                {
                        f_beta << 0 << endl;
                }
                else
                {
                        f_beta << beta << endl;
                }
                if(abs(gamma) < 0.0001)
                {
                        f_gamma << 0 << endl;
                }
                else
                {
                        f_gamma << gamma << endl;
                }
                sum = sum + vec_Triad[i].dist_slices[
                   triad_num];
                f_dist << vec_Triad[i].dist_slices[triad_num]
                    << endl;
        }

        //cout << " Avg distance between slices " << sum/499
           << endl;
        f_alpha.close();
        f_beta.close();
        f_gamma.close();
        f_dist.close();

}
\\call to the program using triad number : calculates the
   torsion angles between this and the neighboring triad
int main(int argc,char* argv[])
{


        int i=0,j=1;
        char tmp1[200],tmp2[200],frame_name[100];
```

```
        vector <Triad> vec_Triad;

        int no_of_res,no_of_pts_per_frame;
        no_of_res = 284;
        no_of_pts_per_frame = 55;

        sprintf(tmp1 ,"helix_1.dat");
        sprintf(tmp2 ,"helix_2.dat");

        ifstream f_ctr1(tmp1,ifstream::in);
        ifstream f_ctr2(tmp2,ifstream::in);

        if(f_ctr1.is_open() && f_ctr2.is_open())
        {
//                      cout << " Successfully opened the files
   \t" << tmp1 <<"\t" << tmp2 << " \tfor reading co-ordinates
    " << endl;
        }
        else
        {
                cout << " Problems in opening the file for co
                   -ordinates,\t" << tmp1 << "\t" << tmp2<< "
                   \t quitting" << endl;

        }

        char str_ctr_coor_1[100][100],str_ctr_coor_2
           [100][100];
        j=1;
        while ((!f_ctr1.eof()) ||(!f_ctr2.eof()))
        {
                for (i = 0; i < no_of_pts_per_frame; i++)
                {
                        f_ctr1.getline(str_ctr_coor_1[i],100)
                           ;
                        f_ctr2.getline(str_ctr_coor_2[i],100)
                           ;

//                      cout << str_ctr_coor_2[i] << endl;

                                if((!str_ctr_coor_1[i][0]) ||
                                    (!str_ctr_coor_2[i][0]))
                        {
                                cout << "inside if loop" <<
                                   endl;
                                goto finish_loop;
                        }
```

```
                }

                        Triad obj_Triad;
                        obj_Triad.build_Triad(str_ctr_coor_1,
                            str_ctr_coor_2,no_of_pts_per_frame
                            );

                        vec_Triad.push_back(obj_Triad);
        }

        finish_loop:
        int triad_num;
        triad_num = atoi(argv[1]);
        cout << " Triad number " << triad_num << endl;
        calc_Angle(vec_Triad,triad_num);
 return 0;
}
```

calc_stiffness_alpha.m: (can be used for beta and gamma stiffness values as well).

Determine the stiffness from the curvature of the torsion angle distributions obtained from build_triad.cpp.

```
triad=1;
alpha_bending_stiffness = fopen("triad_angles/avg_lp1.dat","w
    ");
alpha_equilibrium_1 = fopen("triad_angles/avg_alpha_1.dat","w
    ");
alpha_equilibrium_2 = fopen("triad_angles/avg_alpha_2.dat","w
    ");
avg_alpha = fopen("avg_alpha_e0.dat","w");
for triad=1:55
        alpha_file="triad_angles/alpha_";
        alpha_file=strcat(alpha_file,int2str(triad));
        alpha_file=strcat(alpha_file,".dat");
        alpha_hist_str="triad_angles/hist_alpha_";
        alpha_hist_str=strcat(alpha_hist_str,int2str(triad));
        alpha_hist_str=strcat(alpha_hist_str,".dat");
        alpha_reg_str="triad_angles/reg_alpha_";
        alpha_reg_str=strcat(alpha_reg_str,int2str(triad));
        alpha_reg_str=strcat(alpha_reg_str,".dat");
        alpha_hist_file = fopen(alpha_hist_str,"w");
        alpha_reg_file = fopen(alpha_reg_str,"w");

        dist = load("triad_angles/avg_dist.dat");
```

```
        alpha = load(alpha_file);

[hist_alpha,bin] = hist(alpha,100);

#disp(bin);

i=1;
for n=1:100
        regression = -log(hist_alpha(n));
        if ( regression != Inf )
                x(i) = bin(n);
                y(i) = regression;
                fprintf(alpha_reg_file,"%f\t%d\n",bin(n),
                    regression);
                i++;
        endif

        fprintf(alpha_hist_file,"%f\t%d\n",bin(n),hist_alpha(
            n));
endfor

p= polyfit(x,y,2)

bending_stiffness = (2*p(1))/dist(1,2)
fprintf(alpha_bending_stiffness,"%d\t%f\n",triad,
    bending_stiffness);

equilibrium_angle_1 = sqrt(p(3)*2/(bending_stiffness))
fprintf(alpha_equilibrium_1,"%d\t%f\n",triad,
    equilibrium_angle_1);


equilibrium_angle_2 = -(p(2)/(bending_stiffness))
fprintf(alpha_equilibrium_2,"%d\t%f\n",triad,
    equilibrium_angle_2);

fprintf(avg_alpha,"%d\t%f\n",triad,(equilibrium_angle_2*180/
    pi));

endfor
```

VITA

Sirish Kaushik Lakkaraju received his Bachelor of Engineering degree in electronics and instrumentation from the University of Madras at Chennai, India in 2003. He received his Master of Science degree in biomedical engineering from Texas A&M University in 2008 and his Ph.D. in December 2011. His research interests lie in studying the role of mechanics and dynamics of biological macromolecules and macromolecular assemblies on their function.

Contact Address:
Department of Biomedical Engineering
5045 Emerging Technologies Building
3120 TAMU
College Station, TX 77843-3120
c/o Wonmuk Hwang